# Détermination des mécanismes de dégradation d'électrodes modèles de pile à combustible à membrane échangeuse de protons

Zuzhen Z.Zhao Zhao

## To cite this version:

Zuzhen Z.Zhao Zhao. Détermination des mécanismes de dégradation d'électrodes modèles de pile à combustible à membrane échangeuse de protons. Autre. Institut National Polytechnique de Grenoble - INPG, 2012. Français. NNT : . tel-00764891v1

HAL Id: tel-00764891
https://theses.hal.science/tel-00764891v1

Submitted on 13 Dec 2012 (v1), last revised 25 Jul 2013 (v2)

UNIVERSITÉ DE GRENOBLE

# THÈSE

Pour obtenir le grade de

## DOCTEUR DE L'UNIVERSITÉ DE GRENOBLE

Spécialité : **Matériaux, Mécanique, Génie Civil, Électrochimie**

Arrêté ministériel : 7 août 2006

Présentée par

**Zuzhen ZHAO**

Thèse dirigée par **Frédéric MAILLARD**

préparée au sein du **Laboratoire d'Electrochimie et de Physico-chimie des Matériaux et des Interfaces**
dans **l'École Doctorale Ingénierie-Matériau Mécanique Énergétique Environnement procédés Production**

# Détermination des mécanismes de dégradation d'électrodes modèles de pile à combustible à membrane échangeuse de protons

Thèse soutenue publiquement le **07 Décembre 2012**,
devant le jury composé de :

**Prof. M. Chatenet**
Professeur, Grenoble-INP, France, Président

**Prof. C. Coutanceau**
Professeur, Université de Poitiers, France, Rapporteur

**Dr. N. Job**
Première assistante, Université de Liège, Belgique, Rapporteur

**Dr. F. Maillard**
Chargé de recherche CNRS, Grenoble, France, Directeur de thèse

# Table of contents

**Table of contents** .......... **1**

*Acknowledgements* .......... *7*

**List of abbreviations and symbols** .......... **9**

**Chapter I- Literature review** .......... **13**

**I. Energy and environmental crisis review** .......... **15**

A. From the first industrial revolution to the energy crisis .......... 15

B. Promising renewable energies .......... 16

C. Fuel cells and the hydrogen energy .......... 17

**II. Proton exchange membrane fuel cell** .......... **18**

A. Historical notes .......... 18

B. Working principle .......... 18

**III. Issues for practical PEMFC applications** .......... **20**

A. High cost of PEMFC materials .......... 21

B. Low durability of PEMFC materials .......... 23

*1. Degradation of the bipolar plates* .......... *23*

*2. Degradation of the gas-diffusion layers* .......... *23*

*3. Degradation of the proton-exchange membrane* .......... *24*

*4. Degradation of the catalytic layers* .......... *25*

**IV. Degradation mechanisms of the Pt/C catalysts in PEMFC CLs** .......... **26**

A. 3D Ostwald ripening .......... 27

B. Corrosion of the carbon support .......... 28

C. Migration of Pt nanocrystallites .......... 29

**V. Structural markers of Pt/C degradation** .......... **30**

A. Physical markers .......... 30

*1. Pt crystallite/particle growth* .......... *30*

*2. Aggregation of Pt nanoparticles* .......... *31*

*3. Particle detachment* ....31

B. Electrochemical markers of Pt/C degradation ....32

*1. Adsorption/desorption of H/O* ....32

*2. Electrooxidation of a $CO_{ads}$ monolayer (CO stripping)* ....33

**VI. Conclusions .... 36**

**Chapter II - Experimental .... 39**

**I. Electrocatalysts .... 41**

A. Pt/XC72 nanoparticles (E-TeK, Inc.) ....41

B. Pt/Sibunit nanoparticles ....41

C. Pt nanowires supported on Vulcan XC72 (Pt NWs/XC72) ....42

**II. Characterization of the fresh/aged electrocatalysts .... 42**

A. Physical techniques ....42

***1. Transmission electron microscopy*** ....42

***2. Identical-location TEM (IL-TEM)*** ....44

***3. X-ray diffraction*** ....45

***4. Field-emission gun–scanning electron microscopy (FEG —SEM)*** ....46

B. Chemical techniques ....46

***1. X-ray Photoelectron Spectroscopy (XPS)*** ....46

***2. Raman spectroscopy*** ....47

***3. In situ Fourier Transform Infrared Spectroscopy (in situ FTIR)*** ....48

C. Cyclic voltammetry ....48

**III. Preparation of the samples/solutions .... 49**

A. Solutions ....49

B. Electrochemical cell set-up ....49

C. Ink preparation and ageing ....49

**IV. Hydrodynamic methods .... 50**

A. Study of the oxygen reduction reaction on a rotating disk electrode (ORR, RDE) ....50

B. Study of the oxygen reduction reaction on a rotating ring disk electrodes (ORR, RRDE) ....51

**V. Accelerated aging tests (AATs) .... 52**

*1. Sequential CO stripping experiments ......52*

*2. Accelerated aging tests in solution containing oxidizing, reducing or inert molecules ..53*

**Chapter III ...... 55**

**Evidences of the migration of Pt crystallites on high surface area carbon supports in the presence of reducing molecules ...... 55**

**I. Introduction...... 57**

**II. Results and discussion ...... 59**

A. Definition of structural markers of "crystallite migration" ......59

B. Mobility of Pt crystallites under CO environment......63

C. Effect of $H_2$, CO and $CH_3OH$ ......65

D. Effect of the upper potential sweeping conditions......70

E. Identical-location TEM (IL-TEM) experiments......73

F. On the origin of Pt crystallite migration......75

*1. Changes in the work of adhesion upon chemisorption......75*

*2. Trapping of Pt nanoparticles at defects of the graphitic crystallites......77*

*3. Reduction of oxygen-containing carbon surface groups ......78*

**III. Conclusions ...... 80**

**Chapter IV...... 83**

**Carbon corrosion and platinum nanoparticles ripening under open circuit potential conditions ...... 83**

**I. Introduction...... 85**

**II. Results and discussion ...... 87**

A. Electrochemical characterization......87

B. XPS measurements......90

C. EC-FTIR measurements ......91

D. Raman spectroscopy measurements ......94

E. Change of the Pt/C structure by electrochemical and electron-based techniques ......96

F. Insights into the carbon corrosion mechanism...... 100

**III. Conclusions ...... 101**

**Chapter V–Effect of catalyst layer thickness and Pt loading on the ORR activity ................................. 103**
**I. Introduction ........................................................................................................................ 105**
**II. Results and discussion ........................................................................................................ 107**
- A. Physical characterization ................................................................................................ 107
- B. Electrochemical characterization ................................................................................... 111
- C. Effect of the catalyst loading on the ORR activity ......................................................... 113
  - *1. Rotating disk electrode measurements ........................................................................ 113*
  - *2. Rotating ring-disk electrode measurements ................................................................. 116*
- D. Stability of Pt/Sibunit electrocatalysts in the presence of oxidizing and reducing gas ................ 120

**III. Conclusions ...................................................................................................................... 123**

**Chapter VI ............................................................................................................................. 125**
**Pt NWs as more robust electrocatalysts for PEMFC applications ........................................... 125**
**I. Introduction ........................................................................................................................ 127**
**II. Results and discussion ........................................................................................................ 129**
- A. Physical properties of Pt NWs/C catalyst ...................................................................... 129
  - *1. Transmission Electron Microscopy characterization ..................................................... 130*
  - *2. Scanning Electron Microscope (SEM) characterization ................................................. 130*
  - *3. XRD characterization ..................................................................................................... 131*
- B. Enhanced durability of Pt NWs/C with respect to Pt NPs/C ............................................ 133
  - *1. Effect of subsequent CO stripping experiments ............................................................ 133*
  - *2. Effect of reducing molecules such as CO and $CH_3OH$ .................................................. 134*
  - *3. Effect of the carbon support ......................................................................................... 136*
  - *4. Long term ageing treatment .......................................................................................... 136*
- C. Electrocatalytic activity of Pt NWs/C for the MOR ......................................................... 137

**III. Conclusions ...................................................................................................................... 140**
**Chapter VII – General conclusion and outlook ....................................................................... 143**
**References ............................................................................................................................. 149**

**To Liting**

# Acknowledgements

*At the end of this work, I would like to express my gratitude to all the people who supported me. But I don’t think it is possible to thank all of them in this short page.*

*This work has been done in the Laboratoire d'Electrochimie et de Physico-chimie des Matériaux et des Interfaces in the past three years. I was honoured to work in such a pleasant atmosphere with so many nice and talented persons. Thanks to all of you for your kind help during my stay in France.*

*I want to particularly thank the persons who always trusted and encouraged me during my Ph.D.; they are the power source of my life. Thanks to my family and friends.*

*I would like to thank my supervisor Dr. F. Maillard. His academic support and scientific guiding allowed me to overcome various difficulties. He is the model for me to be a better and delicate man in my future life.*

*I am deeply thankful to the Reviewers and the Jury for kindly accepting to review this work.*

*I would like to thank Prof. M. Chatenet and other teachers from Grenoble-INP for their teaching in the classes during the past three years.*

*I want to thank Dr. L. Dubau for performing the TEM images and for many thoughtful discussions. I also express my gratitude to Dr. B. Vion-Dury, Dr. J. Durst and Ms. Sc. L. Castanheira for their kind help in the everyday life.*

*This thesis would not have been possible without the financial support from the China Scholarship Council.*

*I would like to thank all the people I interacted with and learned from while at LEPMI and Grenoble-INP.*

*From the bottom of my heart, I thank you all!*

## List of abbreviations and symbols

| **Abbreviation** | **Explanation** | |
|---|---|---|
| **AAT** | Accelerated aging test | |
| **CL** | Catalytic layer | |
| **COR** | Carbon oxidation reaction | |
| **$CO_{surf}$** | Carbon surface oxide groups | |
| **CPD** | Averaged closest distance between two Pt nanoparticles | |
| **CTAB** | Cetyltrimethylammonium bromide | |
| **CV** | Cyclic voltammetry | |
| **DEMS** | Differential electrochemical mass spectroscopy | |
| **ECSA** | Electrochemically active surface area | |
| **GC** | Glassy carbon | |
| **GDL** | Gas-diffusion layer | |
| **GSD** | Grain size distribution | |
| **$H_{ads}$** | Adsorbed hydrogen | |
| **$H_{des}$** | Desorbed hydrogen | |
| **HOR** | Hydrogen oxidation reaction | |
| **HPL** | High upper potential limit | |
| **HRTEM** | High resolution transmission electron microscopy | |
| **HSAC** | High surface area carbon | |
| **IL-TEM** | Identical-location transmission electron microscopy | |
| ***In situ* FTIR** | *In situ* Fourier transform infrared spectroscopy | |
| **IPD** | Average interparticle distance | |
| **LPL** | Low upper potential limit | |
| **MEA** | Membrane electrode assembly | |
| **MOR** | Methanol oxidation reaction | |
| **MPL** | Micro-porous layer | |
| **MSE** | Mercury sulphate electrode | |
| **NP** | Nanoparticle | |
| **NW** | Nanowire | |
| **OCP** | Open circuit potential | |
| **PEM** | Proton-exchange membrane | |
| **PEMFC** | Proton-exchange membrane fuel cell | |
| **PSD** | Particle size distribution | |
| **RDE** | Rotating disk electrode | |

| | |
|---|---|
| **rpm** | Revolutions per minute |
| **RRDE** | Rotating ring disk electrode |
| **SHE** | Standard hydrogen electrode |
| **TC** | Texture coefficient |
| **TEM** | Transmission electron microscopy |
| **XPS** | X-ray photoelectron spectroscopy |
| **XRD** | X-ray diffraction |
| **Ref.** | Reference |
| ***0D, 1D, 2D*** | Zero-dimensional, one-dimensional, two-dimensional |

| Symbol | Meaning | Usual unit |
|---|---|---|
| $\sigma$ | Surface tension | dyne $cm^{-1}$ |
| $\beta$ | Shape factor | |
| $\vartheta$ | Angle at the peak maximum | rad |
| $\lambda$ | X-ray wavelength | cm |
| $\rho$ | Density | g $cm^{-3}$ |
| $\mu$ | Metal loading on glassy carbon | µg $cm^{-2}$ |
| $A$ | Area | $cm^2$ |
| $\bar{d}_N$ | Number averaged diameter | nm |
| $\bar{d}_S$ | Surface averaged diameter | nm |
| $\bar{d}_V$ | Volume-averaged mean diameter | nm |
| $E$ | Potential | V |
| $F$ | Faraday constant | C |
| $I$ | Current | A |
| $I(hkl)_i$ | Intensity of the *(hkl)* plane | |
| $I_D$ | Disk current | A |
| $I_R$ | Ring current | A |
| $I_b$ | Backward peak current | mA |
| $I_f$ | Forward peak current | mA |
| $I_{fa}$ | Faradaic current | A |
| $I_C$ | Capacitive current | A |
| $j$ | Current density | A $cm^{-2}$ |
| $j_k$ | Kinetic current density | |
| $I_L^{\text{diff, solution}}$ | $O_2$ diffusion limited current density in the liquid electrolyte | A $cm^{-2}$ |

| | | |
|---|---|---|
| $I_L^{\text{diff. CL}}$ | $O_2$ diffusion limited current density in the catalytic layer | A $cm^{-2}$ |
| $\boldsymbol{K}$ | Scherrer constant | |
| $\boldsymbol{L}$ | Thickness of the catalyst layer | µm |
| $\boldsymbol{m}$ | Weight | g |
| $\boldsymbol{n_{e^-}}$ | Average number of electrons produced during the reduction of a dioxygen molecule | |
| $\boldsymbol{Q_{CO}}$ | Charge required to oxidize a monolayer of CO | C |
| $\boldsymbol{Q_H}$ | Charge required to desorb a monolayer of hydrogen | C |
| $\boldsymbol{R}$ | Reflectivity | |
| $\boldsymbol{S_c}$ | Specific surface area of carbon | $m^{-2}$ g |
| $\boldsymbol{T}$ | Temperature | °C |
| $\boldsymbol{v}$ | Sweep rate | V $s^{-1}$ |
| $\boldsymbol{V}$ | Volume | $cm^3$ |
| $\boldsymbol{W}$ | Adhesion work | J |
| ***wt. %*** | Weight percent | % |

# CHAPTER I- LITERATURE REVIEW

# I. Energy and environmental crisis review

## A. From the first industrial revolution to the energy crisis

Starting from the United Kingdom in the 18th century, the first industrial revolution has profoundly affected the lives of a part of humanity. It was driven by the progress of agriculture and the population increase that caused an increase in demand and production. This demand was satisfied thanks to a set of parameters: (i) development of iron, cast iron and steel manufacturing, (ii) shorter times between scientific discoveries and technical applications, (iii) abundant workforce and (iv) profusion of low-cost primary energy sources, such as coal. Combined to steam engines, coal provided energy in mines, factories, and allowed the development of new means of transport (rail, boat). Years later, coal was replaced by oil that was lighter, and easier to store and transport. This new source of energy was called "black gold" and became the main energy source during the 20th century. Today, most of the energy consumed by the world comes from non-renewable resources, which are limited in quantities and can be depleted. Examples include: oil (petroleum), natural gas, coal and uranium (nuclear). Petroleum accounts for approximately 34% of the world’s energy consumption. [1] Coal and natural gas together supply approximately 48%. Uranium is another non-renewable energy resource used in nuclear power plants, and is used for approximately 7% of the world’s energy. Finally, renewable energy resources (solar, wind, biomass and hydropower) account for approximately 8% of the world’s energy consumption.

The situation in 2012 resembles that of a dangerous "end of game": the price of these non-renewable resources climbs because they are of limited supply and cannot be replenished in a short period of time. Furthermore, our economy has become so globalized that their scarcity also affects the price of most of the goods that we use in our daily lives. According to the global proved reserves, the primary energy resources just can provide less than several hundreds of years need at present conditions [2]. In addition, the consumption of the fossil fuels impacts on the environment through the production of greenhouse gases. Indeed, when coal, oil or natural gas is burned they release a large range of greenhouse gases including carbon dioxide, water vapour, methane and nitrous oxides. These gases trap the sun's heat in the Earth's atmosphere, acting like a lens in a magnifying glass, and increasing the heat of the sun ("global warming"). This is called the "greenhouse effect".

In 2005, thirty industrialized countries engaged to meet quantitative targets for reducing or limiting emissions of greenhouse gases (the Kyoto Protocol). [1] In December 2011, the United Nations conference on climate change, held in Durban (South Africa), led to the adoption of a roadmap for an agreement to establish by 2015 a global pact to reduce emissions of greenhouse gases, which would entry into force in 2020. The text included for the first time all the countries worldwide in the fight against global warming, but it did not provide legal constraint, or actions to reduce emissions of greenhouse gas and limit global warming below the threshold 2 °C.

Finally, the energy demand worldwide is continuously increasing due to the increase in population and the fast economic growth of countries such as Brazil, India and China. At the time this thesis is written, these countries have adopted a very similar energy model to the one of Europe and USA, *i.e.* based on low-cost and available energy. Therefore, there is a vital interest to develop eco-friendly new energy resources that are able to face the end of fossil energies (non-renewable energy sources), and that are generated from sources that cannot be depleted (renewable energy sources). New solutions need to be developed and implemented at a large scale to use the power of sun, wind and water, and to convert it into a secondary energy source such as electricity [3].

## B. Promising renewable energies

---

[1] In 2010, 168 countries had ratified the protocol.

Solar energy is actually considered as the most promising renewable energy. It is the energy derived from the sun through the form of solar radiation, and it is used in two major ways: solar cell for electricity generation and solar heating [4]. Though the solar energy is clean and abundant, the low energy efficiency of solar cells must be improved. Wind energy is another widely explored renewable energy source [5]. Nowadays, airflows are used to run turbines, and generate clean electricity and offshore farms are developed to sustain more energy. However, wind energy remains limited to the regions where winds are strong and constant, such as coast and high altitude sites. Finally, biomass, geothermal, ocean energy and other potential clean energy sources are still far away from massive application.

## C. Fuel cells and the hydrogen energy

For both renewable and non-renewable energy sources, the energy produced needs to be stored so as to be delivered in an easily usable form. A promising approach is based on the use of electrolysers that can store electricity by producing hydrogen and oxygen from water electrolysis, and later produce power when the molecules recombine to make water in a fuel cell. Indeed, hydrogen is as an energy rich molecule that allows easy energy conservation and transport (the heat of $H_2$ + $O_2$ reaction at ambient temperature and pressure is 286 kJ $mol^{-1}$) [6]. A fuel cell is a device converting chemical energy of a fuel, for example hydrogen, into electrical energy. The basic fuel cell types span a remarkable range of operating temperatures, and performance specifications [7]. Countries such as Japan, Germany, USA, Canada, France, and Iceland are developing fundamental as well as applied research programs to develop this technology. Although other forms of hydrogen are possible (for example, heating, cooking, power generation, aircraft, locomotives), a major use for fuel cells is in portable and mobile applications (cars, trucks, buses, taxis, motorcycles) in which compact and efficient power sources are needed.

# II. Proton exchange membrane fuel cell

## A. Historical notes

The discovery of the principle of the fuel cell is due to Christan Friedrich Schönbein, Professor at the University of Bâle, who reported on the reaction of hydrogen and oxygen on Pt electrodes [8]. Between 1839 and 1842, Sir William Robert Grove documented a series of experiments on an invention which he termed “gaseous voltaic battery”, composed of one pair of Pt electrodes and acidic solution [9, 10]. The first large boost in fuel cell technology happened in the end of 1950s and the beginning of 1960s. In 1962, a proton-exchange membrane fuel cell (PEMFC) designed by scientists working at General Electric (GE) was used as the power supplier of Apollo U.S. manned lunar landing spacecraft [8]. Since that time, the rapid development of the PEMFC technology led to expectations of rapid and wide commercialization. For application in the areas of transportation and stationary, portable and micro powered PEMFCs offer unique and favourable advantages over chemical batteries in terms of efficiency, energy density, zero or low gas emissions.

## B. Working principle

In a PEMFC, the hydrogen oxidation and the oxygen reduction reactions are performed separately at two electrodes: the anode and the cathode, respectively (Figure I-1). At the anode, the hydrogen oxidation reaction (HOR - Reaction 1a) produces protons and electrons, which are then used to reduce oxygen into water at the cathode (oxygen reduction reaction, ORR – Reaction 1b). Protons are transported from the anode to the cathode via the proton-conducting membrane, electrons going through an external circuit.

$$O_2 + 2H_2 \rightarrow 2H_2O \qquad \text{Equation I-1}$$

$2H_2 \rightarrow 4H^+ + 4e^-$ Equation I-1a

$O_2 + 4e^- + 4H^+ \rightarrow 2H_2O$ Equation I-1b

The key component of a PEM fuel cell is the Membrane Electrode Assembly (MEA). This is multi-layered sandwich material composed of catalytic layers (CLs), where electrochemical reactions occur, gas-diffusion layers (GDLs), enabling the fuel/oxidant transport to the CLs, water management and electron/heat conduction, and a proton exchange membrane (PEM). The PEM, usually a perfluorosulfonated ionomer such as Nafion®, acts as a proton conductor and prevents direct recombination of the reactants (low gas permeability). The CLs are constituted of Pt-based nanoparticles (electrocatalyst) supported on carbon (black, fibres or nanotubes), together with the recast Nafion® ionomer network. They are used to accelerate the reaction kinetics. The role of Nafion® consists of holding the catalyst particles together, forming a continuous pore-volume network, and providing a path for proton transfer. The number of electrochemically active Pt sites is one of the effective factors for fuel cell electrode reactions (Figure I-1). Usually, a large number of electrochemically active Pt sites (electrochemical active surface area, ECSA) translates into a high performance of the fuel cell electrodes. For operation with pure $H_2$, carbon-supported Pt nanoparticles (referred to as Pt/C in what follows) are classically used at the anode but Pt-Ru/C, Pt-Sn/C or Pt-Mo/C offer better performance in CO-contaminated $H_2$ or for direct alcohol oxidation. At the cathode, Pt may be alloyed with a 3d-transition metal (referred to as Pt-M/C in what follows) to improve its ORR performance, and to decrease the electrocatalyst cost. The working principle of a polymer electrolyte fuel cell is illustrated in Figure I-1.

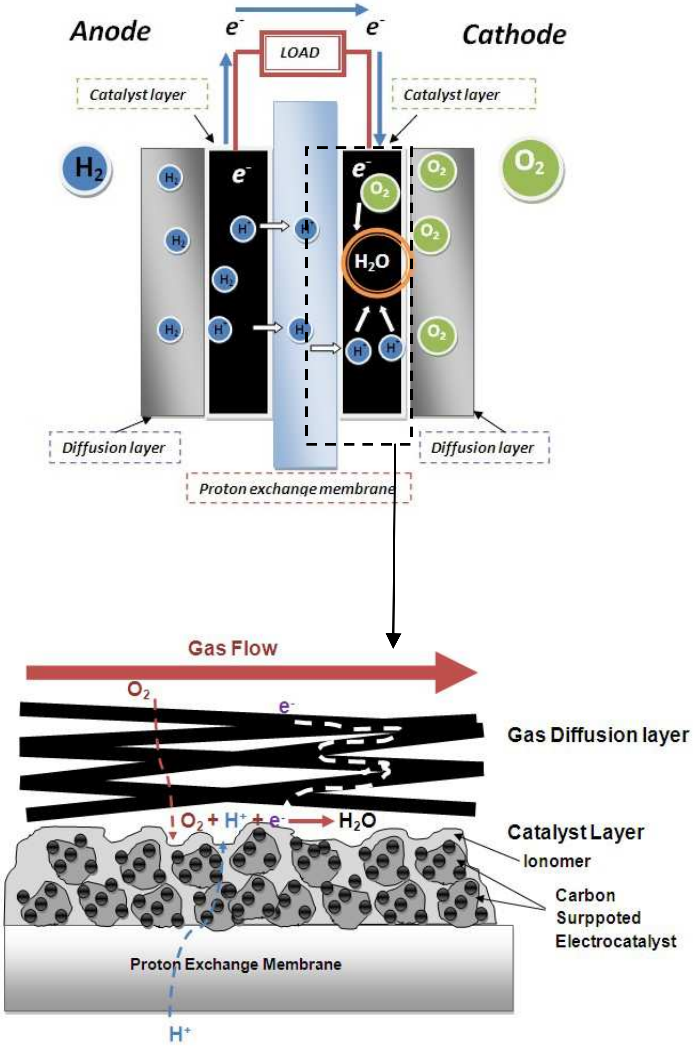

Figure I-1. Schematic description of an hydrogen / oxygen fuel cell and the structure of PEM catalyst.

## III. Issues for practical PEMFC applications

Although PEMFC now possess sufficient initial electrical performances for industrial deployment, [11, 12] they still face several hurdles such as their high cost per kW and their lack of reliability and durability, which is the focus of this Ph.D. Cost issues are primarily due to the use of precious metal catalysts in the catalytic layers. The cost of a 80 kW automotive proton-exchange membrane fuel cell system operating on direct hydrogen and projected to a manufacturing volume of 500,000 units per year was 61 \$ $kW^{-1}$ in 2009 technology and in 2009 dollars, and for 2015 the US Department of Energy targets to reduce this cost to 30 \$ $kW^{-1}$ in order to compete with internal-combustion engines [13]. The poor durability of PEMFC materials is another key issue preventing the wide commercialization of PEM fuel cells.

## A. High cost of PEMFC materials

Figure I-2 shows the cost ratio of the main components of a PEMFC. Proton exchange membranes, precious metal catalysts (typically Pt or Pt alloys), gas diffusion layers, and bipolar plates account for 70% of the total cost of the system [2, 13]. The price of the electrocatalysts dominates the total fuel cell cost. During the last 30 years, some solutions for reduction of the cost of catalyst have been put forward: exploration of non-noble electrocatalysts and reduction of the Pt loading.

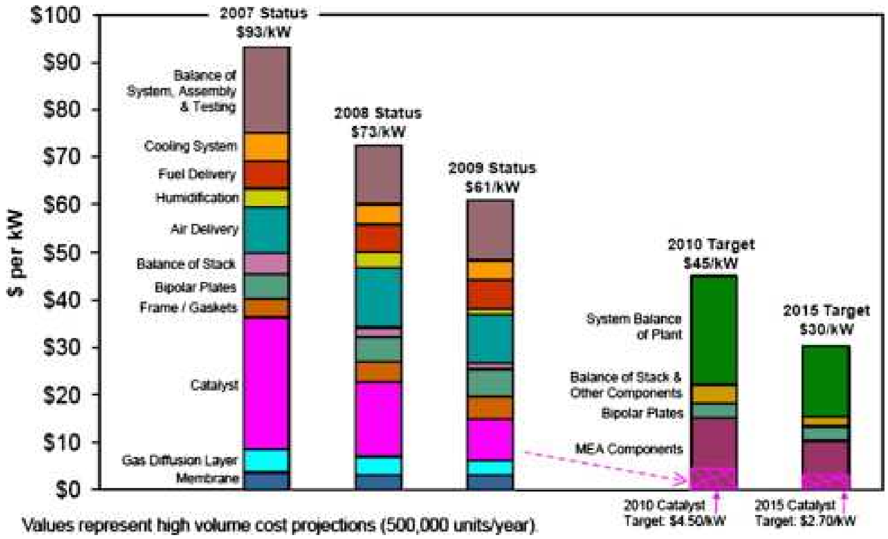

Figure I-2. Fuel cell cost ratio of major components and its breakdown. Reprinted from Ref. [13].

Firstly, large efforts have been made to find non-noble metal catalysts including: transition metal chalcogenides and heat-treated nitrogen containing complexes [14].

Bashyam and Zelenay examined the activity of cobalt–polypyrrole–carbon composite catalysts, which feature good activity and stability in PEM fuel cells, and generated a peak power density of 0.14 W $cm^{-2}$ [15]. Bezerra *et al.* [16] reviewed the study of heat-treated Fe and Co-N/C catalysts. Though remarkable progresses have been made this field, any of these catalysts has reached the level of a Pt-based catalyst in terms of catalytic activity, and chemical/electrochemical stability. Transition metal oxides, such as perovskite, are also interesting candidates to replace Pt in PEMFC catalytic layers but they are unstable in the PEM fuel cell environment [14]. Reeve *et al*. [17] observed that in acidic solutions, the activity declines substantially, and the stability of the oxide phase is very poor. The slow dissolution of the metal components of the oxide and their re-deposition at the anode caused severe cumulative poisoning problems.

Secondly, recent studies of Gasteiger *et al.* [11, 18], Brault and Coutanceau [19-21] and Billy *et al*. [22] have demonstrated that MEAs using Pt loading below 200 $\mu g_{Pt}$ $cm^{-2}_{geo}$ at the cathode could still withstand comparable cell performances under $H_2$/Air with respect to conventional MEAs. At the anode, the Pt loading can even further be reduced to 35-50 µg of Pt per $cm^2$ without any voltage loss. Decreasing the Pt/C particle size may also enable to expend the Pt surface area / Pt mass (cost) ratio, but such strategy is not always beneficial, since the structure sensitivity of the fuel cell reactions yields lower kinetics on small carbon-supported nanoparticles [23]. Finally, many research programs are currently being conducted on alloys composed of Pt and a non-noble metal [11]. Mukerjee and Srinivasan [24] first investigated the ORR kinetics on some binary alloys of Pt (PtNi, PtCr and PtCo). Their results revealed enhanced electrocatalytic activities, lower activation energies and different reaction orders for all the alloys relative to pure Pt. They bridged the increase in oxygen reduction reaction catalytic activity to both electronic (the higher Pt 5d-orbital vacancies) and geometric factors (shorter Pt–Pt bond distances), and stressed the importance of surface-blocking spectator species such as oxygenated species. At the anode, several Pt-M alloys exhibit better activity than Pt for methanol and hydrogen electrooxidation: PtRu [25], PtSn [26] PtCo [27] and PtPd [28].

However, though these alloying materials show efficient activity for fuel cell reactions, comparing to Pt, their stability is much lower in electrochemical environment [29-37].

## B. Low durability of PEMFC materials

The low durability of the MEA is another serious problem preventing the wide commercialization of PEMFCs. Since the degradation of the PEM, of the CL and of the GDL are correlated [38], the phenomena are difficult to evaluate separately.

### 1. Degradation of the bipolar plates

Bipolar plates are key components used to distribute the hydrogen and oxygen gases, collect water exiting the cell, and the current generated through the electrochemical reactions at the anode/cathode. Because of the harsh working environment of the PEMFC, bipolar plates should exhibit high corrosion resistance, appropriate mechanical properties, good thermal and chemical stability, and low ohmic resistance [39, 40]. Many kinds of materials have been evaluated as bipolar plates, including metals, carbon, carbon/graphite-based composites, and organic polymer based materials [41, 42]. Graphite and graphite composites are most used for their favourable properties such as good electrical conductivity, inertia to chemicals, and low density. However carbon oxidation/corrosion easily occurs in extreme operating conditions such as cell reversal [43].[2] Therefore, the focus is presently on metallic bipolar plates that may also suffer the same problem of corrosion, [42] yielding metallic cations release and increased contact resistance.

### 2. Degradation of the gas-diffusion layers

The GDL is a porous substrate pressed onto the CL: this is the channel for the gas/water transport, electronic/heat conduction and the mechanical protection of the

---

[2] Cell reversal occurs when the fuel cell stack is loaded and not enough fuel is supplied to the anode. Drawing excessive current from any one cell more than its fuel delivery can lead to cell reversal.

CL. Generally, the GDL is a porous carbon fibber/cloth covered by a mixture of porous carbon powder and a hydrophobic agent (polytetrafluoroethylene). In addition to a bulk hydrophobic treatment, GDLs are often coated with a microporous layer (MPL) on their catalyst-facing side, [44-46] to aid liquid water transport and current collection. When a MPL is added between the CL and GDL, the liquid saturation is redistributed across the MPL and GDL to improve the water management within the PEM fuel cell. Several mechanisms of GDL degradation have been proposed in the literature including: mechanical degradation [47], carbon corrosion [48, 49], and hydrophobic agent decomposition [50]. Most of them cause hydrophobicity loss and changes in the GDL pore structure, resulting in an increase in the water content of the GDL and the MPL and thus impeding gas phase mass transport [51-53]. It should be noted that the carbon fibres of the GDL and the carbon black particles of the MPL are more stable than the carbon black in the CL due to the absence of Pt that can catalyse the electrochemical oxidation of carbon [54]. However, chemical surface oxidation of carbon by water proceeds [48, 49].

## 3. Degradation of the proton-exchange membrane

The proton exchange membrane is a thin layer of solid electrolyte, which conducts protons from the anode to the cathode, while preventing electron transport and the cross-over of fuel molecules from the anode and oxygen reactant from the cathode. Proper membrane material requires high ionic conductivity, chemical stability in an acidic environment, thermal stability throughout the operating temperature, and good mechanical toughness. Nafion®, which was developed by the DuPont® Company in the 1960s, is based on perfluorosulfonic acid and is extensively used for its good performance in PEM fuel cell operation conditions. However, in operating conditions, Nafion® membranes degrade by several mechanisms including modification of the chemical and mechanical properties, and thermal decomposition [55-57]. Mechanical degradation includes the formation of cracks, tears, punctures, and pinholes due to the presence of foreign particles or fibres introduced during the MEA fabrication process that might perforate the membrane, and facilitate the gas crossover. Chemical degradation originates from chemical attack by hydrogen peroxide radicals, resulting in breakage of the membrane's backbone and side-chain groups and subsequent loss of mechanical strength and proton conductivity, thus leading to an increase in resistance and declining cell performance. It is currently admitted that chemical degradation, leading to ionomer damage and loss in PEM functionalities, results from a chemical attack initiated by active oxygen species [29]. Such species as $HO^{\bullet}$ and $HO_2^{\bullet}$ originate from the hydrogen peroxide that is generated through incomplete reduction in the ORR [58]. These radical species attack the polymer end groups that are present in the membrane yielding release of organic moieties and fluoride in the cathode outlet water [59]. Nevertheless, the fluoride emission rate strongly depends on the gas nature and decreases with increasing the current density [29]. Thermal degradation occurs when the membrane becomes dehydrated due to high-temperature operation, low humidity, and other causes, and leads to the loss of proton conductivity [43, 57].

## 4. Degradation of the catalytic layers

Catalyst layer degradation is one of the most critical reasons leading to the lack of stability of the MEAs [60]. In the PEMFC CL, the catalysts can be classified into three groups based on catalyst material [61]: Pt catalyst; Pt catalysts alloyed with another metals, such as Au, Ag, W, Fe, Cr, Cu, Co, Ru and non-Pt catalysts such as non-noble metals and organ metallic complexes. Although a variety of catalysts have been investigated so far, Pt/C and Pt-alloyed catalysts are still the most popular catalysts in use due to their low over potential and high catalytic activity for the hydrogen oxidation reaction (HOR) and the oxygen reduction reaction (ORR) as well as their stability in the harsh acidic environment.

In the literature, the stability and degradation of Pt catalysts, Pt-alloy catalysts and non-Pt catalysts on PEMFC catalyst materials has been reviewed by many excellent articles [11, 29, 62, 63]. Antolini *et al*. [63] also gave an useful introduction about the stability of Pt alloy catalysts focusing on the first row transition metals. The degradation mechanisms of Pt-based catalysts under harsh operating conditions were reviewed by Shao *et al*. [64]. The authors introduced some approaches to improve catalyst durability with alloyed Pt nanoparticles supported on highly graphitized carbons. Zhang *et al*. [65] discussed the degradation of Pt nanoparticles and of the carbon support under different accelerated processes in PEMFCs. Schmittinger and Vahidi [55] presented the effects of corrosion and contamination of the electrocatalyst in both the anode and cathode sides. Rama *et al*. [66] summarized the catalyst resulted activation losses and classified them into effects due to the Pt catalysts, geometric structure of the CLs and carbon support. These review articles contributed to the improvement of PEMFC degradation issues. However, a sufficient understanding of basic Pt catalysts degradation mechanisms is still required.

## IV. Degradation mechanisms of the Pt/C catalysts in PEMFC CLs

The degradations of the PEMFC catalytic layers are usually associated with a loss of the electrochemically active surface area of Pt/C (or Pt-M/C, where M is a transition metal) electrocatalysts. The physical characterizations performed on aged CLs evidenced Pt particle size growth and disappearance of the smallest particles as the two main morphological changes. However, the reasons accounting for the increased Pt particle size remain highly debated. It is now well-established that four main degradation mechanisms are at work: (i) metal nanoparticle aggregation and/or detachment [67-71], (ii) corrosion of the high surface area carbon support [38, 54, 67, 72-74], (iii) 3D Ostwald ripening, where the smallest Pt crystallites dissolve preferentially, yielding the formation of $Pt^{z+}$ ions and their redeposition onto larger particles [29, 67, 75]; and (iv) chemical reduction of the $Pt^{z+}$ ions in ion conductors, leading electrically disconnected Pt crystallites [29, 67, 75]. This is schematically illustrated in Figure I-3.

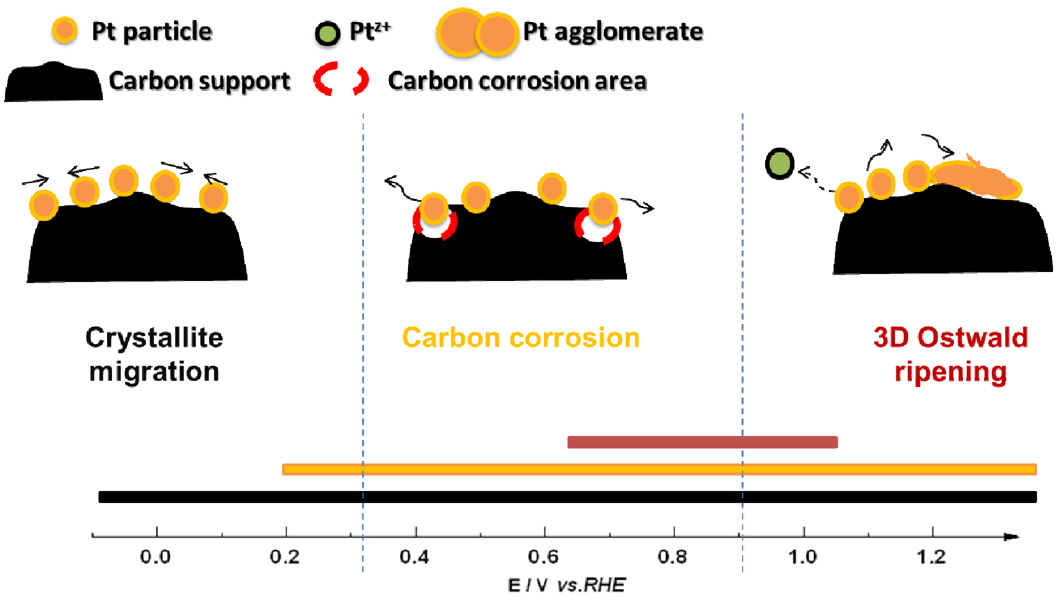

Figure I-3. Basic degradation mechanisms of Pt/C catalysts. Adapted from Ref. [75].

## A. 3D Ostwald ripening

3D Ostwald ripening is due to the Pt atoms dissolution from the smallest nanoparticles, diffusion of the Pt$^{z+}$ ions in the electrolyte and redeposition onto larger Pt particles. This process is driven by the reduction of the total surface energy of the Pt nanoparticles. In acidic solution (*e.g.*, 0.5 M $H_2SO_4$ [76] or 0.57 M $HClO_4$ [77]) the dissolution rate of a platinum wire electrode increases with increasing potentials from 0.65 to 1.10 V *vs*. the standard hydrogen electrode (SHE) and is logarithmically dependent on potentials in the 0.85 - 1.1 V region [77]. Above 1.1 V *vs*. SHE, the dissolution rate decreases, which is attributed to the formation of a protective Pt oxide film [77]. For Pt/C, the dissolution rate of Pt at 0.9 V *vs*. SHE is comparable with that of a Pt wire electrode, and increases monotonously with increasing potential (0.6–1.2V *vs*. SHE) [64]. Cycling the potential between the oxide formation and reduction regions leads to higher dissolution rates than potential holding in the oxide formation region, with the latter being three to four orders of magnitude lower than the former [77]. This is Pt$^{z+}$ ions are believe to be released in electrolyte during the negative potential sweep

[64, 78, 79]. The $Pt^{z+}$ ions may (i) diffuse and redeposit onto larger Pt crystallites, leading to the growth of the average Pt particle size and particle "necking"; (ii) redeposit onto the support carbon to form a new Pt particle; (iii) be reduced in the ionomer to form electrically disconnected Pt nanoparticle.

## B. Corrosion of the carbon support

The most used support material for Pt-based electrocatalysts in PEM fuel cells is high surface area carbon. However, carbon materials are thermodynamically unstable in the PEMFC cathode environment (the thermodynamic potential at standard conditions for the carbon corrosion reaction ($C+H_2O \rightarrow CO_2 + 4H^+ + 4e^-$) is 0.207 V *vs*. RHE), [80] yielding detachment of the Pt-based nanoparticles [67, 76]. Investigations on the dependence on the potential of the anodic oxidation of carbon electrodes using differential electrochemical mass spectroscopy (DEMS) showed that pure carbon was oxidized at potentials higher than 0.9 V *vs*. RHE (with $CO_2$ and, to a lesser extent, CO being the main products), and that Pt nanoparticles catalysed the oxidation of a oxygen-containing carbon surface groups ($CO_{surf}$) to $CO_2$ at potentials between 0.6 and 0.8 V *vs*. RHE, with the $CO_{surf}$ being formed on the carbon at $E > 0.3$ V *vs*. RHE [81]. Stevens *et al*. [48] explored *ex situ* and *in situ* fuel cell catalyst degradation test methods as well as the impact of catalyst degradation on fuel cell performance. A series of Pt-loaded carbons with two different carbon supports were aged *ex situ* in an isothermal oven and *in situ* using a 1.2 V *vs*. RHE PEM fuel cell accelerated test. It was also argued that, in the presence of water, carbon can also be consumed through the heterogeneous water-gas reaction: $C + H_2O \rightarrow H_2 + CO$. Recently, Maillard *et al*. [54] investigated the role of Pt in the corrosion of carbon by Fourier-transformed infrared spectroscopy coupled *in situ* with electrochemical measurements. The authors showed that carbon surface oxide species (*e.g.*, phenol, ether, carboxylic and carbonyl groups), formed at low electrode potential $E < 0.60$ V *vs.* RHE, spill over back from the carbon support to the Pt nanoparticles, where they are converted into CO and then slowly oxidized into $CO_2$. At higher electrode potential $E > 0.60$ V *vs.* RHE, oxygenated species resulting from water splitting on Pt facilitate the removal of these carbon surface oxides species yielding increased kinetics for carbon corrosion. Oxygen-containing groups were also detected on the carbon surface by other techniques [49, 82, 83]. These oxygen-bearing groups are believed to decrease the conductivity of the catalytic layers and weaken the interaction between the support and the catalytic metal nanoparticles, which results in an accelerated sintering [82, 83]. Many authors agree that the carbon corrosion rate is catalysed by Pt, indeed, the higher the Pt loading, the larger the interfacial area between the Pt nanoparticles and carbon and the larger fraction of the carbon is in the "reactive zone" [48, 54, 72, 84, 85]. Finally, the extent of graphitization of the carbon plays an important role on carbon support stability, with more graphitic carbons being more thermally and electrochemically stable [86, 87]. This is due to the decreased density of defect sites where carbon oxidation initiates.

## C. Migration of Pt nanocrystallites

Pt crystallites are not immobile on a carbon support but can collide and aggregate under PEMFC operating conditions. The movements of Pt crystallites on the carbon surface can be described as Brownian motions, which are potential independent. This degradation mechanism is influenced by many factors such as: Pt particle size[88], Pt loading, [71] flatness of the carbon surface [88] and stability of the carbon support [89]. Size-dependent mobility of Pt clusters on a graphitic carbon surface was estimated by Chen *et al.* using molecular dynamics simulations [88]. The mobility is fast ($10^{-11}$ $m^2$ $s^{-1}$) for Pt clusters with less than 40 atoms but decreases rapidly with a decrease in the Pt particle size. The diffusion coefficient of larger clusters has variable size-dependence with local minima at cluster sizes of 50 and 300 Pt atoms and a local maximum at cluster size of 100 atoms. In addition to the overall size of the Pt clusters or nanoparticles, the mismatch between the bottom layer of Pt and graphite also affects the overall Pt–graphite affinity and hence the Pt cluster mobility. Unlike graphite carbon with a well-defined planar geometry, common high surface area carbon supports, like Vulcan 72 have more complex structures. Generally, in order to obtain homogeneous Pt particle dispersion, porous carbons are considered to be better than graphitic carbon. Indeed graphite or low surface area carbon supports can limit Pt dispersion and adherence on the carbon surface [87]. However, a compromise must be found between porosity (stabilization of the Pt nanoparticles) and degree of graphitization (resistance to corrosion). Recently, carbon nanotubes and carbon nanofibres were tested as support materials for fuel cell catalysts [90-92]. From traditional carbon materials utilized in fuel cell electrocatalyst, these materials are distinguished by their high extent of structural order. Moreover, their tunable mesoporosity confers them enhanced mass transport capabilities [93].

# V. Structural markers of Pt/C degradation

## A. Physical markers

### 1. Pt crystallite/particle growth

The growth of Pt nanocrystallites/nanoparticles is a common evidence of Pt/C degradation. Two conventional methods may be used to determine the particle size: X-ray diffraction (XRD) and transmission electron microscopy (TEM). X-ray diffraction was first employed by Wilson *et al*. to determine the change of the Pt crystallite size during long-term PEMFC operation [118]. Later, this method was employed by many groups to build the grain size distribution (GSD), and characterize the crystallite growth mechanisms in various fuel cell operating environments, including cyclic and transient conditions [118-120]. More often, research groups determine the variations of the mean particle size established by transmission electron microscopy. Xie *et al*. [59] performed single cell durability testing, and found that the size of the cathodic catalyst grew after over 1000 h of testing in drive cycle experiments. When cells were cycled to potential range over 1 V, extremely rapid cathode particle growth was observed. Ferreira *et al*. [76] found that Ostwald ripening dominates the degradation of the cathode catalyst layer, and yields larger mean particle size and broader Gaussian size distribution than what was expected.

## 2. Aggregation of Pt nanoparticles

During crystallite migration, crystallites collide, form aggregates and eventually coalesce to form larger crystallites. Consequently, the fraction of "isolated" particles (*i.e.* spherically-shaped and non-aggregated) decreases at the expense of the fraction of aggregated particles. Those changes can be imaged and quantified by a proper analysis of representative TEM images. From this analysis, (i) the number and the surface averaged mean particle size, (ii) the density of isolated/aggregated nanoparticles, (iii) the total particle density defined as the sum of isolated and aggregated nanoparticles per $\mu m^2$ of the carbon support, (iv) the fraction of aggregated particles and (v) the percentage of lost isolated particles during the electrochemical treatment, can be determined.

## 3. Particle detachment

The detachment of Pt nanoparticles from the carbon surface is also commonly observed during PEMFC operation [67] or upon accelerated ageing tests, especially in conditions where the carbon supported is strongly corroded [68, 73, 121, 122]. In two recent studies, Mayrhofer *et al*. [68, 121] argued that detachment of Pt nanoparticles and crystallite migration/coalescence are the main degradation mechanisms, and that Pt dissolution/redeposition plays a minor role in the variations of ECSA losses (liquid electrolyte). The authors argued that during potential cycling, a partial oxide layer forms between the Pt particles and the carbon support, leading to a gradual reduction in adhesion and finally to the complete detachment of particles. However, it is worth noting that catalyst degradation was observed only when the sample was cycled 3600 times to high electrode potentials of 1.4 V *vs*. RHE (and not with upper limits of 1.05 or 1.20 V *vs*. RHE). Detached Pt particles were visible in identical-location TEM images because they lied onto the carbon membrane of conventional TEM grids.

## B. Electrochemical markers of Pt/C degradation

The surface reactivity of Pt-based catalysts is closely related to their structure (size, shape, degree of aggregation), making the adsorption/desorption of H, O and CO molecules ideal structural markers to unveil the morphological changes encountered by Pt nanoparticles during accelerated ageing tests.

### 1. Adsorption/desorption of H/O

Figure I-4 shows cyclic voltammograms (CVs) of model Pt nanoparticles with various mean particle sizes ranging from 1.8 nm to 2.8 nm and aggregated particles supported on a glassy carbon (GC) substrate. CVs for Pt nanoparticles can be divided into three characteristic potential regions: (i) $H_{ads}$ / $H_{des}$ region ($0.05 < E < 0.40$ V *vs.* RHE), (ii) double-layer region ($0.40 < E < 0.60$ V *vs.* RHE) and (iii) the surface oxide formation/reduction region ($E > 0.7$ V *vs.* RHE).

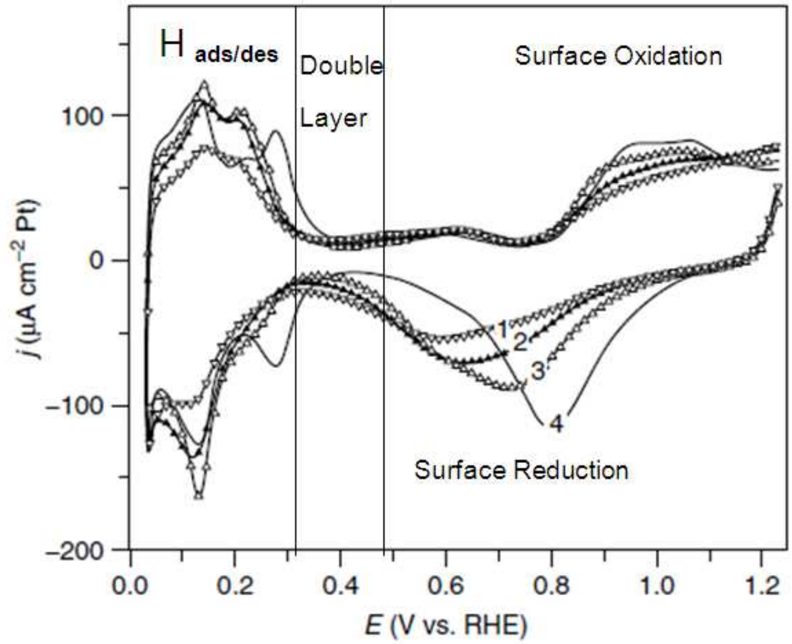

Figure I-4. CVs of Pt/C catalyst with different mean particles sizes $\overline{d}_N$ =1.8 nm (1), 2.4 nm (2), 2.8 nm (3) and Pt electrodeposited on glassy carbon (4). 0.1M $H_2SO_4$; *v* =0.1 V $s^{-1}$. Figure reprinted from Reference [23].

As previously proposed [123, 124], the peaks located at *E* =0.13 V *vs.* RHE are attributed to the adsorption/desorption of H on/from Pt(110) sites, and the peaks at *E* = 0.22 – 0.28 V *vs*. RHE on/from Pt(100) and Pt(111) sites. With an increase of the Pt particle size, the intensity of the $H_{ads}$ peaks at *E* = 0.22 and 0.28 V *vs.* RHE develop, which is indicative of the increased contribution of the (100) and (111) facets (terraces) and a decrease of the contribution of edge and corner atoms. Furthermore, as the size of Pt crystallites is increased, the oxide reduction peak is shifted towards positive electrode potential. Here, it is wise noting that the shape of CVs is also influenced by several factors such as the nature of the electrolyte (specific adsorption of ions), the sweep rate, the temperature and other operation conditions. In spite of these influences, a CV in supporting electrolyte remains the most rapid and widely used method to evidence morphological changes of Pt nanoparticles.

## 2. Electrooxidation of a $CO_{ads}$ monolayer (CO stripping)

CO stripping voltammetry is widely employed to estimate the electrochemically active surface area of Pt-based electrocatalysts [125]. Numerous investigations of CO oxidation on noble metal surfaces have proven that the reaction follows the Langmuir–Hinshelwood mechanism at electrode potential *E* > 0.60 V *vs*. RHE, both under chemical and electrochemical conditions [126]. The reaction scheme for the electrochemical CO oxidation is given by the following equations:

$$H_2O + * \leftrightharpoons OH_{ads} + H^+ + e^- \qquad \text{Equation I-2}$$

$$CO_{ads} + OH_{ads} \rightarrow COOH_{ads} \qquad \text{Equation I-3}$$

$$COOH_{ads} \rightarrow \rightarrow CO_2 + H^+ + e^- \qquad \text{Equation I-4}$$

Figure I-5 shows the first and the second CO stripping voltammograms recorded on a Pt surface. The hatched region indicates the charge required to desorb a monolayer of hydrogen ($Q_H$) or oxidize a monolayer of CO ($Q_{CO}$), respectively. The ECSA can be determined by integrating the coulometry required to adsorb/desorb under-potentially deposited hydrogen, or electrooxidize a monolayer of carbon monoxide:

$$ECSA_H = \frac{Q_H}{0.21} \qquad \text{Equation I-5}$$

$$ECSA_{co} = \frac{Q_{co}}{0.42} \qquad \text{Equation I-6}$$

Where $Q_H$ and $Q_{CO}$ are the charge required to desorb a monolayer of under-potentially deposited hydrogen or electrooxidize a monolayer of CO, respectively and the values of 0.21 and 0.42 (mC cm$^{-2}$) represent the charge density associated with a one/two electron process, respectively [126].

Furthermore, "CO stripping" is also used as a simple but direct method to probe *in situ* the agglomeration of carbon-supported Pt particles during accelerated ageing tests or PEMFC operation. Indeed, $CO_{ads}$ monolayer electrooxidation is a nanostructure sensitive reaction, which features a CO electrooxidation pre-peak in the presence of Pt nanoparticles featuring surface defects, such as Pt aggregates [127, 128]. The position of this pre-peak is shifted *ca.* 50 mV towards more negative potential with respect to the position of the main CO electrooxidation peak (corresponding to $CO_{ads}$ electrooxidation on "isolated" Pt/C particles). Additionally, the position of the main $CO_{ads}$ stripping peak strongly depends on the mean particle size and shifts toward more negative potential when increasing the Pt particle size [126, 128, 129]. Maillard *et al*. first reported the effect of the Pt particle sizes on the kinetics of the $CO_{ads}$ monolayer electrooxidation. A pronounced size effect was observed on the reaction kinetics in the particle size range from 1 to 4 nm, including positive shift and broadening of the $CO_{ads}$ stripping peak and increase of the tailing current with a decrease of the particle size (see Figure I-6.). Later, the shift of the CO electrooxidation peak towards more positive electrode potentials with a decrease of the Pt particle size was confirmed by several different groups [130-134].

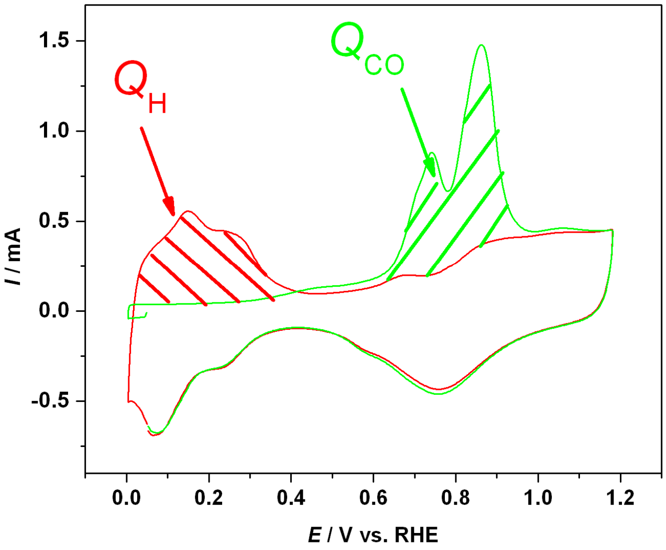

Figure I-5. The first and the second CV scan in CO-free at Pt/GC after CO adsorption. The hatched areas show $H_{upd}$ ($Q_H$) and CO stripping ($Q_{CO}$) charges used to calculate the electrochemically active surface area. 0.1M $HClO_4$ – $v = 0.02$ V $s^{-1}$.

Modelling of chronoamperograms performed by Andreaus *et al.* [135, 136] suggested that $CO_{ads}$ surface mobility is fast ($D_{CO} > 10^{-14}$ $cm^2$ $s^{-1}$) on large Pt particles ($d >$

5 nm), compared to $OH_{ads}$ formation and $CO_{ads}$ + $OH_{ads}$ recombination, and does not fix the reaction rate. As the particle size decreases ($d$ < 1.8 nm), $CO_{ads}$ diffusivity drops down to *ca.* $10^{-16}$ $cm^2$ $s^{-1}$, and hence a current decay is observed in $CO_{ads}$ stripping voltammograms and chronoamperograms.

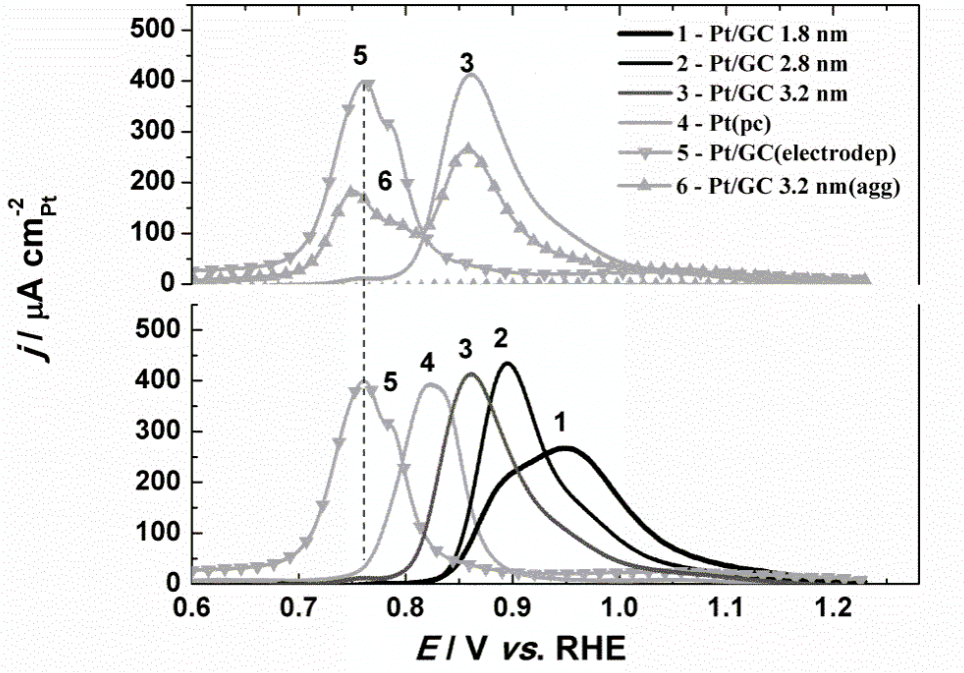

Figure I-6. Background-subtracted $CO_{ads}$ stripping voltammograms in 0.1M $H_2SO_4$ at the sweep rate of 0.1 V $s^{-1}$ for model Pt/GC electrodes with Pt mean particle sizes $\overline{d}_N$ 1.8 (1), 2.8 (2), 3.2 nm (3), polycrystalline Pt foil (4), Pt electrodeposited on GC comprising multi-grained Pt with the grain size of *ca.* 5 nm (5). Curve (6) corresponds to Pt/GC sample containing single-grained Pt particles with the average size 3.2 nm along with multi-grained Pt structures. Replotted from Ref. [23] with permission of the author.

# VI. Conclusions

In this chapter, we underlined the importance to develop an hydrogen economy in which low temperature PEM fuel cells provide the final step. Their working principle, their main components as well as the major research hurdles that prevent wide commercialization (cost of materials, lifetime) were surveyed. We also defined physical and electrochemical structural markers to monitor the changes in morphology of Pt/C nanoparticles observed during PEMFC operation or accelerated aging tests. Finally, despite large research efforts achieved during the last decade, the degradation mechanisms of PEM fuel cell materials require additional research and understanding. In particular, some questions remain unanswered and will be the focus of this PhD:

1. Can we separate the contribution of the main degradation mechanisms of Pt/C nanoparticles (crystallite migration/aggregation, Ostwald ripening, carbon corrosion) in a model catalytic layer?
2. In specific operating conditions (temperature, potential range, relative humidity), is there an influence of the gas atmosphere on the Pt/C degradation mechanisms?
3. What is the nature of the interactions existing between the Pt nanoparticles and the high surface area carbon support?
4. What is the mechanism of the electrochemical oxidation of conventional carbon blacks used to support the Pt nanoparticles?
5. During PEMFC operation, the density of isolated Pt nanoparticles decreases at the expense of aggregated Pt nanoparticles: how does this impacts the kinetics of the oxygen reduction reaction?
6. Considering the above, can we improve the stability of the Pt/C electrocatalysts currently used in PEMFCs?

# CHAPTER II - EXPERIMENTAL

# I. Electrocatalysts

## A. Pt/XC72 nanoparticles (E-TeK, Inc.)

Three samples based on Pt nanoparticles supported on Vulcan XC72 (a carbon black of specific surface area $S_c$~ 250 $m^2$ $g^{-1}$) were used to investigate the migration/detachment of Pt crystallites on/from high surface area carbon supports. They were supplied by E-TeK and have different weight fractions (wt. %) of 20, 30 and 40 %, translating into surface-averaged mean particle size of 2.9, 3.4 and 4.7 nm, respectively as well as different fraction of isolated/agglomerated particles. Generally speaking, the fraction of agglomerated particles increases with an increase of the Pt wt. % in E-TEK electrocatalysts, as it will be shown in Chapter III. The catalysts were used as-received without any further treatment.

## B. Pt/Sibunit nanoparticles

Pt nanoparticles supported on Sibunit, a carbon with a specific surface area of $S_c$ ~6 $m^2$ $g^{-1}$ were prepared by Dr. P. Simonov at the Boreskov Institute of Catalysis in Novosibirsk (Siberia). Carbons of Sibunit family are prepared through pyrolysis of natural gases on carbon black surfaces followed by an activation to achieve desired values of the surface area and pore volume [1, 2]. Pyrolysis leads to formation of dense graphite-like deposits, and in the course of the activation procedure, the carbon black component is removed first. Hence, the pore size distribution in the final Sibunit sample roughly reproduces the particle size distribution in the carbon black precursor [1]. Thus, varying the type of the gas source, the template (carbon black), and the manner and duration of the activation, enables production of meso- or macroporous carbon materials with surface areas from 1-50 (non-activated) to 50-500 $m^2$ $g^{-1}$ (activated) and pore volume up to 1 $cm^3$ $g^{-1}$. The advantage of carbons of the Sibunit family is their chemical purity, high electrical conductivity and uniform morphology of primary carbon globules (contrary to carbon blacks, in particular Vulcan) [3]. Pt supported on Sibunit electrocatalysts (Pt/Sibunit) were prepared via the polyhydroxo complex route using a procedure similar to that described in Ref. [2]. Before their use in electrochemistry, the Pt/Sibunit powders were reduced for 2 hours under $H_2$ atmosphere at *T* = 250 °C. The reduced electrocatalysts have different weight fractions of 1.5 and 5 wt. %, translating into surface averaged particle size of 1.5 nm and 3.7 nm, respectively.

### C. Pt nanowires supported on Vulcan XC72 (Pt NWs/XC72)

Pt nanowires (Pt NWs) were prepared by a soft template based phase-transfer method [4]. Briefly, 10 mL of a hexachloroplatinic (IV) acid hydrate ($H_2PtCl_6 \cdot x\ H_2O$, > 99.9%, Aldrich) solution (20 mM, aqueous) was mixed with 10 mL of chloroform containing 40 mM cetyltrimethylammonium bromide (CTAB, Acros) while stirring at 1000 revolutions per minute (rpm) for 1 h. After quiescence for 3 h, 80 mL of deionised water and 10 mL of ice-cold sodium borohydride (300 mM) solution were added drop by drop under stirring at 1000 rpm. After that addition, a 30 minute period of time was used to ensure that the $Pt^{4+}$ ions were completely reduced (change of the solution colour from orange to dark brown). After filtration, Pt nanowires were washed four times with 200 mL boiling methanol and 1000 mL hot deionized water to ensure complete removal of the CTAB surfactant. The Pt nanowires were then mixed with deionised water and Vulcan XC72 and ultrasonically treated for 30 min to yield Vulcan XC-72 supported Pt nanowires (Pt NW/XC72). The resulting Pt NW/XC72 powder was dried in an oven at *T* = 100 °C for 12 h before its use in electrochemistry.

## II. Characterization of the fresh/aged electrocatalysts

### A. Physical techniques

#### 1. Transmission electron microscopy

TEM is a routine technique used to probe the crystalline structure of the Pt nanoparticles/nanowires, estimate their size/shape, and determine their extent of agglomeration and their defect density. The catalytic materials that can be probed by TEM should be electron transparent (normally, a few tens of nanometres in thickness), and should not be affected by ultra-high vacuum (implying good contact between the metal particles and the carbon support) nor by the electron bombardment (which may cause local heating and modification of the surface structure). In this work, the metal nanoparticles were examined with a Jeol 2010 TEM operated at 200 kV with a point to point resolution of 0.19 nm. The TEM images were used to build the particle size distribution of the catalysts before/after the electrochemical treatment. For each distribution, at least 400 particles were counted to build the particle size distribution (PSD), the number averaged diameter:

$$\bar{d}_N = \frac{\sum_{i=1}^{n} n_i d_i}{\sum_{i=1}^{n} n_i} \qquad \text{Equation II-1}$$

and the surface averaged diameter:

$$\bar{d}_S = \frac{\sum_{i=1}^{n} n_i d_i^3}{\sum_{i=1}^{n} n_i d_i^2} \qquad \text{Equation II-2}$$

Where $n_i$ stands for the number of particles having a diameter $d_i$). Only “isolated” particles (that is non-agglomerated, single grain spherical nanoparticles) were counted to build the PSD, meaning that the changes of the PSD reflect the changes in size of the isolated Pt particles. From the value of $\bar{d}_S$, the specific surface area of the catalytic particles was calculated:

$$S_{\mathrm{TEM}} = \frac{\beta}{\rho \bar{\mathrm{d}}_{\mathrm{S}}} \qquad \text{Equation II-3}$$

Where ρ is the density of the catalytic material and β is the shape factor. The shape factor is equal to 6 for (hemi) spherical or (truncated) cuboctahedral particles, and is above this value for other shapes. The dispersion of the material (ratio of surface to total number of atoms) varies inversely with the surface averaged mean particle size (for the case of (hemi) spherical Pt particles):

$$D = \frac{1.107}{\bar{d}_S} \qquad \text{Equation II-4}$$

## 2. Identical-location TEM (IL-TEM)

An identical-location TEM method, very similar to that initially developed by Mayrhofer *et al.*, [5, 6] was employed to gain more insights into the degradation of Pt/C electrocatalysts after various ageing treatments. This technique enabled multiple analyses of the same catalyst location during the degradation experiment. It was first introduced in our laboratory by Dr. B. Vion-Dury [7]. The IL-TEM experiments were processed as follows: (i) a small quantity of Pt/C catalyst (5 µL) was first deposited on the top side of a TEM gold grid bearing a lacey carbon membrane. Caution was taken to use small Pt/C loading so as to be able to find “isolated” carbon particles in TEM, (ii) randomly selected carbon particles were imaged at different scales before the electrochemistry experiments (Figure II-1), (iii) the TEM grid was handled carefully with tweezers, inserted between two glassy carbon sheets, which were machined for this purpose. Both plates were held pressed one upon the other by a clamp, (iv) electrochemical experiments were performed using the (glassy carbon plates + gold grid) sandwich as a working electrode, (v) the sandwich was then disassembled and the previously selected areas were imaged in TEM. All IL-TEM experiments presented in this work were performed by Dr. F. Maillard and Dr. L. Dubau.

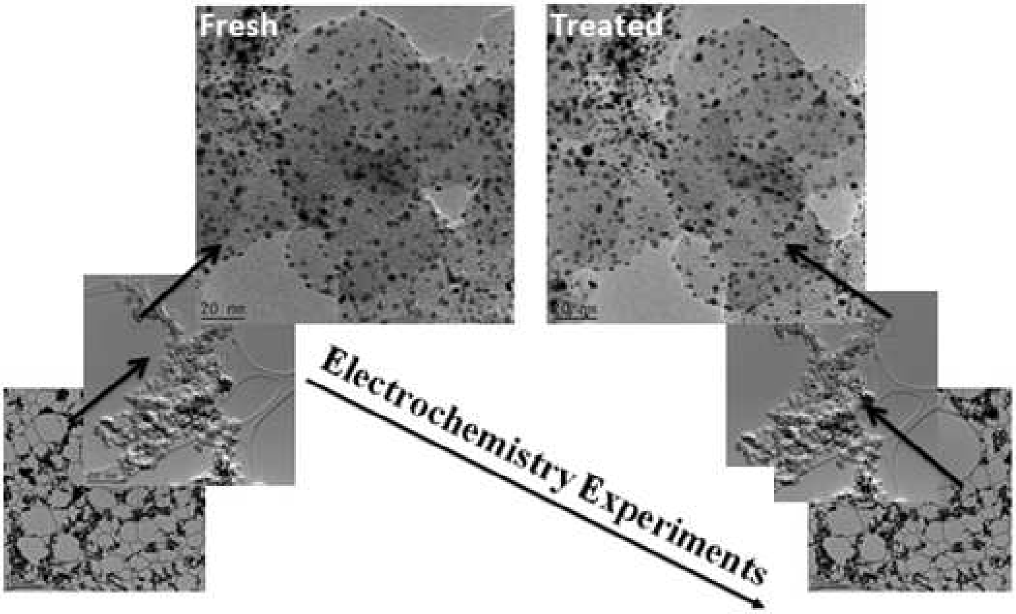

Figure II-1. Schematics of selected zones imaged in the IL-TEM experiments.

## 3. X-ray diffraction

XRD is generally used to estimate the mean crystallite size of single crystalline or polycrystalline materials. The average crystallite size $\bar{d}_{\mathrm{XRD}}$ can be estimated from the peak broadening in the X-ray diffractograms using the Scherrer equation: [8]

$$\bar{d}_{XRD} = \frac{K\lambda}{B(2\theta)\times\cos\theta} \qquad \text{Equation II-5}$$

Where $\bar{d}_{XRD}$ is the crystal dimension normal to the diffracting planes, *K* is the Scherrer constant (*K* = 0.89), $\lambda$ is the X-ray wavelength, $B_{2\theta}$ the integral breath of the diffraction peak in terms of the 2θ angle in radians (the full width at half maximum (FWHM) is frequently used), and θ is the angle at the peak maximum. The mean crystallite size obtained by XRD cannot be directly compared with particle size obtained by other techniques such as transmission electron microscopy or cyclic voltammetry without assuming a suitable model for the particle shape. In the case of spherical nanoparticles, an accurate comparison of $\bar{d}_{\mathrm{XRD}}$ should be made with the volume-averaged mean diameter $\bar{d}_{\mathrm{V}}$ determined by TEM:

$$\bar{d}_{\mathrm{V}} = \frac{\sum_{\mathrm{i}} n_{\mathrm{i}} d_{\mathrm{i}}^{4}}{\sum_{\mathrm{i}} n_{\mathrm{i}} d_{\mathrm{i}}^{3}} \qquad \text{Equation II-6}$$

### 4. Field-emission gun–scanning electron microscopy (FEG —SEM)

SEM is one of the most versatile instruments available to examine and analyse the microstructural characteristics of solid samples [9]. Imaging with SEM consists of sweeping a finely focused electron beam over a bulk specimen. The beam energy typically varies between 1 and 40 k eV. The interaction of the electrons and the sample surface atoms produces different signals including: secondary electrons, back-scattered electrons and X-ray fluorescence (chemical analysis). Since the electron beam is very narrow (focused to a spot about 0.4 nm to 5 nm in diameter), this technique allows nanometre resolution. In this work, FEG-SEM images were obtained on a Zeiss Ultra 55 microscope designed to maximize the imaging resolution at low beam energies. The Ultra 55 is equipped with a SE detector inside the lens (in lens detector) and a BSE detector. Both were engineered to image the electrocatalysts at low accelerating voltage (less than 20 kV).

## B. Chemical techniques

### 1. X-ray Photoelectron Spectroscopy (XPS)

XPS is a spectroscopic technique that is commonly used to determine the elemental composition, the chemical state and the electronic state of the elements contained in the near-surface region of a material. XPS spectra are obtained by analysis of the kinetic energy and number of electrons escaping from the 1-10 nm of the surface region of a sample after irradiating by a X-ray beam. XPS patterns were obtained on a

XR3E2 spectrometer (Vacuum Generator) equipped a Mg $K_\alpha$ (1253.6 eV) X-ray source powered at 300 W (15 kV – 20 mA). The kinetic energies of photoelectrons were measured using a hemispherical electron analyser working in the constant pass energy mode (30.0 eV). The background pressure in the analysis chamber was kept below $10^{-9}$ - $10^{-10}$ mbar during data acquisition. The XPS data signals were taken in increments of 0.1 eV with dwelling times of 50 ms. Analyses were carried out at an angle of 90° between the sample surface and the analyser. High resolution spectra envelopes were obtained by curve fitting of synthetic peak components using the software "Avantage" from ThermoSCientific. The raw data were used with no preliminary smoothing. Symmetric Gaussian–Lorentzian (90:10) product functions were used to approximate the line shapes of the fitting components with Shirley background corrections. The full width at half maximum was fixed at $1.7 \pm 0.1$ eV. Atomic ratios were computed from experimental intensity ratios and normalized by atomic sensitivity factors.

## 2. Raman spectroscopy

The Raman Effect was discovered by the Indian physicist Chandrashekhara Venkata Raman in 1928. The inelastic scattering of light explains the shift in wavelength of a small fraction of radiation scattered by molecules, having different frequency from that of the incident beam. This shift in wavelength is due to the chemical structure of the molecules responsible for scattering. Molecular vibrations active in Raman spectroscopy provide information of the electronic environment symmetry, structure, and bonding of the molecules, and thus allow the quantitative and qualitative analysis of the individual compounds. Raman spectroscopy was used for examining the extent of graphitization of the fresh/aged carbon supports. The Raman spectra were recorded *ex situ* using both a Renishaw RM1000 and a Renishaw In-Via spectrometer. The Raman spectra were obtained by excitation with the radiation from an argon laser ($\lambda$ = 514 nm) operated at approximately 5 mW. The detector was a Peltier-cooled charge coupled device camera and the spectral resolution was about 1 $cm^{-1}$. The measurements were performed with a X50 ULWD objective, and a 100 µm confocal aperture for the sample illumination and collection of the scattered photons.

### 3. *In situ* Fourier Transform Infrared Spectroscopy (*in situ* FTIR)

Fourier transform infrared spectroscopy is a widely used technique. In this study, *in situ* FTIR served to determine the reaction products of the electrochemical carbon oxidation [10]. Coupled EC-FTIR experiments were performed in external reflection mode with a home-made electrochemical cell and *p*-polarized light at $T = 20 \pm 2$ °C. A $CaF_2$ prism, bevelled at 60°, constituted the bottom of the cell. The spectrometer was a Bruker Vertex 80v spectrometer and the detector a liquid $N_2$-cooled mercury-cadmium-telluride. The spectrometer was kept under vacuum during the experiments. The spectral resolution was set to 4 $cm^{-1}$ and 256 interferograms were co-added and then Fourier transformed to obtain a single-beam spectrum (acquisition of one single beam spectrum takes *ca.* 60 s). Data were plotted using relative reflectivity $\frac{R_E}{R_{ref}}$ where $R_E$ is the reflectivity measured at the desired potential and $R_{ref}$ the reflectivity measured at $E = 0.1$ V *vs.* RHE.

## C. Cyclic voltammetry

Cyclic voltammetry is the most-popular technique in electrochemistry [11]. In linear sweep voltammetry and cyclic voltammetry, a periodic potential change is imposed between the working electrode and the counter electrode, and a current is measured between the working electrode and the counter-electrode. The potential at the working electrode is monitored and controlled very precisely with respect to the reference electrode via a potentiostat. The measured current $I$ is the sum of two distinct terms: $I_{fa}$ and $I_{C,}$ where $I_{fa}$ stands for the faradic current by transfer of electrons during the electrochemical reactions taking place at the working electrode (faradic current), and $I_C$ for the capacitive current, which results from the movement of charged species in the electrolyte under polarization conditions. Cyclic voltammetry is the technique of choice to probe surface specific process such as the adsorption / desorption of protons ($H^+$) or oxygen (OH / O) in a PEMFC, determine the electrochemically active surface area or determine the electrocatalytic activity (per unit surface area of Pt) of different electrodes for a given reaction. The potential sweep rate $v_b = \frac{dE}{dt}$ may range between millivolts or several volts per second.

# III. Preparation of the samples/solutions

## A. Solutions

All the glassware used in this work was cleaned by immersion in a $H_2SO_4 : H_2O_2$ mixture overnight and thoroughly rinsed with MQ-grade water. Solutions were prepared from ultrapure water (MQ grade, 18.2 MΩ cm, 1 - 3 ppm TOC) and $HClO_4$ (Suprapur, Merck). The electrolyte was a 0.1 M $HClO_4$ solution purged with argon (99.99 %).

## B. Electrochemical cell set-up

The working electrode was a thin film rotating disk electrode (RDE) composed of supported Pt nanoparticles or nanowires deposited on a glassy carbon disk (Sigradur, 0.196 $cm^2$) and immersed in the electrochemical cell at controlled potential: $E$ = 0.10 V *vs*. the reversible hydrogen electrode (RHE). The counter-electrode was a Pt foil, and the reference electrode - a mercury sulphate electrode (MSE) $Hg|Hg_2SO_4$, $K_2SO_4$ (saturated) connected to the cell via a Luggin capillary.

## C. Ink preparation and ageing

Catalyst inks composed of 5.0 mg of electrocatalyst, 2.4 ml of MQ-grade water and 54 µL of 5 wt. % Nafion® solution (Electrochem. Inc.) were prepared in glass flasks and ultrasonically treated for 30 minutes to obtain homogenous dispersions. The inks were used directly after their preparation or stored for different durations. The caps of the glass flasks were permeable to air, which is believed to cause a mixed electrode potential located between the two reversible potentials of carbon support corrosion (anode) and oxygen reduction on Pt (cathode). The aged catalysts inks were characterized by electrochemical, chemical and physical characterizations after constant interval durations ranging from 1.5 years to 3.5 years. Prior their use in electrochemical experiments, an aliquot of the ink was deposited onto a glassy carbon (or a gold disk in EC-FTIR experiments) and sintered for 5 minutes at $T$ = 110 °C to ensure its binding to the disk and evaporation of the Nafion® solvents.

# IV. Hydrodynamic methods

## A. Study of the oxygen reduction reaction on a rotating disk electrode (ORR, RDE)

Electrochemical measurements were carried out in hydrodynamic conditions on porous rotating disk electrodes composed of Pt/C nanoparticles. The total measured current, $j$, measured on the electrode in the presence of $O_2$ at $E < 1$ V *vs*. RHE is given by the Koutecky-Levich equation: [11] [12]

$$\frac{1}{|\mathrm{j}|} = \frac{1}{|\mathrm{j}_{\mathrm{L}}^{\mathrm{diff.}}|} + \frac{1}{\mathrm{j}_{\mathrm{K}}}$$ Equation II-7

with

$$\frac{1}{|\mathrm{j}_{\mathrm{L}}^{\mathrm{diff.}}|} = \frac{1}{|\mathrm{j}_{\mathrm{L}}^{\mathrm{diff.,\,solution}}|} + \frac{1}{|\mathrm{j}_{\mathrm{L}}^{\mathrm{diff.,\,CL}}|}$$ Equation II-8

Where $j_K$ is the kinetic current density, $I_L^{\text{diff, solution}}$ and $I_L^{\text{diff. CL}}$ are the $O_2$ diffusion limited current density in the liquid electrolyte and in the catalytic layer, respectively. For RDE experiments, $j_L^{\text{diff, solution}}$ is then expressed from the classical Levich equation [11] [12]:

$$| j_L^{\text{diff., solution}} | = 0.62 \text{ n F } C_{O_2} D_{O_2}^{2/3} \upsilon^{-1/6} \omega^{1/2}$$ Equation II-9

Where $n$ is the number of electrons exchanged during the reaction, $F$ is the Faraday constant, $C_{O_2}$ is the oxygen solubility (in mol $m^{-3}$) and $D_{O2}$ is the oxygen diffusion coefficient in the bulk of the electrolyte (in $m^2$ $s^{-1}$), respectively, $\upsilon$ is the kinematic viscosity of the electrolyte (in $m^2$ $s^{-1}$), and $\omega$ is the angular rotation velocity (in rad $s^{-1}$).

After correction of $O_2$ diffusion in solution, the correction of $O_2$ diffusion in the catalytic layer can be processed by using the macro-homogeneous (or continuous) model, as depicted in: [12]

$$j_k = (nFD_{O2}C_{O2} / L) [U_L j_{k,calc}]^{1/2} \tanh\{[U_L j_{k,calc}]^{1/2}\}$$ Equation II-10

where $j_k$ (A) is the experimental geometric current given as a function of the electrode potential from Equation III-7, $j_{k,calc}$ (A $m^{-2}$ geometric) is the true kinetic current density corrected from the oxygen diffusion in the solution and in the active layer, $U_L = L / (nFD_{O2}C_{02})$, and $L$ (m) is the catalytic layer depth.

## B. Study of the oxygen reduction reaction on a rotating ring disk electrodes (ORR, RRDE)

RRDE experiments were performed to determine the number of exchanged electrons in the ORR by quantifying the amount of dihydrogen peroxide produced at the disc. The ORR takes place on the central disc electrode and the produced $H_2O_2$ molecules are either oxidized or reduced on the concentric ring electrode, depending on the potential of this electrode [13]. The disc and ring currents ($I_D$ and $I_R$, respectively) are recorded as a function of the disc electrode potential. A glassy carbon disc-bulk platinum ring Pine Instrument electrode (AFE6M) was used as a working electrode, and the rotation rate was controlled by a Pine Instrument system (MSR Rotators). The geometric characteristics of the RRDE allowed calculation of the theoretical collection efficiency (disc radius 2.50 mm, ring inner radius 2.76 mm, ring outer radius 3.58 mm).

The ring/disc current ratio allowed calculation of the experimental collection efficiency value ($[Fe(CN)_6]^{4-}/[Fe(CN)_6]^{3-}$ was used as a standard redox couple). In this study, the real collection efficiency was calculated for each catalyst layer thickness.

$$I_{2e^-} = I_R / N \qquad \text{Equation II-11}$$

$$I_\mathrm{D} = I_{2\mathrm{e}^-} + I_{4\mathrm{e}^-} \qquad \text{Equation II-12}$$

$$\frac{I_\mathrm{D}}{n_{\mathrm{e}^-}} = \frac{I_{2\mathrm{e}^-}}{2} + \frac{I_{4\mathrm{e}^-}}{4} \qquad \text{Equation II-13}$$

Where $I_\mathrm{D}$ is a disc current, $I_\mathrm{R}$ is a ring current, and $N$ is the collection efficiency. The values of the latter were obtained separately for each sample. The number of exchanged electrons is then function of the ring and disk currents with:

$$n_{\mathrm{e}^-} = \frac{4I_\mathrm{D}}{I_\mathrm{D} + I_\mathrm{R}/N} \qquad \text{Equation II-14}$$

The typical values of $n_{e^-}$ is between 2 and 4 corresponding to two extreme cases, a value of 4 means that all the reacting $O_2$ molecules are reduced into water, whereas $n_{e^-}$= 2 means that the reduction of $O_2$ molecule proceeds only to $H_2O_2$, which escapes from the catalyst layer without being reduced. In the first case, the hydrogen peroxide molar ratio $X_{H2O2}$ is 0, in the second case $X_{H2O2}$ = 1. As can be seen, the $n_{e^-}$ value measured in this work is close to 4, and the $X_{H2O2}$ value is below 0.06. This means that the reduction of $O_2$ molecules proceeds not directly to $H_2O$ but also produces $H_2O_2$ molecules, which can escape from the catalyst layer and be oxidized on the ring or be re-adsorbed on a neighbouring catalytic site and be further reduced in the catalytic layer. Therefore, the real value of $X_{H2O2}$ should be larger than that determined by RRDE.

# V. Accelerated aging tests (AATs)

## 1. Sequential CO stripping experiments

The electrochemical characterization of the Pt/C catalysts was conducted in a four-electrode cell thermostated at *T* = 20 °C. The real surface area of the fresh/aged Pt/C electrocatalyst was determined using CO stripping voltammograms at $v$ = 20 mV $s^{-1}$, assuming that the electrooxidation of a CO monolayer requires 420 µC per $cm^2$. The CO saturation coverage was established by bubbling CO for 6 minutes and purging with Ar for 39 minutes, while keeping the electrode potential at *E* = 0.1 V *vs*. RHE. In this work, we performed sequential CO stripping measurements to probe the stability of the Pt/C catalysts under oxidizing, neutral or reducing atmosphere.

### a) Pseudo CO stripping experiments

It was of interest to determine whether the morphological changes of the Pt/C nanoparticles are caused by the potential program (potential hold at *E* = 0.1 V *vs.* RHE, *i.e.* a reducing potential, during 45 minutes) or by the presence of CO in solution. For that purpose, a sequence of 8 “pseudo CO stripping” voltammograms (consisting of all the steps involved in CO-stripping but using Ar instead of CO) was applied on Pt/C 40 wt. %, and only two “real” CO stripping characterizations were performed at the beginning and at the end of the experiment.

## 2. Accelerated aging tests in solution containing oxidizing, reducing or inert molecules

After electrochemical characterization, the porous RDE was emerged at *E* = 0.1 V *vs*. RHE, transferred into the “durability test cell” and contacted at *E* = 0.1 V *vs*. RHE with the same supporting electrolyte saturated with $H_2$, CO or methanol. The durability test was performed in two parts, the first one consists of 50 potential cycles between 0.05 and 0.4 or 1.23 V *vs*. RHE at $v$ = 0.20 V $s^{-1}$. The electrode was then emerged at *E* = 0.1 V *vs*. RHE, thoroughly rinsed with water and transferred back into the “characterization cell”. After electrochemical characterization, the next 750 cycles were conducted following a similar procedure.

# CHAPTER III

# EVIDENCES OF THE MIGRATION OF PT CRYSTALLITES ON HIGH SURFACE AREA CARBON SUPPORTS IN THE PRESENCE OF REDUCING MOLECULES

This chapter is based on the following article:

“Evidences of the migration of Pt crystallites on high surface area carbon supports in the presence of reducing molecules” by Z. Zhao, L. Dubau, F. Maillard, J. Power Sources, 217 (2012) 449-458.

The contribution of the author of the present thesis includes: the entirety of the experimental part (preparation and measurements of the properties of the catalytic layers), treatment and analysis of the experimental data and participation in preparation of the manuscript for the publication.

# I. Introduction

Conventional catalytic layers of proton-exchange membrane fuel cells (PEMFC) utilise Pt-based catalysts supported on a porous carbon support such as carbon blacks. Carbon blacks possess large surface area, high electron conductance, chemical inertness, adequate porosity and low cost, which make them attractive for this application [1, 2]. Yet, providing long-term stability to the nanometre-sized catalytic materials under PEMFC operating conditions has proven challenging. Degradations mechanisms of carbon-supported Pt-based nanoparticles include: (i) 3D Ostwald ripening, where the smaller crystallites dissolve preferentially, yielding the formation of $Pt^{z+}$ and $M^{y+}$ ions (M being the alloying element) and their redeposition onto larger crystals [3, 4]; (ii) the chemical reduction of the $Pt^{z+}$ ions in ion conductors, yielding formation of electrically disconnected Pt crystallites [5]; (iii) the corrosion of the carbon support leading to the detachment of the metal nanoparticles [6] and (iv) the migration of the Pt-based crystallites [7-10]. The interest reader is referred to Chapter I for more details.

Although there is a large body of experimental evidences for the first three mechanisms, the migration of crystallites has only been seldom explored. There are several reasons for this, the most obvious being that crystallite migration, carbon corrosion, and Ostwald ripening are occurring simultaneously during the ageing of Pt-M/C materials [5, 11]. Indeed, the corrosion of the carbon support to gaseous species induces the movement of the metal crystallites and their further agglomeration/detachment [12]. Similarly, the preferential dissolution of the smallest crystallites during Ostwald ripening is likely to influence their mobility on the carbon support. Another reason is that crystallite migration, carbon corrosion, and Ostwald ripening may produce similar morphological changes such as the aggregation/coalescence of the metal nanoparticles [5, 12]. Several studies tried to make a distinction between a sintering caused by Ostwald ripening or by crystallite migration on the basis of the shape of the particle size distribution (PSD) [13]. However, such analysis is strongly dependent on the quality, the choice and the proper analysis of representative transmission electron microscopy images and, practically speaking, remains hardly feasible.

Dealing with crystallite migration also raises the nature of the interactions existing between the metal nanoparticles and the underlying carbon support. There is a consensus in the scientific community to say that carbon surface oxides (referred to as $CO_{surf}$ in the manuscript) play a major role during the synthesis of metal nanoparticles [14-23]. Lowde *et al.* [15] and Prado-Burguette *et al*. [16] argued that the aqueous metal ion species strongly interact with oxygenated groups present on the carbon support through electrostatic interactions, and determine the structure and the morphology of the final metal phase (*e.g.* particle size distribution and degree of agglomeration). On the contrary, other authors reported a decrease of the metal dispersion in the presence of oxygen-bearing surface groups [14, 21]. Now, the persistence of these interactions after the reduction of the metallic salt to form a metal nanoparticle remains a still open question. There are experimental evidences, from electron-spin resonance, [24] X-ray photoelectron spectroscopy [17, 25-29] and infrared spectroscopy studies, [30, 31] that metal nanoparticles interact with the carbon support via the oxygen atoms of the $CO_{surf}$ groups. This interaction not only influences the catalytic activity of PEMFC reactions [2] but also the resistance to sintering of the metal particles in both the gas [19, 32] and the liquid phase [33]. On the other hand, $CO_{surf}$ groups are easily generated on high surface area carbon supports in PEMFC operating conditions (low pH < 1, high temperature > 70 °C, positive electrode potentials and oxygen-containing environment at the cathode) [34-36]. In an early study, Giordano *et al.* [37] reported that the presence of $CO_{surf}$ groups on the carbon support enhances the carbon corrosion rate, which was rationalized by the transfer of oxygenated species from the Pt nanoparticles to the $CO_{surf}$ species, to form gaseous products such as CO and $CO_2$ [12, 35, 38-40]. Summing up, $CO_{surf}$ groups play a dual role: (i) they behave as anchoring sites for the metal nanoparticles; (ii) they are reaction intermediates in the corrosion of the carbon support. However, their interaction with the metal nanoparticles is still not fully understood and is the focus of the present study.

To reach this objective, commercial Pt/Vulcan XC 72 electrocatalysts (denoted Pt/C in what follows) were aged in “mild” conditions, for which the corrosion of both the Pt nanoparticles and the carbon support cannot be considered dominant. Transmission electron microscopy and electrochemical techniques were successfully employed to characterize the fresh and the aged catalysts. We show that the migration of Pt crystallites is accelerated in the presence of “reducing” molecules such as $H_2$, CO, and $CH_3OH$.

# II. Results and discussion

## A. Definition of structural markers of “crystallite migration”

During PEMFC operation, crystallites may collide, form agglomerates and eventually coalesce to form larger crystallites. Consequently, the ratio of the fraction of “isolated” particles (*e.g.* spherically-shaped and non-agglomerated) to the fraction of agglomerated particles decreases. Those changes can be imaged in TEM and quantified by a proper analysis of representative images as it has been described in Chapter II. Moreover, “CO stripping” voltammograms were used as a rapid and facile method to detect *in situ* the agglomeration of the carbon-supported Pt particles. Indeed, it is well-established that the presence of nanoparticles featuring a high concentration of surface defects, such as Pt agglomerates, yields a CO electrooxidation pre-peak, which is shifted *ca.* 50 mV negative versus the CO electrooxidation peak on isolated Pt/C particles [41-45]. Additionally, the position of the main CO stripping peak strongly depends on the mean particle size and shifts toward positive potential with a decrease of the Pt particle size (the reader is referred to [41, 42, 46] for more details).

The relevance of the chosen structural markers is demonstrated in Figure III-1, showing background subtracted CO stripping voltammograms on Pt/C catalysts with different Pt wt. %, and the associated particle size distributions. As the Pt wt. % increases, the charge under the pre-peak develops, reflecting an increased fraction of agglomerated Pt nanoparticles in the sample. The later agrees with what was observed in TEM images (Table III-1). The increased agglomeration degree can be accounted for by considering that, as the metal loading increases, the carbon support cannot accommodate the Pt nanoparticles, and their agglomeration becomes more facile. This agrees with theoretical calculations of Ruckenstein *et al.* [10].

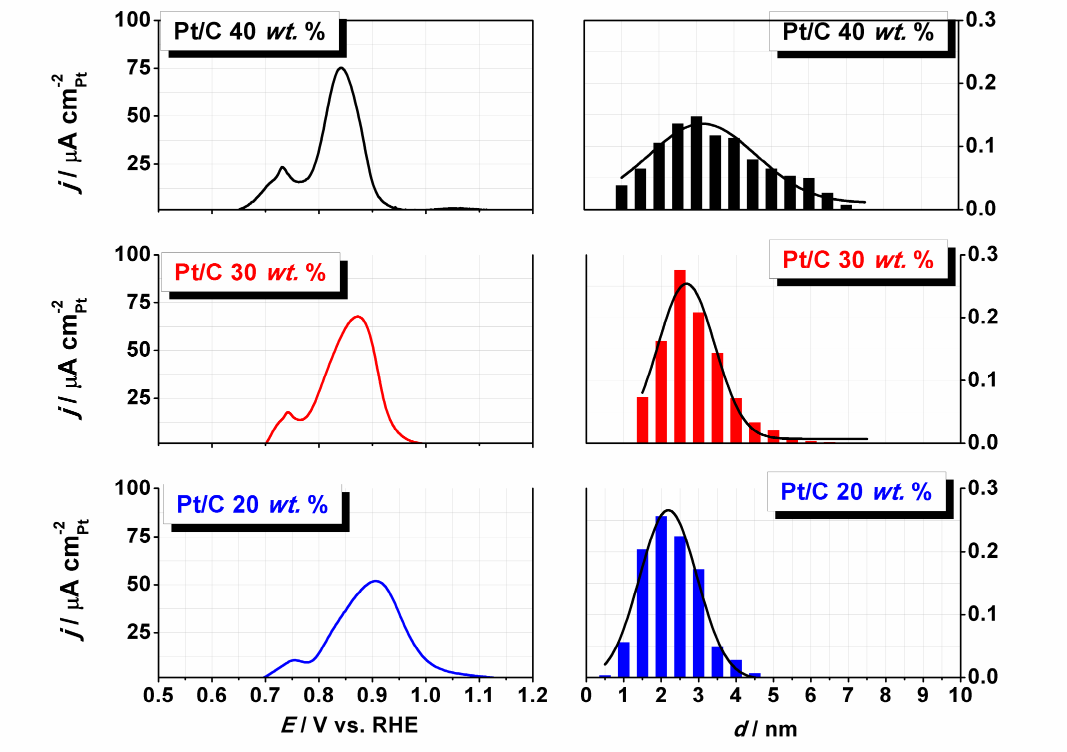

Figure III-1. Averaged background-subtracted CO stripping voltammograms and particle size distributions of the Pt/C electrocatalysts used in this study. The currents are normalized to the real surface area estimated from CO stripping coulometry. Each voltammogram is the average of three measurements. Electrolyte: 0.1 M $HClO_4$; $v$ = 0.020 V $s^{-1}$; $T$ = 20 °C.

At this point of the chapter, we would like to point out that caution should be exercised when considering the number of isolated/agglomerated particles listed in Table III-1. Indeed, our statistical analysis only considered the number and not the size/shape of the Pt aggregates. Therefore, the relationship with the electrochemical measurements remains to a large extent qualitative but is good enough to draw clear and concise conclusions on the fraction of aggregated particles present in the sample. In particular, the above results, as well as those obtained by different research groups [41, 42, 44-47], demonstrate a strong relationship between the amplitude of the pre-peak at low electrode potentials in CO stripping voltammograms and the extent of particle agglomeration.

Table III-1. Number and surface averaged mean particle size, density of isolated and agglomerated particles and loss of isolated Pt particles for three Pt/C commercial electrocatalysts before/after repetitive CO stripping voltammograms.

| | 20 wt. % Pt/C | | 30 wt. % Pt/C | | 40 wt. % Pt/C | | |
|---|---|---|---|---|---|---|---|
| | Fresh | After 10 CO stripping voltammograms | Fresh | After 10 CO stripping voltammograms | Fresh | After 10 CO stripping voltammograms | After 8 pseudo CO stripping voltammograms |
| $\bar{d}_N$ / nm | 2.5 | 2.5 | 2.7 | 2.9 | 3.5 | 4.6 | 3.6 |
| $\bar{d}_S$ / nm | 2.9 | 2.9 | 3.4 | 3.4 | 4.5 | 5.3 | 4.5 |
| Number of isolated particles / $\mu m^{-2}$ carbon | 38000 | 32000 | 10800 | 8000 | 8000 | 5600 | 7500 |
| Number of agglomerated particles / $\mu m^{-2}$ carbon | 2500 | 2500 | 2800 | 3000 | 2600 | 2200 | 2200 |
| Total number of particles / $\mu m^{-2}$ carbon | 40500 | 34500 | 13600 | 11000 | 10600 | 7800 | 9700 |
| Fraction of agglomerated particles / % | 6.2 | 7.2 | 20.6 | 27.3 | 24.5 | 28.2 | 22.7 |
| Loss of isolated particles / % | 0 | 15.8 | 0 | 26.0 | 0 | 30.0 | 6.2 |

## B. Mobility of Pt crystallites under CO environment

Figure III-2 shows the effect of repetitive CO stripping voltammograms for the different catalysts used in this study. Over the sequence, the CO stripping voltammograms feature a decrease in the charge under the main CO electrooxidation peak at the expense of the charge contained under the CO electrooxidation pre-peak. Considering the above discussion, these results indicate that the Pt nanoparticles are mobile on the high surface area carbon support and collide upon agglomeration during the CO stripping sequences. The validity of this assumption is confirmed by the analysis of representative TEM images, which shows that the number of isolated particles is reduced in favour of the number agglomerated and/or non-spherical Pt/C nanoparticles, and that this effect strongly depends on the Pt wt. %.

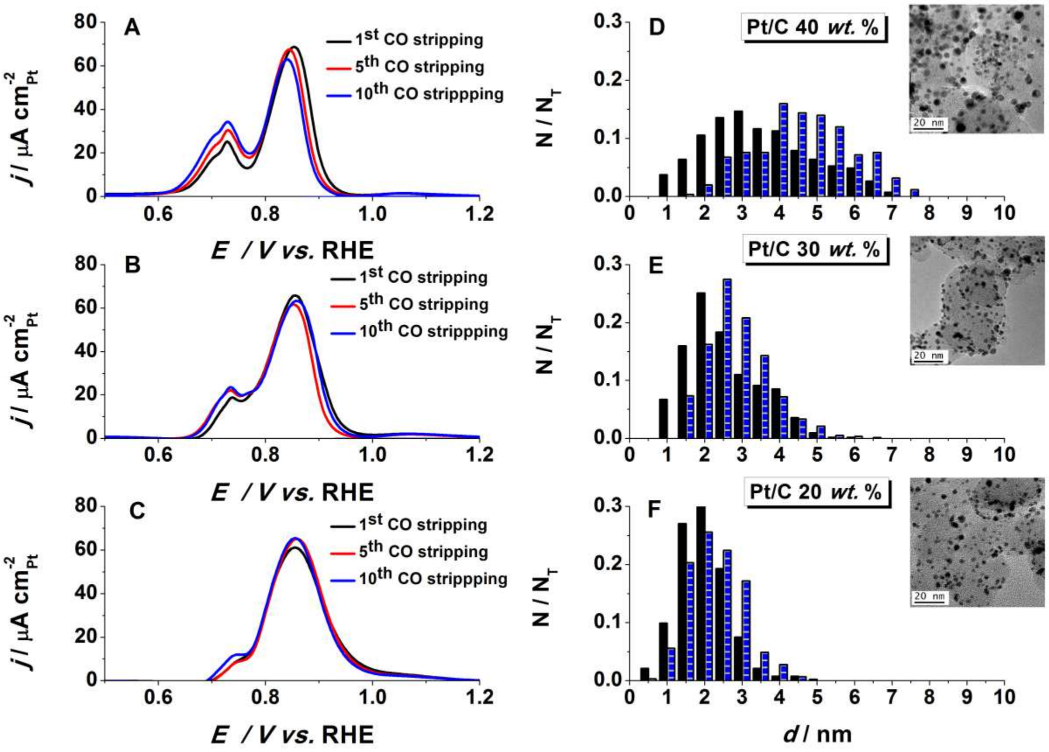

Figure III-2. (A-C) Repetitive background-subtracted CO stripping voltammograms on Pt/C electrocatalysts and (D-F) representative TEM images and the size distributions of the "isolated" particles after the durability test. The currents are normalized to the real surface area estimated from CO stripping coulometry. Each voltammogram is the average of three measurements. Electrolyte: 0.1 M $HClO_4$; $v = 0.020$ V $s^{-1}$; $T = 20$ °C.

Figure III-3 shows the initial and the final CO stripping voltammograms recorded on Pt/C 40 wt. % (A) in the presence and (B) in the absence of CO in solution during a 10 CO-stripping or pseudo-stripping sequence (see Experimental section, V-1). On the right hand side of Figure III-3 are also shown representative TEM images as well as the associated particle size distributions.

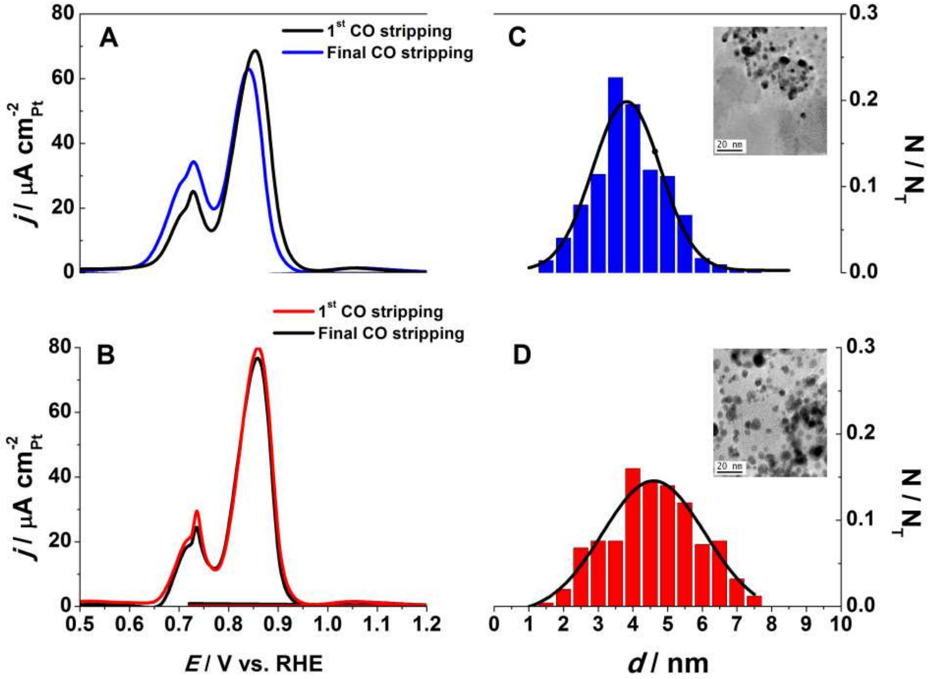

Figure III-3. Initial and final background-subtracted (A) CO stripping or (B) pseudo CO stripping voltammograms recorded on Pt/C 40 wt. %. (C) and (D) show representative TEM images of the catalyst and the size distributions of the "isolated" particles after each sequence. Electrolyte: 0.1 M $HClO_4$; $v = 0.020$ V $s^{-1}$; $T = 20$ °C.

It is clear from Figure III-3B that the potential program causes slight morphological changes, and is not responsible for the agglomeration of the Pt nanoparticles. Indeed, the fraction of isolated and agglomerated particles and the shape of the particle size distribution are very similar before and after this sequence (Table III-

1). At variance, when performed in the presence of CO in solution, the sequence of 10 CO stripping voltammograms (8 + 2 for characterization) promotes the development of the CO electrooxidation pre-peak, associated with the presence of Pt agglomerates in the sample. In the presence of CO in solution, TEM images revealed considerable loss of “isolated” Pt particles due to the formation of Pt agglomerates.

## C. Effect of $H_2$, CO and $CH_3OH$

Knowing such information, we now investigate the effect of two other molecules (hydrogen and methanol) on the morphology of the Pt/C nanoparticles. Experiments were also conducted in the presence of CO in solution during potential cycling (so-called “bulk CO” oxidation). Figure III-4 shows the CO stripping voltammograms recorded on the fresh Pt/C 40 wt. % before and after 50 or 800 CVs in $H_2$ or in CO-saturated solutions or a solution containing 0.5 M methanol. CO stripping and potential cycling were conducted in different electrochemical cells, referred to as “characterization cell” and “durability test cell” cells. The transfer procedure included electrode emersion at $E$ = 0.1 V *vs.* RHE, rinsing in MQ-grade water and transfer to the other cell. The overall procedure takes less than 1 minute. For sake of comparison, a “blank” experiment was also performed under argon *i.e.* in the absence of a reducing molecule in solution. Table III-2 shows that the “blank” experiment causes minor morphological changes in the sample, with a slight decrease of the fraction of isolated particles but no increase of the fraction of agglomerated particles. The rationale for such observation is believed to be the detachment of some Pt nanoparticles from the carbon support during potential cycling sequences as it has already been observed during accelerated durability tests [50]. Furthermore, the particle size distribution suffered slight changes, which confirms that the observed morphological changes shall be ascribed only to the migration of Pt crystallites (see the particle size distributions in Figure III-4). In CO stripping voltammograms, a slight decrease of the charge under the main CO electrooxidation peak is observed at the benefit of the pre-peak.

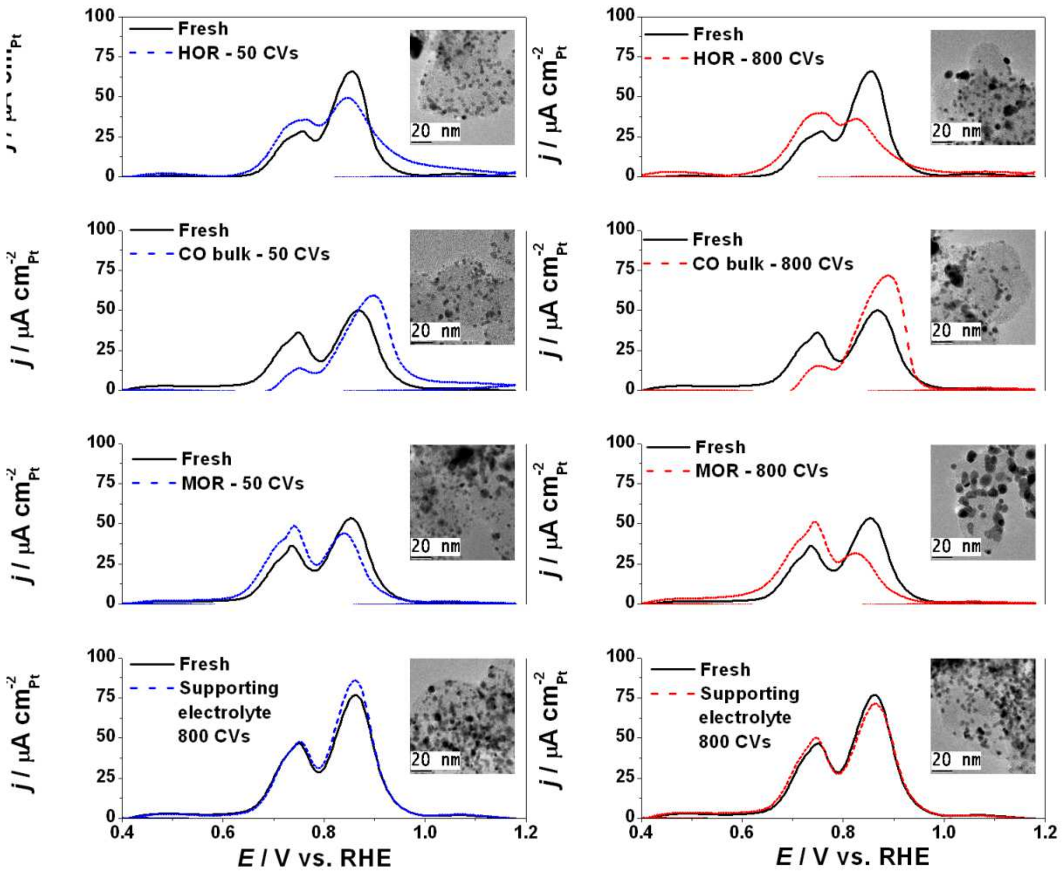

Figure III-4. Background-subtracted CO stripping voltammograms on Pt/C 40 wt. % before/after 50 cycles or 800 cycles between 0.05 and 1.23 V *vs.* RHE in solutions containing hydrogen, carbon monoxide or methanol. The insets show representative TEM images of the catalyst after 50 or 800 CVs. Electrolyte: 0.1 M $HClO_4$; $v$ = 0.020 V $s^{-1}$; $T$ = 20 °C.

At variance, the morphological changes are considerable when $H_2$, CO or methanol is present in solution during potential cycling. In this case, the charge under the CO electrooxidation pre-peak continuously increases at the expense of the main peak. Representative TEM images of the aged Pt/C catalysts shown in Figure III-4 feature the formation of localized areas of very high Pt loading on Vulcan XC72, while other zones of the carbon support are almost depleted in Pt. The analysis of these images confirms that the fraction of agglomerated particles greatly increases during potential cycling in the presence of $H_2$, CO or methanol (Table III-2 and Figure III-5). The migration rate of Pt crystallites is the largest in CO-containing solution and decreases in the order CO > $CH_3OH$ > $H_2$ (Table III-2). To the best of our knowledge, this is the first evidence of Pt crystallite migration in liquid electrolyte in the absence of other coarsening mechanisms such as Ostwald ripening or carbon corrosion.

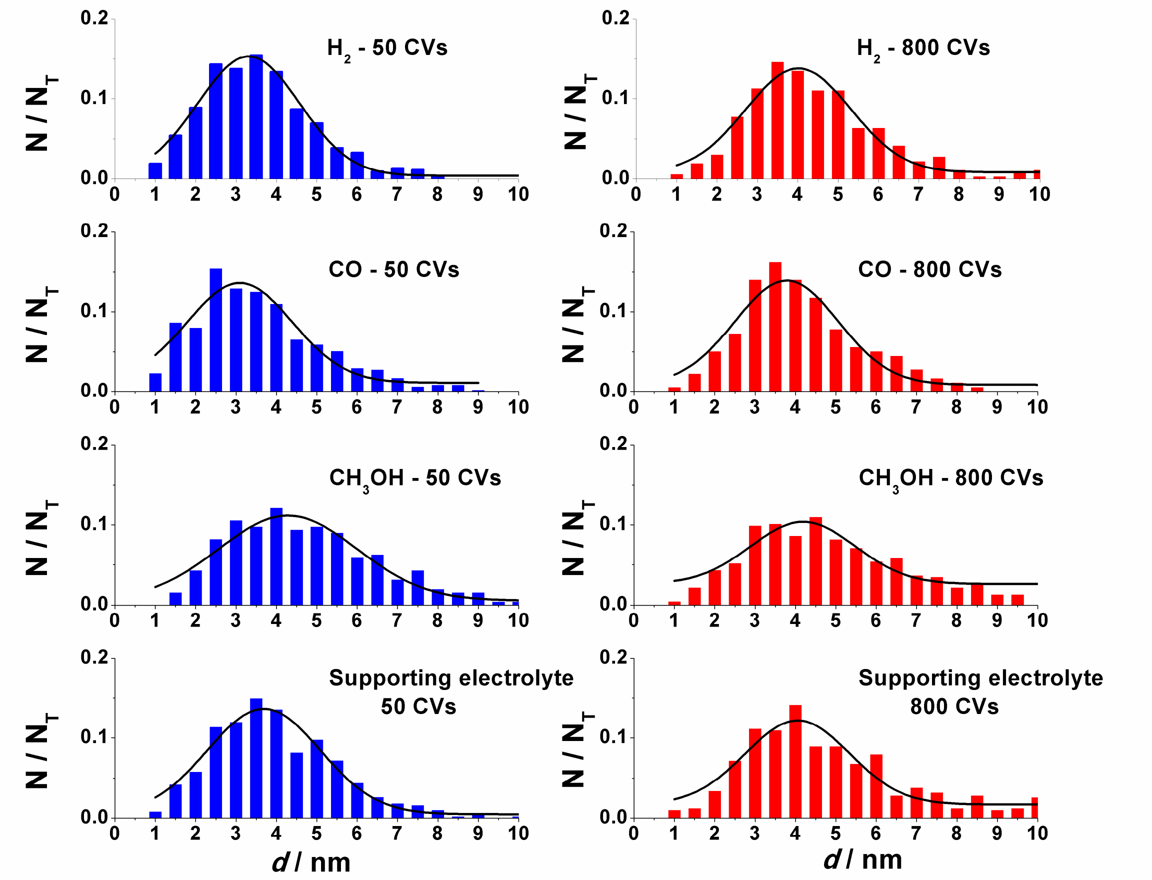

Figure III-5. Particle size distribution of Pt/C catalysts after 50 cycles (left) and 800 cycles (right) between 0.05 and 1.23 V *vs.* RHE in electrolyte containing hydrogen, carbon monoxide, methanol or argon. Electrolyte: 0.1 M $HClO_4$; $v = 0.020$ V $s^{-1}$; $T = 20$ °C.

We now discuss "bulk CO" experiments where CO is continuously present in solution. In this case, the analysis of representative TEM images shows that the presence of CO in solution accelerates the formation of Pt agglomerates. The CO stripping voltammograms feature: (i) a decreased charge under the CO electrooxidation pre-peak, and (ii) a shift towards positive electrode potentials of both the onset and the position of the main CO electrooxidation peak. These opposite results can be reconciliated by considering that "surface defects", which are the source of oxygen-containing species necessary to oxidize CO, are removed by potential cycling in CO-containing solution [51-53]. Consequently, the Pt/C nanoparticles possess lower concentration of surface defects after potential sweeping in CO-containing solution, and hence decreased reactivity for the $CO_{ads}$ stripping reaction, which explains the shift towards more positive potential of the $CO_{ads}$ electrooxidation pre-peak and the decreased charge under this peak.

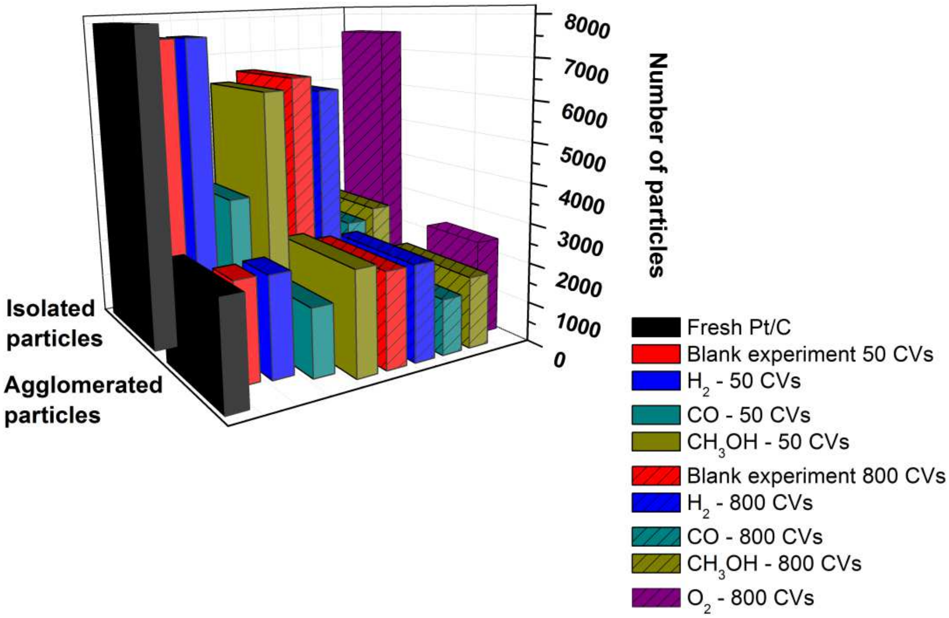

Figure III-6. The fraction of isolated and agglomerated particles before/after potential cycling in solutions containing argon, hydrogen, carbon monoxide or methanol.

Table III-2. Number and surface averaged mean particle size, density of isolated and agglomerated particles and loss of isolated Pt particles for a Pt/C 40 wt. % commercial electrocatalyst before/after potential cycling in various conditions. HPL stands for high upper potential limit (0.05 < *E* < 1.23 V *vs.* RHE).

| Pt/C 40 wt. % E-TeK | Fresh | Supporting electrolyte 50 CVs - HPL | HOR 50 CVs - HPL | MOR 50 CVs - HPL | COOR 50 CVs - HPL | Supporting electrolyte 800 CVs - HPL | HOR 800 CVs - HPL | MOR 800 CVs - HPL | COOR 800 CVs - HPL | ORR 800 CVs - HPL |
|---|---|---|---|---|---|---|---|---|---|---|
| $\bar{d}_N$ / nm | 3.5 | 4.0 | 3.5 | 4.5 | 3.7 | 4.6 | 4.4 | 5.1 | 5.0 | 3.3 |
| $\bar{d}_S$ / nm | 4.5 | 5.0 | 4.5 | 5.4 | 3.4 | 6.0 | 5.7 | 7.1 | 5.7 | 4.3 |
| Number of isolated particles / $\mu m^{-2}$ carbon | 8000 | 7600 | 7600 | 6200 | 3400 | 6500 | 6100 | 2700 | 2400 | 7500 |
| Number of agglomerated particles / $\mu m^{-2}$ carbon | 2600 | 2500 | 2500 | 2600 | 1700 | 2400 | 2400 | 1800 | 1400 | 2400 |
| Total number of particles / $\mu m^{-2}$ carbon | 10600 | 10100 | 10100 | 8800 | 5100 | 8900 | 8500 | 4500 | 3800 | 9900 |
| Loss of isolated particles / % | 0 | 5.0 | 5.0 | 22.5 | 57.5 | 18.7 | 23.7 | 66.2 | 70.0 | 6.3 |

Estimating the relative contribution of the Pt crystallite migration to the overall Pt surface area loss with respect to other degradation mechanisms is interesting. In our measurements, care was taken to avoid experimental conditions favouring Ostwald ripening and carbon corrosion. Consequently, the Pt surface area losses are systematically comprised between 0 and 8 %, and are consistent with the evoked migration of Pt crystallites. These percentages are also consistent with high resolution TEM (HRTEM) images showing that Pt crystallites retain their individual crystallographic characteristics in Pt agglomerates. Occasionally, sintered single grain coalesced Pt particles were also observed. Here, it is worth mentioning that the distinction between sintered and aggregated particles is hardly feasible with electron-diffraction spectra.

It is also worth noting that the formation of localized areas with high Pt loading, such as those imaged in this study, may influence other PEMFC catalysts degradation mechanisms. Indeed, the corrosion rate of the HSAC support is accelerated and proceeds heterogeneously in the presence of high Pt wt. %: highly loaded zones of the carbon support suffer more severe corrosion than the neighbouring “Pt-depleted” zones [8, 37]. On the contrary, we point out that the agglomeration of Pt nanoparticles may influence positively the rate of 3D Ostwald ripening. Indeed, according to the Gibbs-Thompson relation, the increase in the mean Pt particle size resulting from the agglomeration of Pt crystallites will cause an increase in their chemical potential, and translate into lower Pt corrosion kinetics [9].

## D. Effect of the upper potential sweeping conditions

We now investigate the effect of the upper potential limit on the migration of the Pt crystallites. Additional experiments were performed with an upper potential limit *E* = 0.40 V *vs.* RHE so as to avoid the exposure of the Pt/C catalysts to the potential region where surface hydroxides form (*E* > 0.60 V *vs.* RHE, see Ref. [54]). Figure III-7 and Table III-3 show that the Pt crystallites remain mobile regardless of the upper potential limit. However, slights changes of the PSD are observed, which confirms that Pt crystallite migration is the only coarsening mechanism at work. Interestingly, a comparison between Table III-2 and Table III-3 shows that the morphological changes of the fresh Pt/C catalyst, although unequivocal, are minored with the decrease of the upper potential limit.

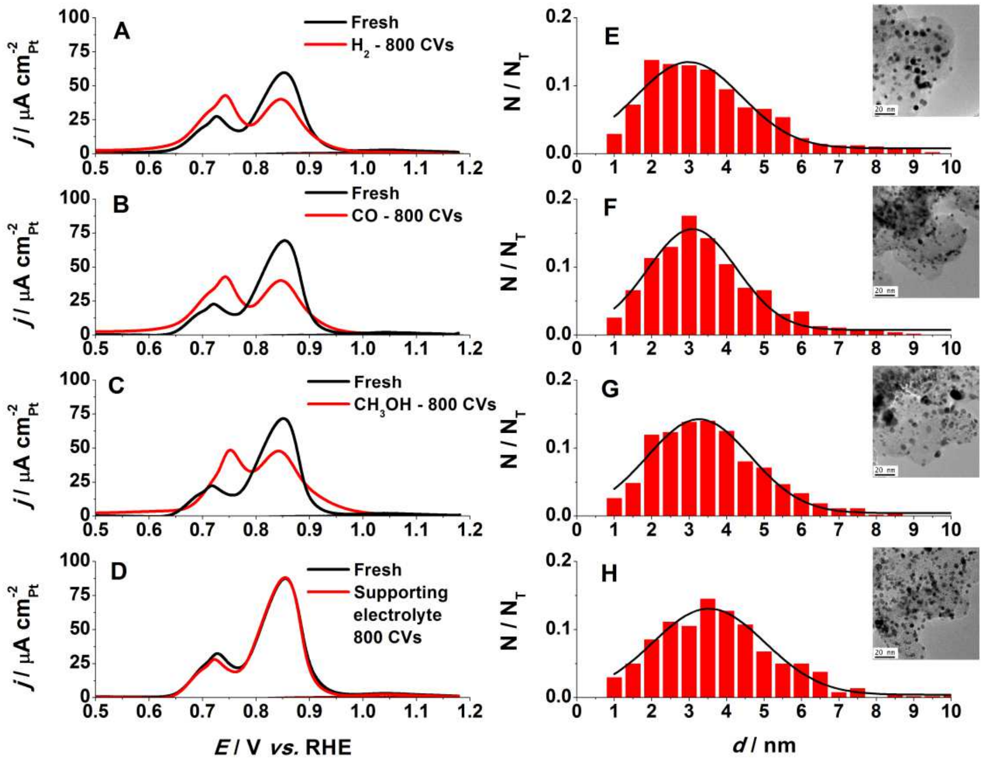

Figure III-7. (A-D) Background-subtracted CO stripping voltammograms and (E-H) particle size distribution of Pt/C catalysts before/after 800 cycles between 0.05 and 0.40 V *vs.* RHE in hydrogen, carbon monoxide or methanol-containing solution. The insets show representative TEM images of the Pt/C catalysts and the size distributions of the "isolated" particles after the 800 cycles. Electrolyte: 0.1 M $HClO_4$; $v$ = 0.020 V $s^{-1}$; $T$ = 20 °C.

Table III-3. Number and surface averaged mean particle size, density of isolated and agglomerated particles and loss of isolated Pt particles for a Pt/C 40 wt. % commercial electrocatalyst before/after potential cycling in various conditions. LPL stands for low potential limits ($0.05 < E < 0.40$ V *vs.* RHE).

| Pt/C 40 wt. % E-TeK | Supporting electrolyte 800 CVs - LPL | HOR 800 CVs - LPL | MOR 800 CVs - LPL | COOR 800 CVs - LPL |
|---|---|---|---|---|
| $\bar{d}_N$ / nm | 3.8 | 3.6 | 5.1 | 3.5 |
| $\bar{d}_S$ / nm | 5.0 | 5.2 | 7.1 | 4.7 |
| Number of isolated particles / µm$^{-2}$ carbon | 6500 | 6400 | 4800 | 5400 |
| Number of agglomerated particles / µm$^{-2}$ carbon | 2400 | 2500 | 2500 | 2300 |
| Total number of particles / µm$^{-2}$ carbon | 8900 | 8900 | 7300 | 7700 |
| Loss of isolated particles / % | 27.0 | 28.0 | 34.2 | 29.9 |

## E. Identical-location TEM (IL-TEM) experiments

IL-TEM experiments were also performed to confirm the increased rate of Pt crystallite agglomeration in the presence of reducing molecules. Similarly to what was done before, 800 potential cycles were performed in two different potential ranges ranging from 0.05 to 0.50 V *vs.* RHE (see Figure III-8) or from 0.05 to 1.23 V *vs.* RHE (see Figure III-9). Minor morphological changes were observed under Ar atmosphere and "low potential limit" conditions, except the detachment of Pt nanoparticles already reported in the literature [5, 48-53]. Under $O_2$ atmosphere, the detachment of particles is more pronounced, which we believed is induced by carbon corrosion. Indeed, at low electrode potential, the oxygen reduction reaction yields formation of hydroperoxyl (HOO•), and hydroxyl (HO•) species [54]. Those radical species possess a standard potential of 2.80 V *vs*. RHE at *T* = 25°C, [55] and are extremely aggressive towards the HSAC leading to Pt nanoparticle detachment. Visual evidences of carbon corrosion are also visible in the TEM images. Under CO atmosphere, the scenario is completely different as expected from the CO stripping measurements presented in the previous section. In this case, crystallite migration is the major degradation mechanism but no sign of coalescence of the Pt nanocrystallites is observed.

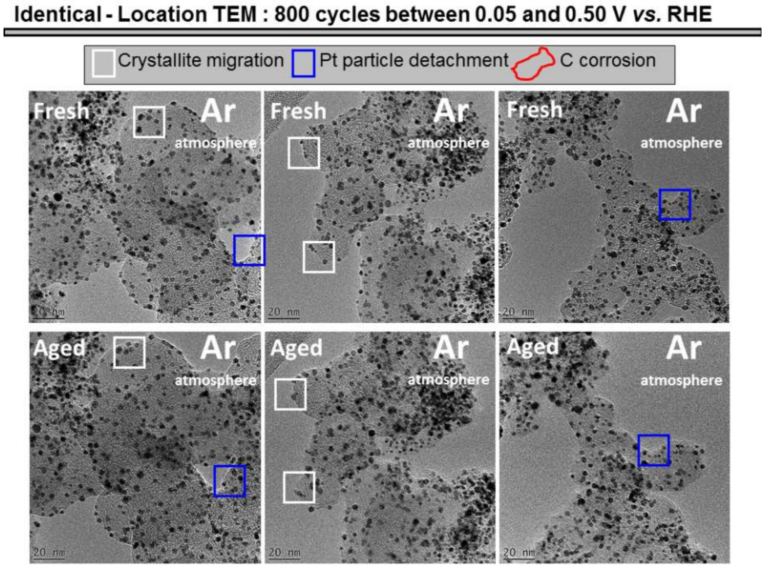

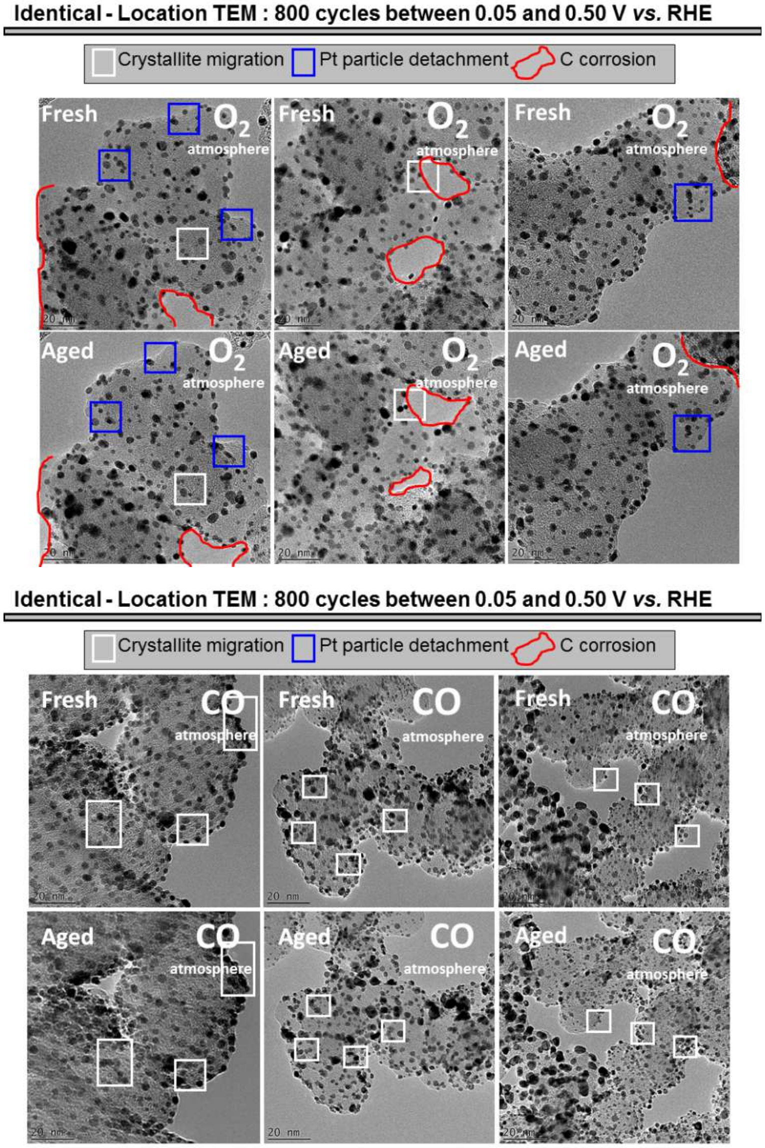

Figure III-8. IL-TEM images of Pt/C catalysts before and after 800 potential cycles between 0.05 and 0.50 V vs. RHE in 0.1 M $HClO_4$ containing Ar, CO or $O_2$. The white squares emphasize crystallite migration and further aggregation, the blue squares point particle detachment and the red lines underline zones where the carbon support was corroded. Electrolyte: 0.1 M $HClO_4$; $v$ = 0.020 V $s^{-1}$; $T$ = 20 °C.

The approach was extended to explore a larger potential window *i.e*. from 0.05 to 1.23 V *vs*. RHE. Representative IL-TEM images of Pt/C catalyst before and after accelerated aging test are shown in Figure III-9. They provide strong evidences that 3D Ostwald ripening is now overlapping with the three degradation mechanisms described above (Pt nanoparticle detachment, Pt crystallite migration/aggregation and carbon corrosion). Indeed, the Pt/C catalysts after the aging procedure feature present features typical of 3D electrochemical Ostwald ripening such as (i) an increase of the mean Pt particle size, (ii) a decrease of the density of isolated particles at the expense of the agglomerated particles. Some particle necking caused by the redeposition of $Pt^{z+}$ ionic species is also observed. Here again, the gas atmosphere plays a key role: Ostwald ripening is predominant and more consequent under Ar atmosphere and its importance decreases in the presence of CO or $O_2$. This interesting phenomenon remains currently unexplained, and will be the subject of future work [53, 56].

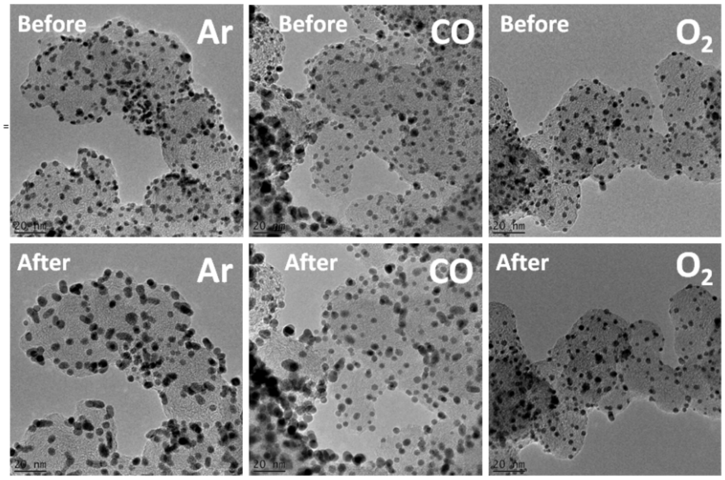

Figure III-9. IL-TEM images of Pt/C catalysts before and after 800 potential cycles between 0.05 and 1.23 V *vs*. RHE in 0.1 M $HClO_4$ containing Ar, CO or $O_2$. Electrolyte: 0.1 M $HClO_4$; $v$ = 0.020 V $s^{-1}$; $T$ = 20 °C.

## F. On the origin of Pt crystallite migration

We now discuss the origin of the increased mobility of Pt nanoparticles in the presence of $H_2$, $CH_3OH$ and CO. We believe that the observed changes can be rationalized in the frame of (i) the changes in the work of adhesion upon chemisorption and (ii) the reduction of the oxygen-bearing surface groups by $H_2$, $CH_3OH$ and CO.

### 1. Changes in the work of adhesion upon chemisorption

The strength of interaction between a metal nanoparticle and the underlying HSAC is commonly described by the adhesion work ($W_a$) [57]:

$$W_a = (\sigma_{s/g} + \sigma_{m/g} - \sigma_{s/m}) A_{s/m} \qquad \text{Equation III-1}$$

Where $\sigma_{s/g}$, $\sigma_{m/g}$ and $\sigma_{s/m}$ are the surface tensions between the support–gas, the metal–gas and the support–metal interface and $A_{s/m}$ is the particle-support contact area. This equation nicely shows that any change of the surface tension of both the metal (such as that arising from chemisorption on the metal surface) and the support strongly impacts the metal–support bonding. Consequently, based on simple thermodynamic considerations, the stability towards sintering must increase in the inverse order of increasing the adsorption heat of adsorbates (decreased metal–gas surface tension ~ decreased work of adhesion ~ higher mobility of the Pt nanocrystallites).

Table III -4. Heats of adsorption of various adsorbates on a Pt(111) surface.

| Adsorbate | Surface | Heat of adsorption / kcal mol$^{-1}$ | Reference |
|---|---|---|---|
| $O_2$ | Pt(111) | - 48.0 | [58] |
| CO | Pt(111) | -29.2 | [58] |
| $H_2$ | Pt(111) | -22.9 | [58] |
| $CH_3OH$ | Pt(111) | -8.0 | [59] |

Table III-4 shows the heats of adsorption of $CH_3OH$, $H_2$, CO and $O_2$ measured at about 10% of a monolayer on Pt(111), *i.e.* at sufficiently low coverage such that adsorbate–adsorbate interactions are negligible. The phenomenon of adsorption is exothermic *i.e.* the heats of adsorption are negative. It is interesting to note that on Pt(111), both CO and hydrogen have substantial chemisorption heats in the range of -29 and -23 kcal mole$^{-1}$, respectively [60, 61]. Consequently, chemisorbed methanol is energetically unstable with respect to adsorbed CO and hydrogen on a Pt surface and easily dissociates to form these molecules [59]. On the basis of the previous equation, it may also be inferred that the stability towards sintering should decrease as $H_2 < CH_3OH < CO < O_2$, in good agreement with the above-mentioned results.

It is also well documented both in gas-phase and liquid catalysis (see Ref. [62, 63]) that the adsorption of molecules may cause a pronounced change of the Pt nanoparticles shape. Adsorption is expected to favour nanoparticles shapes maximizing the enthalpy of adsorption. In a recent study, Cabié *et al.* [62] observed preferentially-oriented Pt nanoparticles with large facets by environmental TEM. While the latter are close to their equilibrium shape under $H_2$ (pressure equivalent to a few millibars), the area of the (001) facets strongly increases upon the adsorption of $O_2$, and drives the reconstruction of the Pt nanoparticles into a square shape. In electrocatalysis, X-ray absorption spectroscopy results of Mukerjee and Mac Breen [64] showed that carbon-supported Pt nanoparticles are close to their equilibrium shape at electrode potential close to 0 V *vs.* RHE (*i.e.* in the presence of adsorbed H atoms) and turn from a cubooctahedral to a plane raft-like particle shape at $E >$ 0.54 V *vs.* RHE (*i.e..* in the presence of adsorbed O atoms*)*. Such morphological changes were also confirmed in the recent *in situ* study of Kikuchi *et al.* with atomic force microscopy [65]. Therefore, the enhanced rate of Pt crystallite migration may also be accounted for by the continuous chemisorption/desorption of reducing molecules on the Pt surface. The alternation between oxidizing ($E >$ 0.60 V vs. RHE) and reducing potentials ($E <$ 0.60 V vs. RHE) during potential sweeping causes perpetual changes in the equilibrium shape of the Pt nanoparticles and hence may accelerate their mobility on the HSAC.

## 2. Trapping of Pt nanoparticles at defects of the graphitic crystallites

We now discuss the nature of the sites of the carbon support, where Pt nanoparticles are sitting on the HSAC support. During the migration phenomenon, the Pt crystallites are believed to move from a carbon site of lowest energy to another equivalent site without very much expenditure of energy and without any memory of their motions. Though the detailed mechanisms are not known, the process requires considerable activation energy, and hence is believed to be negligible at the temperature of this study ($T$ = 20°C). In an early study, Bett *et al*. [10] suggested that the edges of the graphitic basal planes may possibly be the sites at which Pt nanoparticles are trapped. Since the density of the “trap” sites is limited, it is understandable that excessive loading by Pt nanoparticles results in a large fraction of “unstable” Pt nanoparticles (that is “in insufficient interaction with the carbon support”) and in a closer distance between the Pt nanoparticles. Such scenario accounts for the dependence of the rate of Pt crystallite migration on the Pt wt. % observed in Figure III-2 but cannot rationalize the influence of reducing molecules on the process.

## 3. Reduction of oxygen-containing carbon surface groups

As mentioned in the Introduction, a large variety of $CO_{surf}$ groups exists on high surface area carbon supports but the nature of their interactions with the metal phase remains unclear. Based on X-ray absorption spectroscopy, and attenuated total reflection infrared spectroscopy results, Hull *et al.* [29] argued that Pt nanoparticles interact with carbon nanotubes via ester and carboxyl oxygen atoms. Strong interactions between the metal phase and the oxygen-bearing surface groups find also support in the work of Antonucci *et al.* [17]. The authors reported an increase in the $Pt_{4f}$ binding energy with the increase of the concentration of acidic carbon surface oxides. Therefore, it is not surprising that the presence of reducing molecules in solution enhances the rate of Pt crystallite migration. Indeed, these molecules all possess a standard potential close to 0 V *vs.* SHE: (i) $H_2$ ($E^{0}_{H^+/H_2}$ = 0.00 V *vs.* SHE), (ii) $CH_3OH$ ($E^{\circ}_{CO_2/CH_3OH}$ = 0.04 V *vs.* SHE) and (iii) CO ($E^{\circ}_{CO_2/CO}$= -0.10 V *vs.* SHE)), *i.e.* possess great ability to reduce the carbon surface oxides ($E^{\circ}_{CO/C}$ = 0.52 V *vs.* SHE) [66]. The reduction of the oxygen-bearing groups present on the surface of the Vulcan XC72 support “heals” the interaction with the Pt nanoparticles, and hence facilitates their mobility and further collision. Keeping the same idea in mind, it is striking to note that the rate at which Pt crystallites are lost is the fastest (see Table III-2) when CO is present in solution, that for the most negative value of the Gibbs energy of the reaction $\Delta G$. The reduction of oxygen-bearing groups of the carbon support by $H_2$, CO or $CH_3OH$ finds also support in the literature. Indeed, in a temperature-programmed reduction and temperature-programmed desorption study, Roman-Martinez *et al.* [67] evidenced that $H_2$ assists the desorption and the reduction of carboxylic acid anhydride and quinone containing groups present on a HSAC into water. Obviously, the experimental conditions are largely different in the study of Roman-Martinez (gas phase, elevated temperatures) and in our study (liquid electrolyte, strong electric field, low temperatures) but a closer look to background-subtracted CO stripping voltammograms in Figure III-10 shows that the same phenomena may occur under polarization. Indeed, a negative current is observed in the background-subtracted CO stripping voltammogram at around 0.60 < *E* < 0.70 V *vs.* RHE, which is a potential zone where electrons are transferred on quinone/hydroquinone groups [1] or pyrone-like structures (combination of non-neighbouring carbonyl and ether oxygen atoms at the edge of the graphene layers) [57].

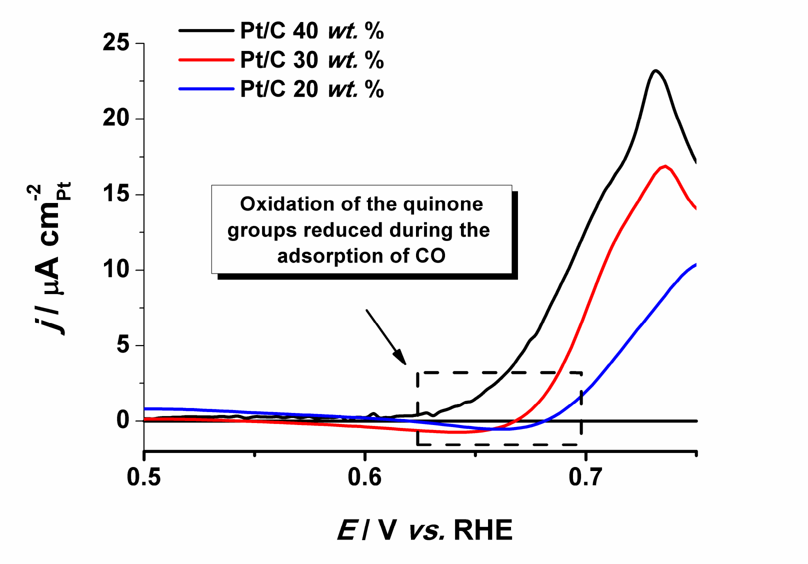

Figure III-10. Background-subtracted CO stripping voltammograms performed on different Pt/C electrocatalysts. The negative current in the potential region 0.60 < *E* < 0.70 V *vs.* suggests that $CO_{surf}$ groups were at least partially reduced during the adsorption of CO at *E* = 0.1V *vs.* RHE. Each voltammogram is the average of three measurements. Electrolyte: 0.1 M $HClO_4$; $v = 0.020$ V $s^{-1}$; $T = 20$ °C.

Figure III-10 strongly suggests that extended polarization of the electrode in the presence of CO in solution reduces part of the $CO_{surf}$ groups. Consequently, an increased oxidation current is observed on the first positive-going potential scan, and results in the negative current in the background-subtracted CO stripping voltammograms. Keeping this idea in mind, we also performed potential cycling in $O_2$-containing solution, all other experimental conditions being kept identical as in Figure III-4.

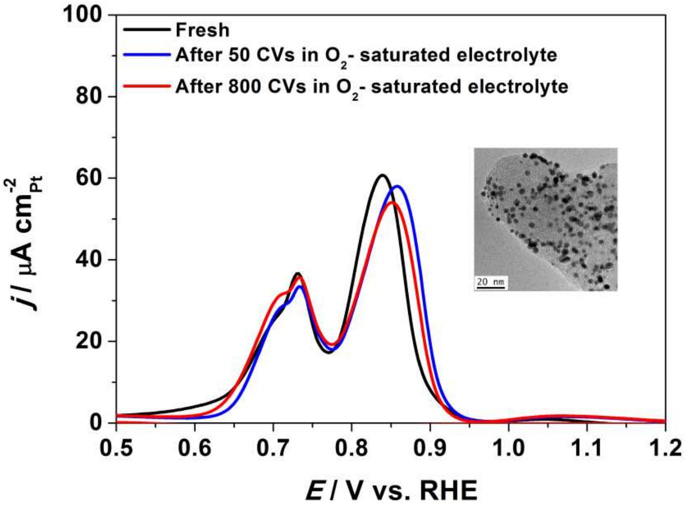

Figure III-11. Background-subtracted CO stripping voltammograms recorded on Pt/C 40 wt. % before/after 50 and 800 cycles between 0.05 and 1.23 V vs. RHE in oxygen-saturated solution. The inset shows a representative TEM image of the Pt/C catalyst after the 800 potential cycles. Electrolyte: 0.1 M $HClO_4$; v = 0.020 V $s^{-1}$; T = 20 °C.

Figure III-11 shows that the shape of the CO stripping voltammograms remains largely unchanged during the durability test, which confirms that the migration of the Pt crystallites is restricted in oxidizing conditions (promoting the persistence of $CO_{surf}$ groups on the carbon surface). Also, the analysis of TEM images confirmed that the sintering of the Pt nanoparticles was kept to a low extent (Table III-2). Here again, the parallel with gas-phase catalysis is striking. Indeed, Sellin *et al.* [68] exposed Vulcan XC 72-supported Pt nanoparticles to heat-treatment at $T$ = 573 K under oxidizing, inert, and reducing atmospheres. They reported the agglomeration of the Pt crystallites and an increase of the mean crystallite size under 3% $H_2$/He, whereas little structural changes were detected under air.

## III. Conclusions

The results presented in this chapter evidenced that Pt crystallites are not immobile on a HSAC support but can collide, agglomerate and even coalesce under potential cycling conditions. Although bearing minor importance in terms of Pt surface area losses, this phenomenon may influence or even accelerate the rate of other degradation mechanisms, such as the electrochemical corrosion of the carbon support and the 3D Ostwald ripening. The migration rate of the Pt crystallites is the largest in CO-containing solution and decreases in the order CO > $CH_3OH$ > $H_2$. We postulate that the morphological changes of the Pt/C nanoparticles may be caused by (i) a change of the work of adhesion between the metal nanoparticles and the carbon support or (ii) to the reduction of the oxygen-bearing surface groups strongly interacting with the Pt nanocrystallites.

# CHAPTER IV

# CARBON CORROSION AND PLATINUM NANOPARTICLES RIPENING UNDER OPEN CIRCUIT POTENTIAL CONDITIONS

This chapter is based on the following article:

"**Carbon Corrosion and Platinum Nanoparticles Ripening under Open Circuit Potential Conditions**" by Z. Zhao, L. Castanheira, L. Dubau, G. Berthomé, A. Crisci, F. Maillard, submitted to J. Power Sources.

The contribution of the author of the present thesis includes the preparation and the measurement of the properties of the catalytic systems, the treatment and analysis of the electrochemical data and participation in preparation of the manuscript for the publication.

# I. Introduction

Proton-exchange membrane fuel cells (PEMFCs) attract much attention as a viable solution to curb our energy-related $CO_2$ emissions [1]. They directly convert the chemical energy of a fuel into electrical energy from the reaction with oxygen, without the intermediate formation of heat and mechanical energy as in conventional Carnot cycle-based engines. PEMFCs use porous electrodes made of ionomer-bonded carbon-supported Pt-based nanoparticles to accelerate the kinetics of the electrochemical hydrogen oxidation reaction (HOR) at the anode, and of the sluggish oxygen-reduction reaction (ORR) at the cathode. However, four catalyst degradation mechanisms modify their structure during PEMFC operation, and yield electrochemically active surface area (ECSA) loss: (i) metal nanoparticle aggregation and/or detachment [2-6], (ii) corrosion of the high surface area carbon (HSAC) support [7-10], (iii) 3D Ostwald ripening, where the smallest Pt crystallites dissolve preferentially, yielding the formation of $Pt^{z+}$ ions and their redeposition onto larger particles [2, 11-13]; and (iv) chemical reduction of the $Pt^{z+}$ ions in ion conductors, leading electrically disconnected Pt crystallites [2, 11-13].

Which mechanism is contributing most to the ECSA loss strongly depends on the initial size of the Pt-based crystallites, the robustness of the carbon support and the PEMFC operating conditions. At the anode (reducing electrode potential & gas atmosphere), Ostwald ripening and carbon corrosion play a minor role, but recent evidences were brought that Pt nanocrystallites migrate/aggregate over [3] or even detach from [5, 14] the carbon support. At the cathode (oxidizing electrode potential and gas atmosphere, presence of water), both the carbon support and the Pt-based nanoparticles are covered by surface oxides and thus unstable. Ostwald ripening and carbon corrosion are believed to be the major degradation mechanisms at this electrode [13-16]. The HSAC corrosion kinetics is rather sluggish at conventional PEMFC cathode operation potential, but is significantly increased for $E > 1$ V *vs*. RHE [9, 10, 17] or during electrode potential transients [5, 18]. Unfortunately, the HSAC support and the metal nanoparticles negatively interact with each other to accelerate the extent of ECSA loss. A recent study by electrochemical – Fourier transform infrared spectroscopy showed that carbon surface oxide species present on HSAC are dehydrogenated at low electrode potential *E* < 0.60 V vs. RHE on Pt/C, yielding the formation of CO/Pt [9]. At higher electrode potential *E* > 0.60 V vs. RHE, the formation of surface oxides on Pt facilitates the removal of the CO molecules and accelerates the carbon corrosion kinetics [9, 10, 19]. It is also worth noting that the corrosion of the carbon support is likely to facilitate the detachment/aggregation of the Pt nanoparticles.

A large part of our knowledge on the durability of PEMFC materials arises from accelerated stress tests (ASTs). Such tests combine variations of the electrode potential, the temperature, the relative humidity and the gas composition, yielding fast variations of the ECSA. Although very informative, they cause the occurrence of simultaneous degradation mechanisms (dissolution, redeposition, HSAC support corrosion, particle detachment, aggregation), and remain poorly informative from a mechanistic viewpoint. In particular, little is known about the effect of high cathode potential experienced by the cathodic electrocatalyst in PEMFC stacks during idle conditions (*i.e.* the time when only idle auxiliary load power is drawn from the stack) or open circuit voltage (during fuel cell shut-down). These conditions yield cathode potential close to 0.90 or 1.00 V *vs*. RHE, respectively and induce carbon weight losses over time [17, 20].

In this Chapter, suspensions composed of Pt/Vulcan XC72 powder, solid ionomer and water were aged for 3.5 years under air atmosphere. These conditions cause a mixed potential produced by simultaneous carbon support corrosion and oxygen reduction on Pt, and hence are believe to reproduce to some extent what happens in a PEMFC cathode at open-circuit potential (OCP) or under idling conditions. X-ray Photoelectron Spectroscopy (XPS), Raman spectroscopy and EC-FTIR measurements were used to monitor the structural and chemical changes associated with the carbon oxidation reaction (COR), and gain some insights in the reaction mechanism. Physical (high-resolution transmission electron microscopy) and electrochemical (cyclic voltammetry) techniques were used to monitor the changes in morphology and size of the supported Pt nanoparticles.

# II. Results and discussion

## A. Electrochemical characterization

Figure IV-1 shows cyclic voltammograms measured on the Pt/C 40 wt. % electrocatalyst before and after ageing for 1.5, 2.5 and 3.5 years under open-circuit conditions in air atmosphere (see experimental).

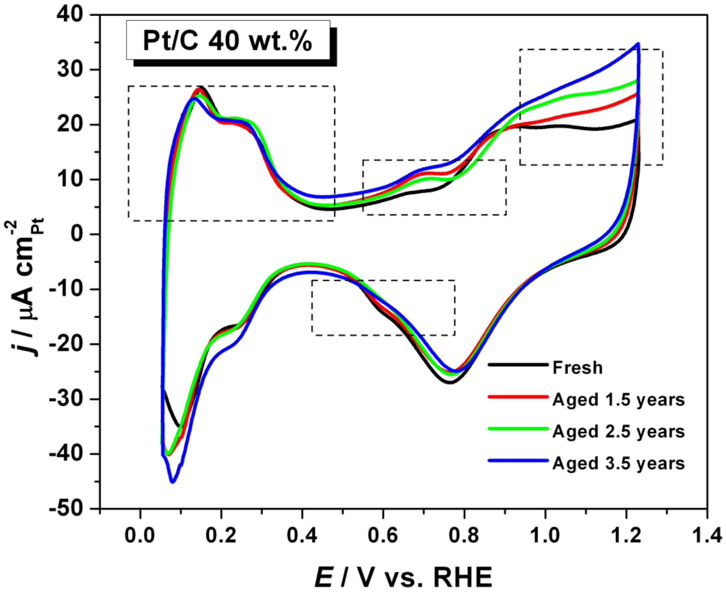

Figure IV-1. Cyclic voltammograms measured on Pt/C 40 wt. % after 0, 1.5, 2.5 and 3.5 years under OCP conditions. The current are normalized to the real surface area estimated by $CO_{ads}$ stripping coulometry. Each voltammogram is the average of three measurements. Electrolyte: 0.1 M $HClO_4$; $v$ = 0.020 V $s^{-1}$; $T$ = 20 °C.

In the potential region $0.05 < U < 0.4$ V *vs*. RHE, the features associated with the under-potential deposition/desorption of protons onto/from Pt nanoparticles remain nearly identical, which suggests that the mean Pt crystallite size does not change during the aging test [22]. This result agrees with the minor changes of the surface averaged mean particle size determined by TEM (Table 1). In the potential interval $0.5 < U < 0.8$ V vs. RHE, a broad oxidation peak ($I > 0$) can be distinguished, which we ascribe to electron transfer on quinone/hydroquinone groups [23]:

$$C{=}O_{(s)} + H^+ + e^- \leftrightarrows C\text{-}OH_{(s)} \qquad \text{Equation VI-1}$$

The electrical charge under this peak is increasing on the aged Pt/C electrocatalysts (positive-going potential sweep), pointing towards higher surface coverage with hydroquinone groups. Interestingly, the oxidation peak also shifts towards more positive potential (*ca*. 30 mV), and the reduction peak of quinone-type groups ($E = 0.60$ V vs. RHE) progressively disappears on the aged Pt/C samples. Assuming no pH variation, the positive shift of the oxidation peak may be rationalized by considering that hydroquinone groups experience different chemical environment on the fresh/aged Pt/C electrocatalysts. Indeed, previous studies have shown that a decrease in the number of aromatic rings causes an increase of the quinone/hydroquinone standard potential [23]. In this frame, the observed positive shift might sign the decrease in the number of aromatic rings resulting from the corrosion of the graphite-like crystallites. Another possibility is that the proportion of electron-withdrawing groups, such as carboxyl and anhydride, increases during the corrosion of the HSAC support. However, both scenarios cannot explain the decreased electrical charge under the reduction peak: the latter suggests that hydroquinone groups present on the surface of the aged Pt/C samples are irreversibly oxidized during the potential sweep.

Table IV-1. Evolution of the number and surface averaged mean particle size, the density of isolated and agglomerated particles and the loss of isolated Pt particles for three Pt/C commercial electrocatalysts during a 3.5 years period at open-circuit potential conditions.

| | 20 wt. % Pt/C | | 30 wt. % Pt/C | | 40 wt. % Pt/C | | | |
|---|---|---|---|---|---|---|---|---|
| | Fresh | After 2.5 years at OCP | Fresh | After 2.5 years at OCP | Fresh | After 1.5 years at OCP | After 2.5 years at OCP | After 3.5 years at OCP |
| $\bar{d}_N$ / nm | 2.5 | 2.6 | 2.7 | 2.8 | 3.5 | 3.8 | 3.6 | 3.6 |
| $\bar{d}$ $\bar{d}_S$ / nm | 2.9 | 3.1 | 3.4 | 3.6 | 4.5 | 4.9 | 4.8 | 5.1 |
| Number of isolated particles / µm$^{-2}$ carbon | 38000 | 33000 | 10800 | 8600 | 8000 | 6700 | 4300 | 2200 |
| Number of agglomerated particles / µm$^{-2}$ carbon | 2500 | 2600 | 2800 | 2500 | 2600 | 2100 | 2200 | 2500 |
| Total number of particles / µm$^{-2}$ carbon | 40500 | 35600 | 13600 | 11100 | 10600 | 8800 | 6500 | 4700 |
| Fraction of agglomerated particles / % | 6.2 | 7.3 | 20.6 | 22.5 | 24.5 | 23.9 | 33.8 | 53.2 |
| Loss of isolated particles / % | 0 | 13.2 | 0 | 20.4 | 0 | 16.3 | 46.3 | 72.5 |

## B. XPS measurements

The chemical nature of the surface oxygen-containing groups was investigated by XPS. Figure IV-2 shows the C1s XPS spectra measured on the fresh/aged Pt/C electrocatalysts. The C1s spectra comprises different peaks at 284.5, 285.6, 287.3 and 289.4 eV associated with C–C (sp$^2$ and sp$^3$-hybridized carbon atoms), C–O (hydroxyl, epoxy and ethers), C=O (carbonyl and/or quinone-like), and O–C=O (carboxylic acid, lactone, anhydride) bonds, respectively. Additional peaks at 291.4 and 292.9 eV are ascribed to C–F bonds in the Nafion® ionomer used as binder [11]. The lower binding energy component is assigned to C–F$_2$ groups while the higher binding energy component is ascribed to C–OF$_2$ and/or C-F$_3$ groups [24].

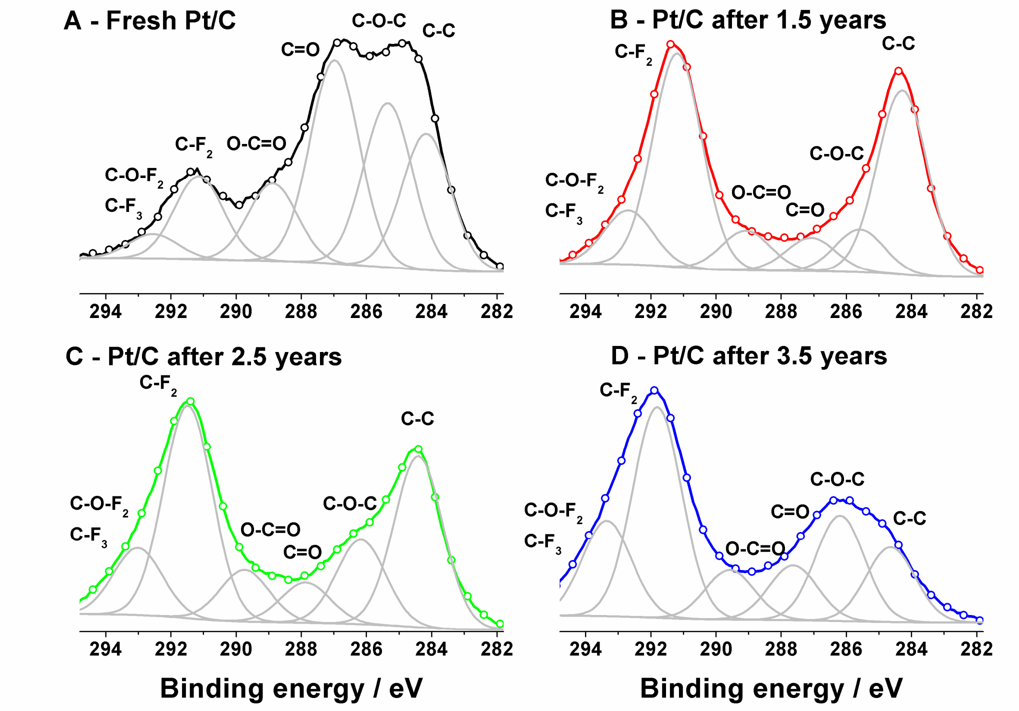

Figure IV-2. C1s spectra of fresh/aged Pt/C 40 wt. % powders.

Figure IV-2 illustrates that the most pronounced changes in the C1s spectra are observed in the carbon–carbon and carbon–oxygen related peaks. Assuming slight or no degradation of the perfluorosulfonated ionomer in our experimental conditions [11], the ratio of the (C–C) / (C–$F_2$ + C–$F_3$) XP areas (hereafter referred as the C/F ratio) allows a fast and semi-quantitative monitoring of the carbon content in each sample. Similarly, the O/F ratio allows fast comparison of the total oxygen content in each sample. The C/F ratio is continuously decreasing, most severely during the first 1.5 years, indicating fast corrosion of the Vulcan XC72 support. The O/F ratio is also decreasing between 0 and 1.5 years, most severely for C-O-containing functional groups (hydroxyl, ether and epoxy). These results suggest that the oxygen-containing surface groups present on the fresh Vulcan XC 72 are oxidized during the first 1.5 years of ageing at OCP. Finally, the slight increase of the O/F ratio observed during the following 2 years is believed to sign slow corrosion of the C–C bonds present in graphite crystallites, and will be confirmed by FTIR and Raman spectroscopy measurements.

## C. EC-FTIR measurements

The oxygen-containing functional groups present on the surface of the fresh/aged carbon supports were also identified by *in situ* Fourier-transformed infrared spectroscopy measurements. Figure IV-3 shows single-beam spectra measured at $E$ = 0.80 V *vs*. RHE on the fresh/aged Pt/C electrocatalysts. The FTIR spectra are normalized to a reference spectrum acquired at $E$ = 0.10 V *vs.* RHE, a procedure that allows (i) minoring the deformation induced by the O-H vibrational modes of water molecules and (ii) probing the vibrational modes of functional groups formed between $0.1 < U < 0.80$ V *vs*. RHE on the HSAC surface.

Different bands are present in Figure IV-3, and their assignment is summarized in Table IV-2. The weak absorbance bands between 1000–1300 $cm^{-1}$ are assigned to the C-O stretching (ν(C-O)) in carboxylic, ether-like, alcoholic and/or phenolic groups [9, 25, 26]. Those bands are very large confirming the complexity of the chemical environment (presence of aromatic rings and of various oxygen-containing functional groups). The band monitored at $\overline{\nu}$ = 1385–1390 $cm^{-1}$ on the fresh Pt/C sample is assigned to the C-O-

H bending in carboxyl groups [9]. In the C=O stretching region (ν(C=O)), between 1600–1850 cm$^{-1}$, the band at 1705-1730 cm$^{-1}$ indicates the presence of carbonyl groups of carboxylic acids, or lactone groups [25]. This band is very large and overlaps with the stretching of quinone groups at 1650 and 1670 cm$^{-1}$ [25] and the in-plane bending region of water molecules (δ(O-H)) at $\bar{\nu} \approx$ 1620-1640 cm$^{-1}$. The stretching of CO molecules adsorbed on the Pt surface (ν(C=O)/Pt) is observed at $\bar{\nu} \approx$ 2000 cm$^{-1}$, in agreement with our previous study [9]. Two bands of weak intensity at $\bar{\nu}$ = 2120 and 2150 cm$^{-1}$ reveal the presence of ketenes (C=C=O) on the 3.5 years aged Pt/C electrocatalyst [25]. Finally, the asymmetric O=C=O stretching vibration of $CO_2$ is observed at $\bar{\nu}$ = 2345 cm$^{-1}$.

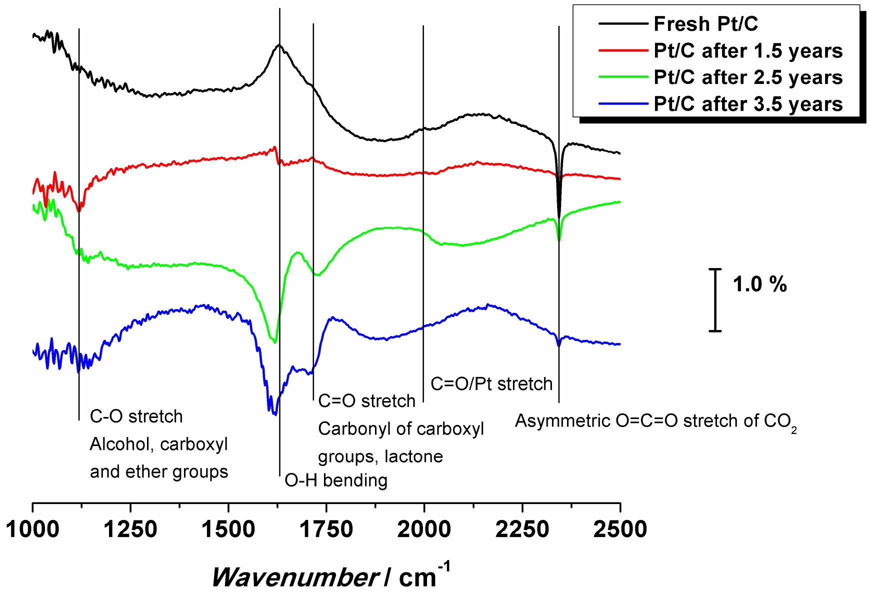

Figure IV-3. FTIR spectra acquired on the fresh/aged Pt/C 40 wt. % electrocatalysts. The reference spectrum was taken at *E* = 0.10 V *vs.* RHE.

Table IV- 2. Proposed functional groups observed on Vulcan XC 72, and their corresponding infrared assignment.

| Wavenumber / cm$^{-1}$ | Bond | Mode | Functional group |
|---|---|---|---|
| 1115 - 1120 | C–O | Stretching | Carboxylic, ether-like, alcoholic and phenolic |
| 1385 - 1390 | C–O–H | Bending | Carboxylic |
| 1620 - 1640 | O-H | in-plane bending | Water molecules |
| 1650 and 1670 | C=O | Stretching | Quinone |
| 1705 - 1730 | C=O | Stretching | Carbonyl of carboxylic acids, lactone |
| 2000 - 2030 | C=O/Pt | Stretching | Carbon monoxide adsorbed on Pt |
| 2120 and 2150 | C=C=O | Stretching | Ketenes |
| 2345 | O=C=O | Stretching | Carbon dioxide |

Two interesting features emerge from the comparison of the FTIR spectra on the fresh/aged electrocatalysts. Firstly, the chemical nature of the functional groups present on the fresh/aged Pt/C samples is identical (carboxylic, carbonylic, ether, and alcoholic groups). Secondly, the quantity of gaseous $CO_2$ produced at $E$ = 0.8 V *vs*. RHE is maximal on the fresh Pt/C and decreases with an increase in the aging time. Since all measurements were performed under identical experimental conditions (Pt/C loading on the Au electrode, electrolyte, temperature, duration of the potential steps), this suggests that the fresh carbon support is more prone to be oxidized into $CO_2$ than the aged carbon support. In agreement with his hypothesis, we observed a decreased CO/Pt band intensity at $E$ = 0.80 V *vs*. RHE on the aged Pt/C samples. Finally, we noticed that potential stepping from 0.1 to 0.8 V *vs*. RHE induces hydrophobicity / hydrophilicity of the fresh/aged carbon support, respectively. Indeed, the O-H bending vibrations of water ($\overline{\nu}$ = 1645 $cm^{-1}$) point positively on the fresh Pt/C sample, indicating that water molecules exit the “thin layer” formed between the electrode and the $CaF_2$ prism when stepping from low to high electrode potential. Conversely, water molecules enter the thin layer during this sequence on the aged Pt/C samples. In other words, the carbon surface is more hydrophilic at $E$ = 0.8 V *vs*. RHE than at the reference $E$ = 0.1 V *vs*. RHE potential on the aged Pt/C samples. It is also interesting to note that the O-H bending vibration of water molecules red-shifts by *ca*. 15 $cm^{-1}$ on the aged Pt/C samples, which indicates that the structure of the water molecules present in the “thin layer” changes from “organized water” (H-bonded) on the fresh Pt/C sample to “free water” on the aged Pt/C samples. Such result is believed to be related to variations in the wettability properties of the carbon support over time, induced by different oxygen content (see section 2.2) and by different fractions of $sp^2$ and $sp^3$ carbon atoms (see Section 2.4) in the fresh/aged Pt/C samples.

## D. Raman spectroscopy measurements

Raman spectroscopy allows probing the degree of graphitization of the fresh/aged Vulcan XC72 carbon particles [6, 27, 28]. The vibrational band present at *ca*. 1355 $cm^{-1}$ in Figure IV-4, namely the D1 band, is attributed to the amorphous or disordered structure of carbon ($sp^3$-hybridized carbon atoms), and the G band at *ca*. 1595 $cm^{-1}$ is ascribed to the ordered graphitic domains of the HSAC support ($sp^2$-hybridized carbon atoms) [29-32]. The slight shoulder at *ca*. 1615 $cm^{-1}$ is ascribed to the D2 band, and corresponds to a defect structure of graphite [28]. Figure IV-4 presents selected Raman spectra measured on the fresh/aged Pt/C catalysts. On the fresh Pt/C, both the high intensity of the D bands and the broadness of the G band indicate that the carbon support possess a highly disorganized structure that is consistent with the turbostratic structure of Vulcan XC72 [23]. After 1.5 years of ageing at OCP, the decreased intensity of the D bands suggests preferential oxidation of the defects of the Vulcan XC72 support (disordered graphitic lattice, graphene layer edges, surface graphene layers). This agrees with the general statement that defect sites are preferential sites for the initiation of the carbon oxidation reaction [33]. After 2.5 years and 3.5 years of aging at OCP, both the D1 band and the G band broaden, indicating that the carbon black support is continuously oxidized during the aging test. The persistence of the D1 band strongly suggests that corrosion also proceeds on the graphite crystallites, in agreement with the XPS measurements that evidenced slight increase of the O/F ratio during this period. These results confirm that the carbon oxidation kinetics is fast during the first 1.5 years, most likely on the disordered domains of the Vulcan XC 72 material, and then slows down because the remaining carbon particles possess a more ordered graphitic structure, which is more difficult to oxidize.

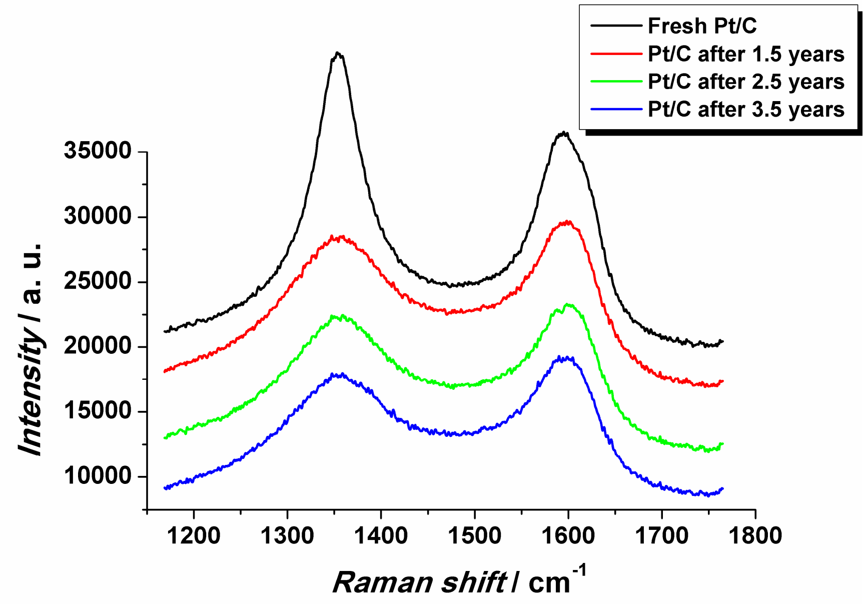

Figure IV-4. Selected Raman spectra of the fresh Pt/C electrocatalyst and after 1.5 years, 2.5 years and 3.5 years of ageing under OCP conditions.

## E. Change of the Pt/C structure by electrochemical and electron-based techniques

Finally, we discuss the structural consequences of the carbon corrosion for the supported Pt nanoparticles. Electron microscopy images were used to determine (i) the number and the surface averaged mean Pt particle size, (ii) the density of isolated/aggregated Pt nanoparticles, (iii) the total Pt particle density defined as the sum of isolated and aggregated nanoparticles per $\mu m^2$ of the carbon support, (iv) the fraction of aggregated Pt particles and (v) the percentage of isolated Pt particles lost during the durability test. In electrochemistry, we made use of the structure sensitivity of the $CO_{ads}$ electrooxidation reaction to detect *in situ* the aggregation of the carbon-supported Pt particles. Indeed, aggregated Pt particles feature a $CO_{ads}$ electrooxidation pre-peak, which is shifted *ca.* 50 mV negative versus the main $CO_{ads}$ electrooxidation peak (on isolated Pt/C particles) [34-40]. Additionally, the position of the main $CO_{ads}$ stripping peak shifts toward positive potential when decreasing the Pt particle size [34-37].

Figure IV-5 shows the background subtracted $CO_{ads}$ stripping voltammograms measured after different life stages: fresh, after 1.5 years, 2.5 years and 3.5 years. Two distinct $CO_{ads}$ electrooxidation peaks can be distinguished on the fresh sample: a broad peak initiating at *ca*. 0.65 V *vs*. RHE, which is composed of different contributions (at $E$ = 0.69, 0.72 and 0.75 V *vs*. RHE), and a main peak at *ca*. 0.84 - 0.85 V *vs*. RHE with some tail on the right-hand side of the peak. Upon aging, the charge under the $CO_{ads}$ electrooxidation pre-peak increases at the expense of the main peak. Concomitantly, the position of the main $CO_{ads}$ electrooxidation peak remains nearly unchanged (slight negative shift of the $CO_{ads}$ electrooxidation from 0.85 to 0.84 V *vs*. RHE). These results indicate an increased fraction of aggregated Pt nanoparticles in the Pt/C sample and minor changes of the mean crystallite size, in agreement with the particle size distributions established from TEM images (Figure IV-5, right hand side). They also account for the considerable loss of isolated Pt particles presented in Table IV-1 (formation of Pt aggregates from “isolated” Pt particles that moved and aggregated upon corrosion of the carbon support). The density of isolated Pt particles decreases by a factor of 4 during the aging sequence, while the fraction of aggregated Pt particles remains nearly identical.

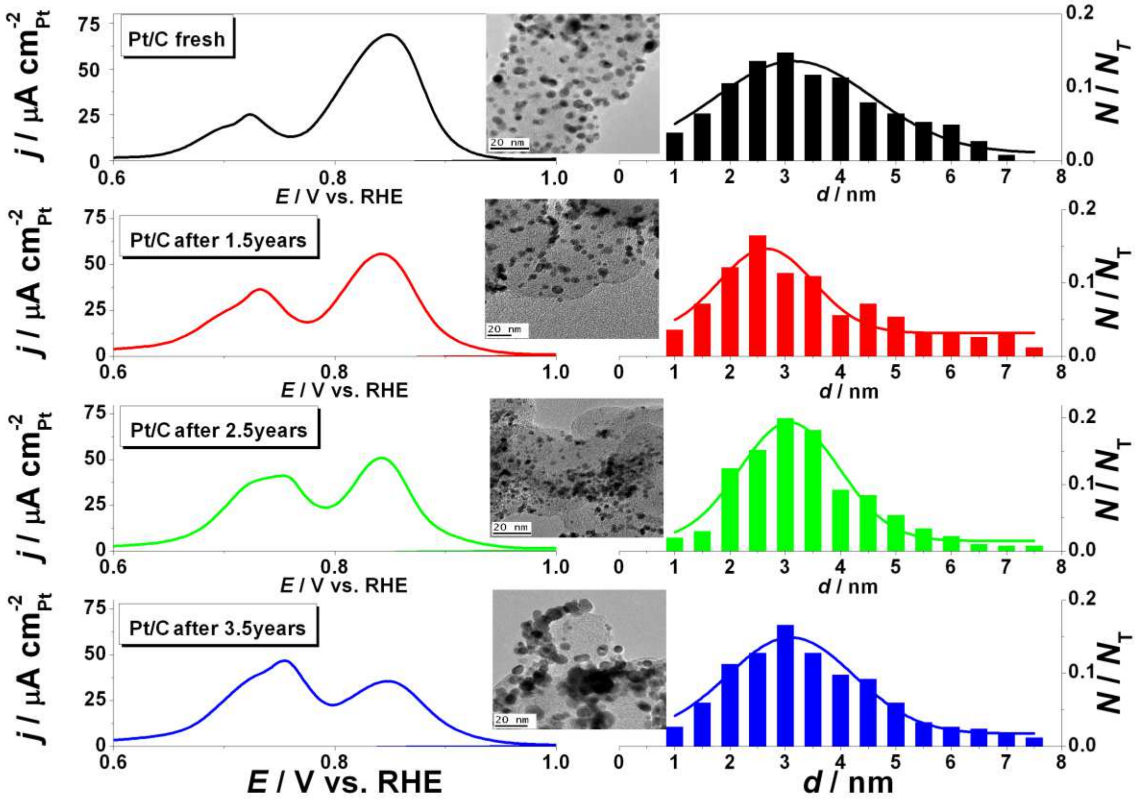

Figure IV-5. Averaged background subtracted CO stripping voltammograms (left) and particle size distributions (right) of fresh and aged Pt/C 40 wt. %. Representative TEM images of the aged Pt/C catalysts are shown in the insets. The current are normalized to the real surface area estimated by $CO_{ads}$ stripping coulometry. Each voltammogram is the average of three measurements. Electrolyte: 0.1 M $HClO_4$; $v$ = 0.020 V $s^{-1}$; $T$ = 20 °C.

Interestingly, this trend is valid whatever the Pt weight fraction (Figure IV-6). $CO_{ads}$ stripping experiments performed on Pt/C 20 wt%, 30 wt. % or 40 wt. % reveal that the charge under the $CO_{ads}$ electrooxidation pre-peak increases at the expense of the main peak. Concomitantly, the position of the main peak remains nearly identical.

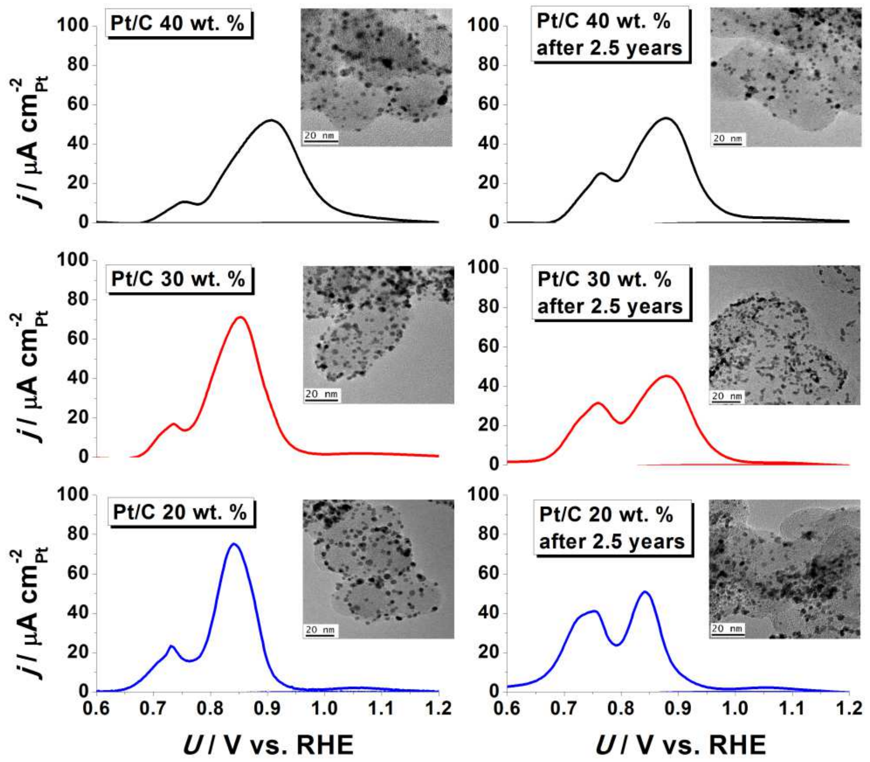

Figure IV-6. Averaged background subtracted CO stripping voltammograms and representative TEM pictures of fresh and aged Pt/C catalysts used in study. The current are normalized to the real surface area estimated by CO stripping coulometry. Each voltammogram is the average of three measurements. Electrolyte: 0.1 M $HClO_4$; $v$ = 0.020 V $s^{-1}$; $T$ = 20 °C.

The morphological changes of the Pt nanoparticles were quantified by a proper analysis of representative TEM images (Figure IV-7). The fraction of isolated Pt particles decreases very fast, this trend being maximal for the catalyst with the highest Pt weight fraction (40 wt. %). Since this catalyst possess the lowest inter-particle distance and the highest Pt/C coverage (calculated as the ratio between the surface area of Pt particles and the surface area of carbon support), the facile aggregation of Pt nanoparticles is not surprising. The density of aggregated Pt particles remains nearly constant over time (within the incertitude of this method) indicating that isolated and aggregated Pt nanoparticles are detached from the carbon support or that the size of the Pt aggregates increases over time.

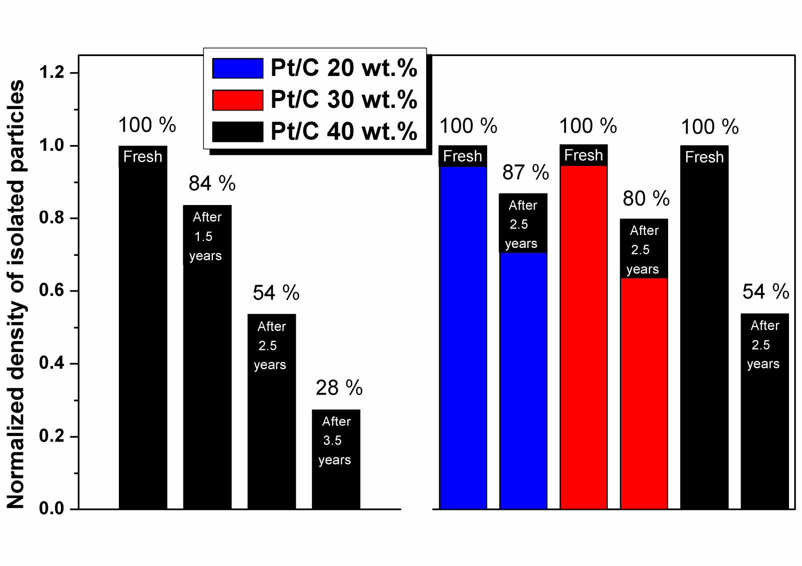

Figure IV-7. Normalized density of isolated particles for fresh and aged Pt/C catalysts having different weight fractions.

## F. Insights into the carbon corrosion mechanism

The results obtained in this study bridge structural and chemical changes observed during the corrosion of a HSAC support. The decreased C/F and O/F ratios in XPS and the large quantity of gaseous $CO_2$ produced at $E$ = 0.80 V *vs*. RHE on the fresh Pt/C sample in EC-FTIR measurements indicate that the oxygen-containing functional groups present on the fresh Vulcan XC72 particles are easily oxidized over the first 1.5 years under OCP conditions in air atmosphere. This nicely agrees with the higher corrosion rates observed on pre-oxidized carbon black materials or carbon nanofibres [41-43]. Raman measurements (decreased D bands intensity over the first 1.5 years) provide evidences that these oxidized domains are associated with disordered domains of the carbon support and defects sites of the graphitic lattice. In the second stage of the COR, Raman spectroscopy results show that organized domains of the HSAC support (graphitic carbon, $sp^2$-hybridized) are also oxidized, the rate of this process being much smaller than that observed on the non-graphitic regions of the HSAC support. The corrosion of the organized domains of the carbon support produces mostly $CO_{surf}$ groups as indicated by XPS and EC-FTIR measurements, and to a minor extent, $CO_2$ molecules at *E* = 0.80 V *vs*. RHE. This translates by the persistence of the D1 band in Raman measurements. As a consequence of the COR catalysis by Pt, the nanometre-sized Pt particles move and detach from the HSAC support, as evidenced by combined electron microscopy and electrochemical techniques.

# III. Conclusions

Due to their turbostratic structure, the high surface area carbon supports used in proton-exchange membrane fuel cells possess a large variety of oxygen-containing functional groups identified as hydroxyl, ether, carbonyl, and carboxyl groups. Upon ageing in air atmosphere under OCP conditions, the disordered domains of a Vulcan XC72 support (non-graphitic, $sp^3$-hybridized) are first oxidized. This translates by production of gaseous $CO_2$ at PEMFC relevant cell voltage in FTIR measurements (*E* = 0.80 V *vs*. RHE). In the second stage of the corrosion of the Vulcan XC72 support, Raman spectroscopy measurements indicate that the ordered domains (graphitic carbon, $sp^2$-hybridized) are also oxidized, the rate of this process being much smaller than that of the non-graphitic regions. The corrosion of the organized domains produces mostly $CO_{surf}$ groups, and to a minor extent, $CO_2$ molecules at *E* = 0.80 V *vs*. RHE. Electron microscopy and electrochemical techniques reveal a continuous loss of nm-sized Pt particles over time, which is rationalized on the basis of the Pt-catalysed carbon corrosion.

# CHAPTER V–EFFECT OF CATALYST LAYER THICKNESS AND PT LOADING ON THE ORR ACTIVITY

The contribution of the author of the present thesis includes the preparation and the measurement of the properties of the catalytic layers, and the treatment and analysis of the experimental data.

# I. Introduction

As shown in the previous chapters, three major degradation mechanisms occur in PEMFC catalytic layers: (i) metal nanoparticle aggregation and/or detachment [1-5], (ii) corrosion of the high surface area carbon support [6-9], and (iii) Ostwald ripening (dissolution/redeposition of the Pt crystallites) [10, 11]. The aging of the Pt-based/C nanoparticles yields: (i) a decrease of the particle density, (ii) the preferential dissolution of the nanoparticles with size smaller than 2 nm, (iii) an increased fraction of aggregated Pt nanoparticles. These morphological changes induce larger values of the average interparticle distance (IPD), defined as the average distance between two neighbouring nanoparticles over time.

The oxygen reduction reaction, which is the cathodic reaction in the PEMFC, is a multi-step reaction for which reaction/re-adsorption/transport effects [12-16] and thus the IPD are important. Indeed, the ORR is believed to proceed either directly to $H_2O$ in a $4e^-$ pathway (reaction 1 in Figure V-1) or in a series of two $2e^-$ steps (reactions 2 and 3) [17]. $H_2O_2$ may be also decomposed on the electrode surface in the non-electrochemical step 4 or desorb in solution (reaction 5).

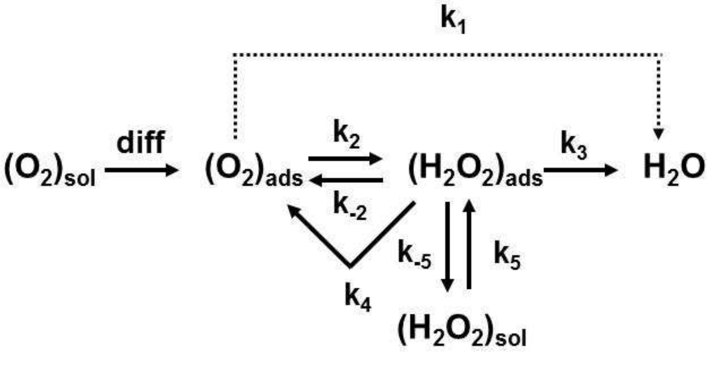

Figure V-1. Pathways of the oxygen reduction reaction on Pt surfaces in acid solution, as suggested in the early work of Bagotoski [18] and Wroblowa [19].

Consequently, the efficiency of the ORR is directly linked to the IPD: on highly loaded Pt/C electrocatalyst (low IPD value), or by extrapolation extended surfaces, the probability for $H_2O_2$ molecules to re-adsorb and further react on a neighbouring particle is high. In this case, the average number of electrons produced during the reduction of a dioxygen molecule ($n_e$-) approaches 4. Conversely, high values of the IPD translate into a low probability for $H_2O_2$ molecules to be further re-adsorbed on the Pt surface and hence into decreased values of $n_e$-. Convincing experiments of Chen *et al.*, [12] using the "single particle approach", showed that the amount of $H_2O_2$ detected on the Pt electrodes strongly increases, while the value of $n_e$- decreases from *ca*. 4 to 3.5 electrons under enhanced mass transport conditions. Schneider *et al.*,[13] using arrays of Pt particles deposited onto GC, demonstrated that decreased coverage of the carbon surface with Pt yields 10-20-fold increase of the $H_2O_2$ yield in the potential interval from 0.90 to 0.30 V *vs*. RHE, that is a potential region where the contribution of GC to the $H_2O_2$ production is negligible.

On Pt/Vulcan XC72 nanoparticles, Antoine *et al*. [20] did not observe any influence of the Pt loading on the $H_2O_2$ production. However, these results should be critically reconsidered by noting that $H_2O_2$ produced at the Pt surface has to diffuse within the porous rotating disk electrode (RDE) to be detected at the ring. As explained above, the probability of $H_2O_2$ to be detected at the ring strongly depends on the Pt to C weight fraction and on the thickness of the Pt/C film deposited onto GC. With thick catalytic layer, $H_2O_2$ possess high probability to be re-adsorbed and further reduced into $H_2O$ on neighbouring Pt nanoparticles. Conversely, for thin catalytic layers, the probability for $H_2O_2$ molecules to escape and be detected at the ring is higher. Ruvinskiy *et al*. [15, 16] combined experimental studies and a finite element modelling to take into account the influence of the thickness of the catalyst layer and the carbon surface coverage with Pt on the ORR mechanism. The authors convincingly showed that the ORR mechanism comprises both the "direct $4e^-$" and a "series $2e^- + 2e^-$" pathway and proposed that (i) the reaction fully proceeds via the $H_2O_2$ mediated pathway below 0.80 V *vs*. RHE and (ii) $H_2O_2$ further reacts via chemical decomposition step rather than direct electrochemical reduction. Summing up, there are numerous evidences in the literature that the number of Pt sites present on the electrode may impact the ORR mechanism and kinetics.

In addition to its importance as an ORR intermediate, $H_2O_2$ molecules play a key role in the durability of PEMFC electrodes. Indeed, the hydroperoxyl (HOO•) and hydroxyl (HO•) radical species generated during the ORR are extremely aggressive towards the carbon support, and lead to Pt nanoparticle detachment. Therefore, the fraction of $H_2O_2$ molecules must be kept to a very low content to guarantee a long-term use of the Pt/C-based catalytic layers or, in other words, the direct $4e^-$ pathway must be privileged.

This chapter aims at shedding light on the kinetic effect on ORR of decreasing coverage of the carbon support with Pt that occurs in the lifetime of a PEMFC. For that purpose, we used two model Pt/Sibunit electrocatalysts with low weight fraction (1.5 or 5 wt. %) and low specific surface area ($S_C \sim 6\ m^2 g^{-1}$), which were prepared by Dr. P. Simonov at the Boreskov Institute of Catalysis in Novosibirsk (Siberia).

# II. Results and discussion

## A. Physical characterization

Figure V-2 displays TEM pictures of the Pt/Sibunit electrocatalysts as well as the values of the mean particle size. Similarly to what was observed for Pt/C E-TeK electrocatalysts, the mean Pt nanoparticle size increases with an increase of the metal loading. This trend may appear surprising for low-loaded Pt/Sibunit catalysts. However, Sibunit-176K carbon possess a much lower specific surface area ($S_C = 6\ m^2\ g^{-1}$) than Vulcan XC72 ($S_C = 254\ m^2\ g^{-1}$), which was employed in Chapter III. In terms of morphology of the metal nanoparticles, the Pt to C weight fractions of 1.5 and 5 wt. % achieved on Sibunit-176K would translate into 40 and 70 wt. % on Vulcan XC72, respectively. The low specific surface area of the carbon support mostly suppresses one mechanism of interaction between the metal phase and the carbon support (mechanical trapping of metal nanoparticles at micropore mouth), and facilitate the aggregation of the nanometre-sized electrocatalyst.

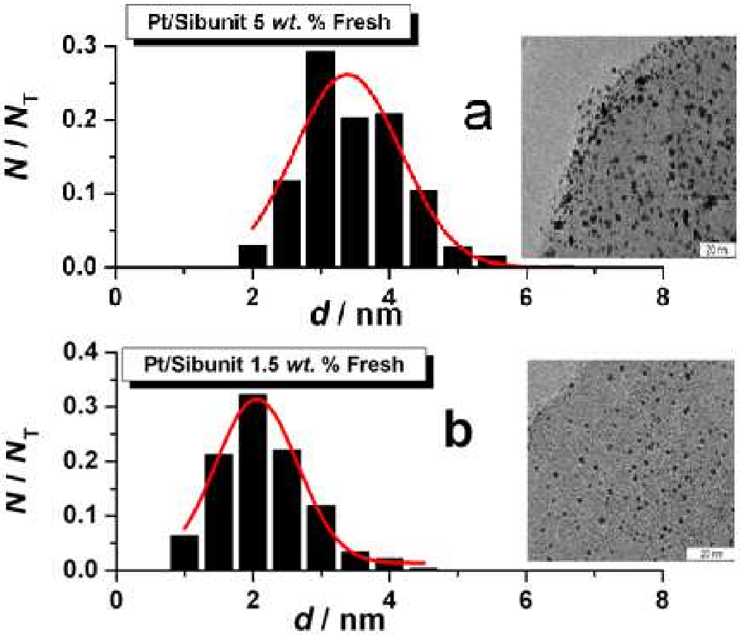

Figure V-2. Representative TEM images and associated particle size distributions for Pt/Sibunit 5 wt. % (a) and Pt/Sibunit 1.5 wt. % (b). To establish the particle size distribution, only the isolated round-shaped Pt nanoparticles were considered.

The closest distance between two metal nanoparticles (CPD) is a relevant parameter to quantify the extent of reaction/transport/re-adsorption effects mentioned in the introduction. The CPD was calculated as:

$$CPD = IPD - \bar{d}_N = (\sqrt{\pi\rho\ d_N^3 S_c \frac{100-y}{6\sqrt{3}y}}) - \bar{d}_N \qquad \text{Equation V-1}$$

Here IPD is the interparticle distance, $\rho$ is the density of Pt (g nm$^{-3}$), $\bar{d}_N$ is the number averaged mean particle size (nm), $S_c$ is the specific surface area of the carbon support ($nm^2$ $g^{-1}$), and $y$ is the weight percentage of Pt in Pt/C catalysts. For that calculation, we assumed hexagonal packing of Pt nanoparticles and used the equations developed by Watanabe *et al*. [21] and modified by Maillard *et al*. [22]. These values as well as the density of isolated/aggregated Pt nanoparticles are shown in Table V-I.

Table V-1. Closest particle distance, number and surface averaged mean particle size, density of isolated/aggregated Pt particles and loss of isolated Pt particles for the Pt/Sibunit electrocatalysts before/after potential cycling in oxidizing/reducing atmosphere.

| | Pt/Sibunit 5 wt. % | | | Pt/Sibunit 1.5 wt. % | | |
|---|---|---|---|---|---|---|
| | Fresh | After 50 potential cycles in $O_2$-containing atmosphere | After 50 potential cycles in CO-containing atmosphere | Fresh | After 50 potential cycles in $O_2$-containing atmosphere | After 50 potential cycles in CO-containing atmosphere |
| Closest particle distance /nm | 1.9 | 2.1 | 3.2 | 1.4 | 1.4 | 3.0 |
| Pt surface coverage/ % | 74.5 | 70.05 | 58.54 | 47.4 | 47.4 | 32.21 |
| $\bar{d}_N$ / nm | 3.3 | 3.5 | 4.2 | 1.5 | 1.5 | 2.2 |
| $\bar{d}_S$ / nm | 3.8 | 3.9 | 4.7 | 1.8 | 2.0 | 2.6 |
| Density of isolated particles / $\mu m^{-2}$ carbon | 9500 | 8700 | 6500 | 15800 | 15500 | 13000 |
| Density of aggregated particles / $\mu m^{-2}$ carbon | 2000 | 2000 | 3000 | 650 | 500 | 1100 |
| Total density of particles / $\mu m^{-2}$ carbon | 11600 | 10700 | 9500 | 16450 | 16000 | 14100 |
| Fraction of aggregated particles / % | 17.2 | 18.7 | 31.6 | 3.9 | 3.1 | 7.8 |
| Loss of isolated particles / % | 0 | 8.4 | 31.6 | 0 | 1.9 | 16.1 |

## B. Electrochemical characterization

Figure V-3 shows the CO stripping voltammograms obtained on the Pt/Sibunit electrocatalysts. The CO stripping on Pt/Sibunit 5 wt. % features two electrooxidation peaks located at *E* = 0.71 V *vs*. RHE and *E* = 0.79 V *vs*. RHE. As discussed in the previous chapters, the low potential pre-peak is due to the electrooxidation of CO molecules adsorbed on aggregated Pt nanoparticles, and the high potential peak is ascribed to the electrooxidation of CO molecules on "isolated" Pt nanoparticles. The existence of isolated and aggregated Pt nanoparticles is confirmed in Figure V-3a, and in Table V-I. On Pt/Sibunit 1.5 wt. %, only one single CO electrooxidation peak is observed (Figure V-3b), which indicates that the extent of agglomeration was kept low on this sample in agreement with TEM observations.

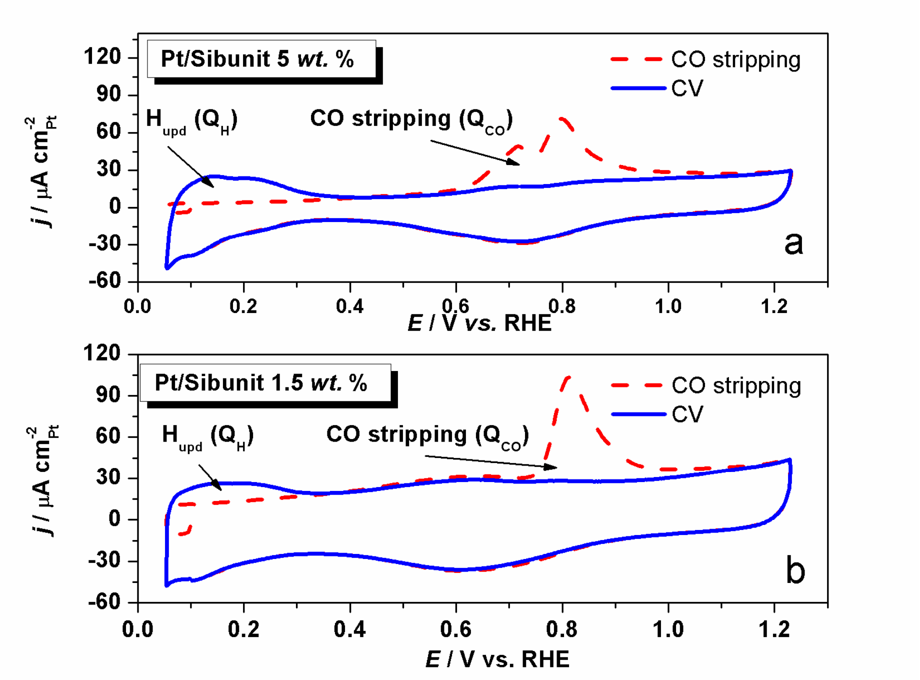

Figure V-3. The first and the second CO stripping voltammograms recorded on a Pt/Sibunit 5 wt. % (a) or on a Pt/Sibunit 1.5 wt. % (b) in CO-free 0.1 M $HClO_4$. v = 0.020 V $s^{-1}$; *T* = 20 °C.

Figure V-4 displays the variation of the ECSA with respect to the Pt loading for Pt/Sibunit 5 wt. % (a) and Pt/Sibunit 1.5 wt. % (b). The ECSA was determined either from the coulometry required to desorb a monolayer of $H_{upd}$ or to oxidize a monolayer of CO. The linear relationship observed for both materials indicate that 100 % of the Pt surface atoms are available for the electrocatalytic reactions. However, whereas the agreement between both techniques is excellent on Pt/Sibunit 5 wt. %, a strong deviation is observed for Pt/Sib 1.5 wt. %. A possible reason for that is the difference in the Pt mean nanoparticle size (Pt/Sibunit 5 wt. %: $\bar{d}_N$ = 3.3 ± 1 nm; Pt/Sibunit 1.5 wt. %: $\bar{d}_N$ =1.5 ± 1 nm). Indeed, recent work of Maillard *et al.* [23] underlined that using the coulometry of $H_{upd}$ results in dramatic underestimation of the surface area of Pt nanoparticles below 3.0 nm (by a factor of 2 for Pt particle sizes of *ca.* 1.5 nm).

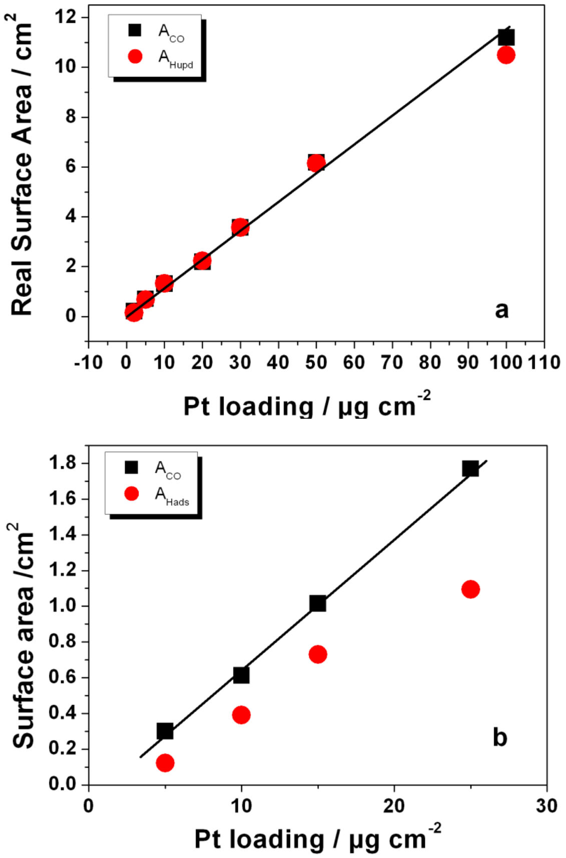

Figure V-4. Dependence of the electrochemically active Pt surface area determined from the coulometry required to adsorb a monolayer of $H_{upd}$ or oxidize a monolayer of CO on Pt/Sibunit 5 wt. % (a) or Pt/Sibunit 1.5 wt. % (b). 0.1 M $HClO_4$; $v$ = 0.020 V s$^{-1}$.

## C. Effect of the catalyst loading on the ORR activity

### 1. Rotating disk electrode measurements

Figure V-5 displays the voltammograms measured in $O_2$-saturated 0.1 M $HClO_4$ on Pt/Sibunit 5 wt. % and Pt/Sibunit 1.5 wt. % with different Pt loadings. Two remarkable features appear when the Pt loading decreases: (i) a shift of the ORR curves towards more negative electrode potential and (ii) a decrease of the diffusion-limited current. This behaviour is reflected on the dependence of the ORR onset potential (Figure V-6) and the ORR specific activity measured at *E* = 0.85 V *vs*. RHE (Figure V-7).

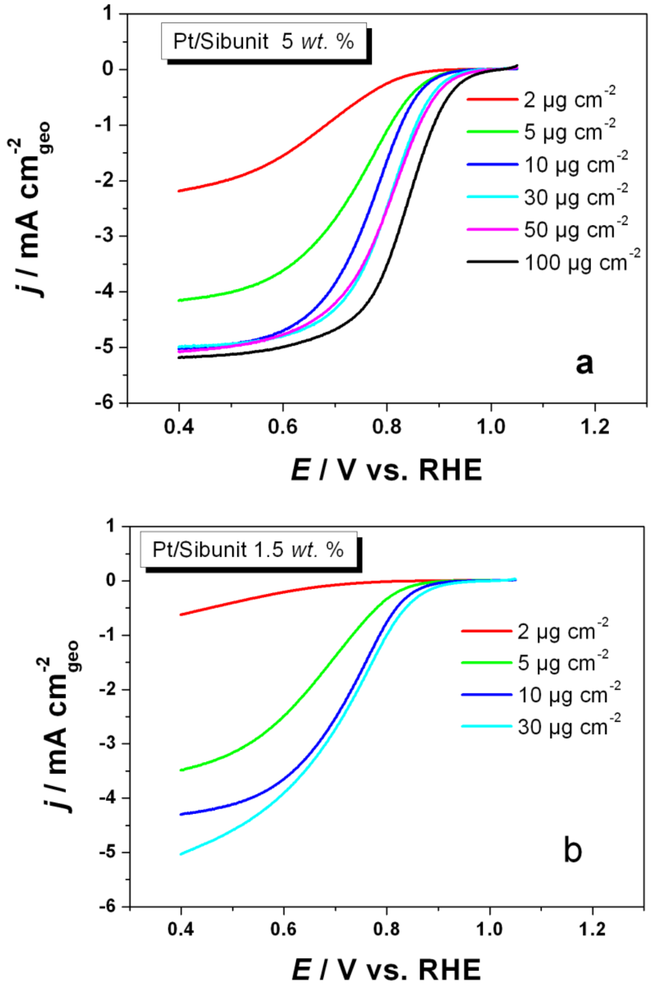

Figure V-5. Dependence of the ORR polarization curves on the Pt loading for Pt/Sibunit 5 wt.% (a) and Pt/Sibunit 1.5 wt. % (b). $O_2$-saturated 0.1 M $HClO_{4;}$ $v$ = 0.002 V $s^{-1}$;

negative-going potential sweep from 1.05 to 0.40 V *vs.* RHE; rotating speed 1600 rpm, *T* = 20± 1°C.The currents are normalized to the geometric area of the electrode (0.196 cm$^2$).

Similar observations were made in the studies of Inaba *et al*. [24], Mayrhofer *et al*. [3] and Ruvinskiy *et al*. [25]. Inaba *et al*. [24] attributed the decrease of the diffusion-limited current to the inhomogeneous distribution of the catalyst on the rotating disk electrode when the metal loading is low. Ruvinskiy *et al*. [25] investigated the dependence of the ORR activity on the thickness of the model catalyst layer composed of vertically aligned carbon nanofilaments loaded with Pt nanoparticles. They concluded that the phenomenon is intrinsic to the catalytic layers with low Pt loading, and attributed it to (i) the adsorption limitation on the Pt surface [25, 26] and (ii) the decreasing number of electrons participating in the ORR, considering the more facile escape of the $H_2O_2$ intermediates.

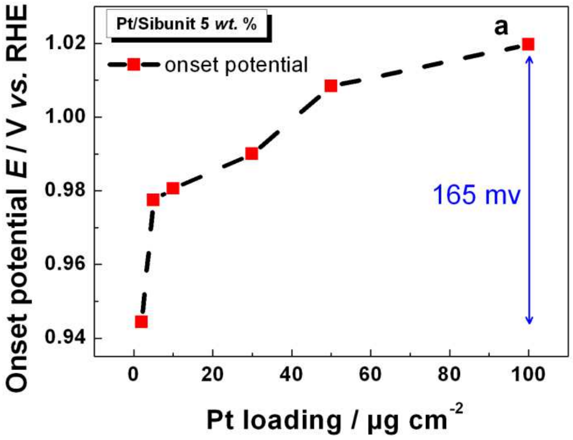

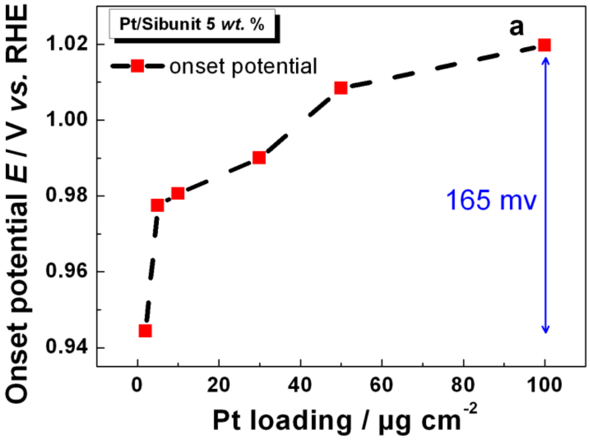

Figure V-6. Variation of the ORR onset potential for different Pt loadings for Pt/Sibunit 5 wt. % catalyst (a) and Pt/Sibunit 1.5 wt. %. $O_2$-saturated 0.1 M $HClO_{4;}$ sweep rate 0.002 V $s^{-1}$; negative-going potential sweep from 1.05 to 0.40 V *vs.* RHE; rotating speed 1600 rpm, $T = 20 \pm 1$°C.

Figure V-7 shows the influence of different Pt loadings on the ORR specific activity reported at $E$ = 0.85 V *vs.* RHE. It is clear that Pt loadings superior to 40$\mu g_{Pt}$ $cm^{-2}$ are best adapted to perform reliable ORR measurements on Pt/Sibunit 5 wt. %. Indeed, the diffusion limited current approaches the value that is predicted on an extended Pt surface by the Levich equation, and the ORR specific activity is stable. Conversely, adjusting the Pt loading for Pt/Sibunit 1.5 wt. % catalyst is not trivial. The latter should be sufficiently large to reach the diffusion-limited current predicted by the Levich equation. However, thick catalyst layers yield additional mass-transport limitations, and induce error in the determination of the ORR specific activity.

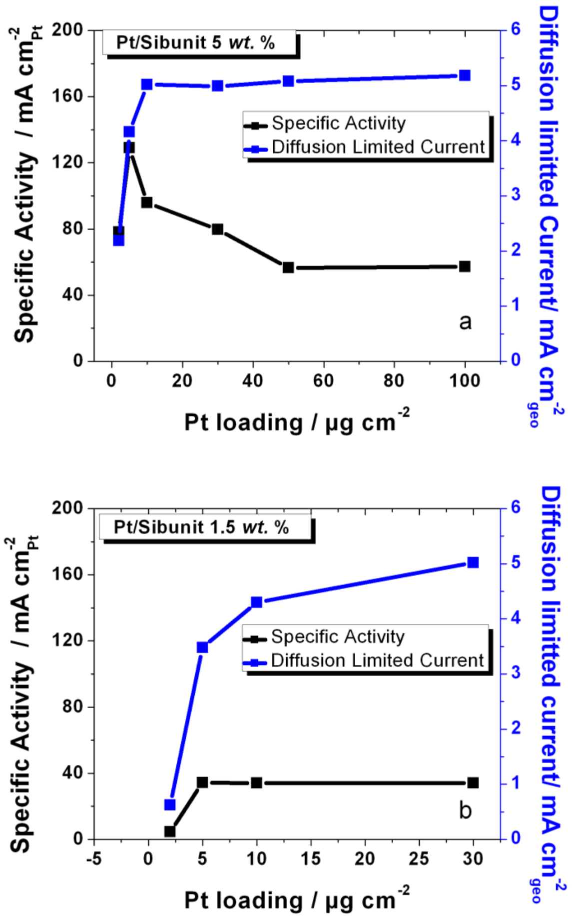

Figure V-7. Dependence of the ORR specific activity measured at $E$ =0.85 V *vs*. RHE and of the diffusion-limited current with respect to the Pt loading for Pt/Sibunit 5 wt. %(a) and Pt/Sibunit 1.5 wt. % (b). $O_2$-saturated 0.1 M $HClO_4$; sweep rate 0.002 V $s^{-1}$; negative-going potential sweep from 1.05 to 0.40 V *vs.* RHE; rotating speed 1600 rpm, $T = 20 \pm 1$°C.

## 2. Rotating ring-disk electrode measurements

Figure V-9 shows the ORR polarization curves recorded as a function of the disc electrode potential $E_D$ on Pt/Sibunit-based catalytic layers having different thickness. The measurements were performed in rotating ring-disc configuration, that is the disc and ring currents ($I_D$ and $I_R$, respectively) were recorded as a function of the disc electrode potential $E_D$. The ORR takes place on the central disc electrode and $H_2O_2$ molecules escaping from the catalytic layer are oxidized at the Pt ring polarized at $E$ =1.23 V *vs*. RHE. The current detected at the ring allows for the calculation of the effective number of transferred electrons during the ORR ($n_{e}$-).

Similarly to what was observed in the former section, the diffusion-limited current on the disc decreases with a decrease of the catalytic layer thickness (Figure V-8). The onset potential for the ORR also depends on the catalyst layer thickness, in agreement with the results of RDE measurements. Concomitantly, the fraction of $H_2O_2$ molecules detected at the ring steeply increases with a decrease of the catalyst layer thickness. These results qualitatively agree with those obtained by Inaba *et al*. on conventional Pt/C-based catalytic layers [24].

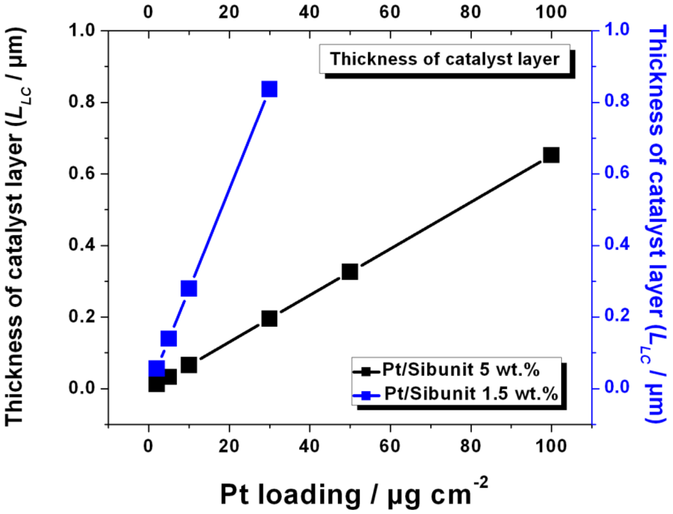

Figure V-8. Thickness of catalyst layers (µm) with respected to the Pt loading on the GC electrode (in µg $cm^{-2}$).

The thickness of the catalyst layer $L_{CL}$ (µm) was calculated using the following equation:

$$L_{CL}=\frac{V_{Pt/Sib}}{100A_{Electrode}}=\frac{m_{Pt/Sib}}{100\rho_{Pt/Sib}\cdot A_{Electrode}}=\frac{\gamma_{Pt/Sib}}{100\rho_{Pt/Sib}}\qquad \text{Equation V-2}$$

Here $V_{Pt/Sib}$ is the volume of the carbon-supported Pt nanoparticles ($cm^3$), $A_{Electrode}$ is the surface area of the glassy carbon electrode ($cm^{-2}$), $m_{Pt/Sib}$ is the weight of Pt/C deposited on the glassy carbon electrode (µg), $\rho_{Pt/Sib}$ is the apparent density of the carbon-supported Pt nanoparticles ($g\ cm^{-3}$),[c] and $\Upsilon_{Pt/Sib}$ is the Pt/Sib loading ($\mu g_{Pt/Sib}\ cm^{-2}$).

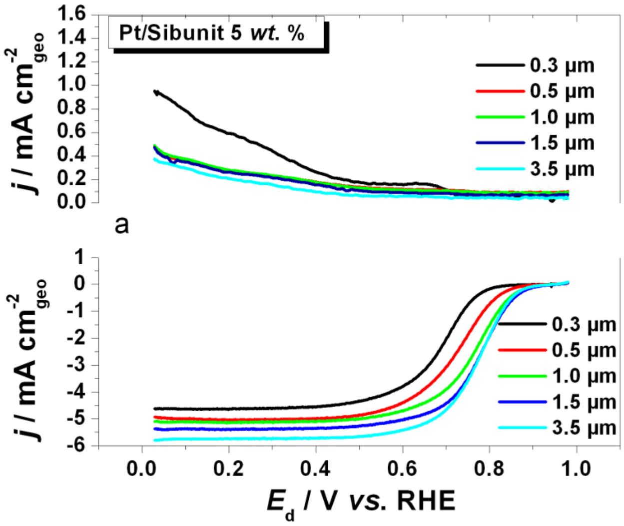

---

[c] The value of $\rho_{Pt/Sib}$ should be estimated from that of Pt ($\rho_{Pt}$ = 21.4 g $cm^{-3}$) and from that of the Sibunit carbon support ($\rho_{Sibunit}$). Since $\rho_{Sibunit}$ was unknown, we estimated it from that of another carbon support, which had similar specific surface area (Vulcan 3 N330), see Ref. [27]. The estimated values of $\rho_{Pt/Sib}$ are 2.55 and 3.22 g $cm^{-3}$ for Pt/Sibunit 1.5 and 5 wt. %, respectively.

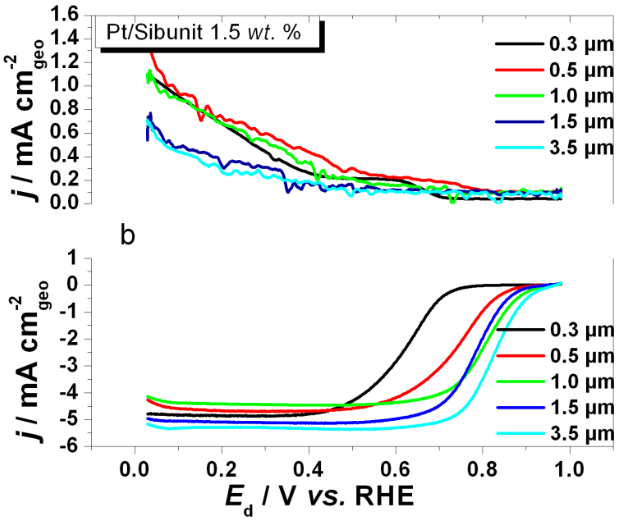

Figure V-9. Ring (above) and disc (below) currents measured on Pt/Sibunit 5 wt. % and Pt/Sibunit 1.5 wt. % catalysts in $O_2$-saturated 0.1 M $HClO_4$. *v* =2 mV s$^{-1}$, rotation speed 1600 rpm.

Figure V-10 features the variation of the fraction of $H_2O_2$ molecules and the effective number of transferred electrons during the ORR. These two parameters were calculated using standard methodology:

$$n_{e^-} = \frac{4I_D}{I_D + {I_R}/{N}}$$

Equation V-3

$$X_{H_2O_2} = \frac{2({I_R}/{N})}{I_D + ({I_R}/{N})}$$

Equation V-4

Where $I_D$ is the disc current, $I_R$ is the ring current, and *N* is the collection efficiency of the RRDE tip determined separately for each sample. A value of $n_{e^-}$ = 4 indicates that all the reacting $O_2$ molecules are reduced into $H_2O$ independently of the reaction mechanism (4 e$^-$ or 2 + 2 e$^-$) whereas $n_{e^-}$ values below 4 indicates that $H_2O_2$ molecules can escape from the catalyst layer.

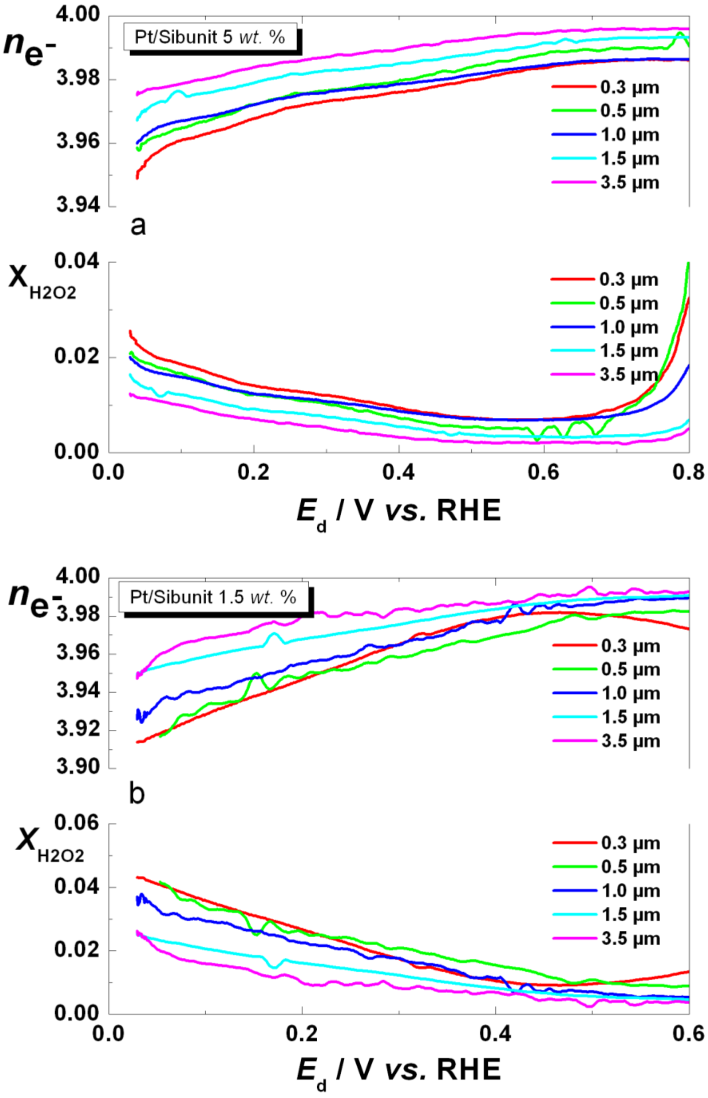

Figure V-10. Effective number of electrons transferred electrons (a) and fraction of $H_2O_2$ molecules produced during the ORR (b) on Pt/Sibunit 5 wt. % and Pt/Sibunit 1.5 wt. % in $O_2$-saturated 0.1 M $HClO_4$. $v$ =2 mV $s^{-1}$, rotation speed 1600 rpm.

As can be seen, the value of $n_{e^-}$ non-negligibly depends on (i) the Pt to C weight fraction and (ii) the catalyst layer thickness, and decreases with a decrease of these two parameters. These results confirm that the electrochemical reduction of $O_2$ molecules involves $H_2O_2$ as a main reaction intermediate, and proceeds via the series 2 + 2 $e^-$ mechanism. Indeed, at constant layer thickness, the probability for $H_2O_2$ molecules to re-adsorb on neighbouring Pt particles is lower for the electrocatalyst with the lowest Pt to C weight fraction. Similarly, a decrease of the catalyst layer thickness yields higher probability for $H_2O_2$ molecules to escape from the catalytic layer and to be detected at the ring. Again, this agrees with the results obtained by Ruvinskiy *et al*. [15] on Pt/vertically aligned carbon nanofilaments.

## D. Stability of Pt/Sibunit electrocatalysts in the presence of oxidizing and reducing gas

The electrochemical activity of Pt/Sibunit 5 wt. % and Pt/Sibunit 1.5 wt. % electrocatalysts for the CO monolayer electrooxidation is shown in Figure V-11. A CO electrooxidation pre-peak appears at about *E* = 0.71 V *vs.* RHE and a negative shift of the main peak is observed on Pt/Sibunit 5 wt. % with respect to Pt/Sibunit 1.5 wt. %. These features confirm larger Pt particle size and higher extent of aggregation [28-30] on the 5 wt. % Pt/Sibunit catalyst in good agreement with the data derived from the analysis of representative TEM images (Table V-1).

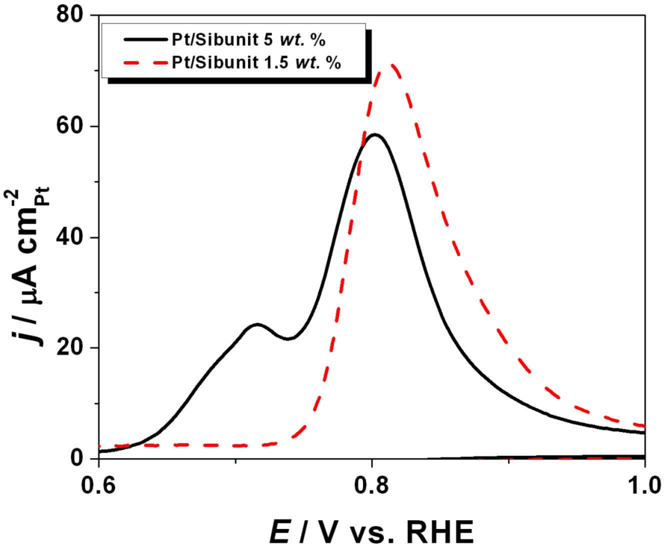

Figure V-11. Background-subtracted CO stripping voltammograms on Pt/Sibunit 5 wt. % and Pt/Sibunit 1.5 wt. % catalysts. The currents are normalized to the real surface area estimated from CO stripping. Electrolyte: 0.1 M $HClO_4$; $v$ = 0.020 V $s^{-1}$; $T$ = 20 °C.

Interestingly, repetitive CO stripping sequences cause a decrease of the charge under the main CO electrooxidation peak and an increase of the charge contained under the pre-peak. These results agree with those presented in Chapter III and indicate that the

Pt/Sibunit nanoparticles are mobile and agglomerate upon collision during the CO stripping sequences. The analysis of representative TEM images clearly evidences minor changes of the mean Pt particle size (Figure V-12) but a strong increase of the fraction of aggregated and/or non-spherical Pt/Sibunit nanoparticles (Figure V-12) at the expense of the isolated Pt/Sibunit particles.

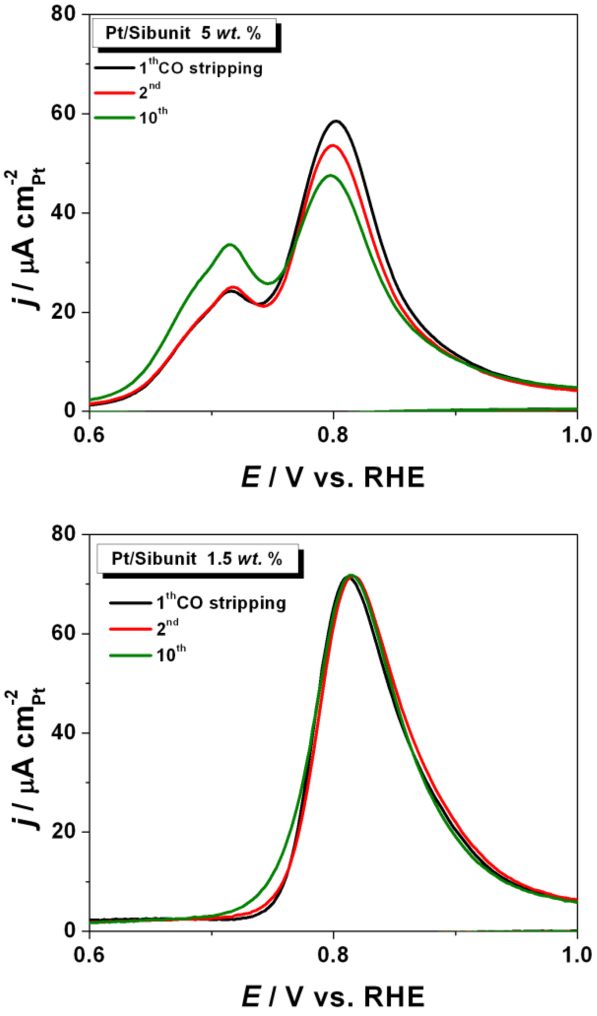

Figure V-12. Repetitive CO stripping voltammograms measured on Pt/Sibunit 5 wt. % (above) and Pt/Sibunit 1.5 wt. % (below). The currents are normalized to the real surface area estimated from CO stripping. Electrolyte: 0.1 M $HClO_4$; $v$ = 0.020 V $s^{-1}$; $T$ = 20 °C.

In order to estimate the stability of the two model electrocatalysts, 50 potential cycles were performed from 0.05 V *vs.* RHE to 1.23V *vs.* RHE in oxidizing ($O_2$-saturated) or reducing (CO-saturated) atmospheres. Before and after the ageing test, CO stripping voltammograms and TEM images were recorded to monitor the morphological changes of the Pt/Sibunit electrocatalysts (Figure V-13). It is interesting to note that the treatment under oxidizing atmosphere induces minor changes of the mean particle size but Pt particle detachment. Conversely, the Pt/Sibunit nanoparticles aggregate easily during the experiments in CO-containing atmosphere, in agreement with the results obtained in Chapter III. These results suggest that enhanced rate of Pt crystallite migration/aggregation under reducing atmosphere is common to different carbon supports with various structural properties.

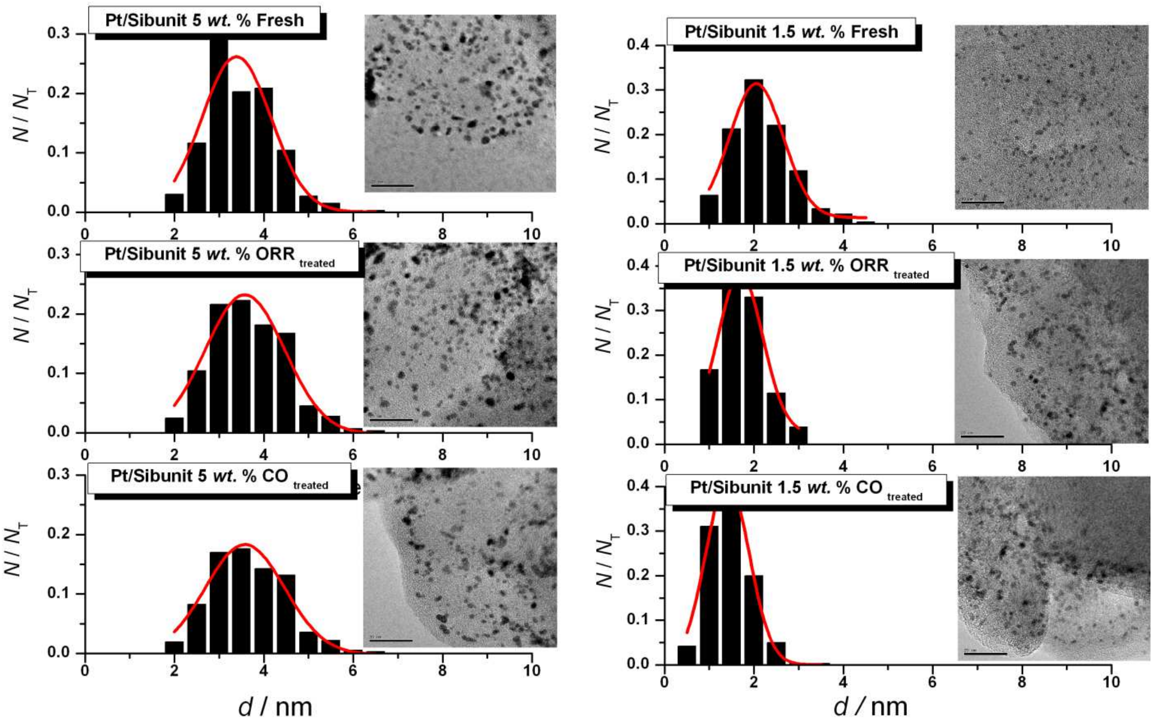

Figure V-13. Particle size distributions and representative TEM images of Pt/Sibunit 5 wt. % (left) and Pt/Sibunit 1.5 wt. % (right) before/after ageing in reducing or oxidizing environment (50 potential cycles from 0.05 V *vs.* RHE to 1.23 V *vs.* RHE in oxidizing ($O_2$-saturated) or reducing (CO-saturated) atmospheres, sweep rate 0.05 V $s^{-1}$). Electrolyte: 0.1 M $HClO_4$; $v$ = 0.020 V $s^{-1}$; $T$ = 20 °C

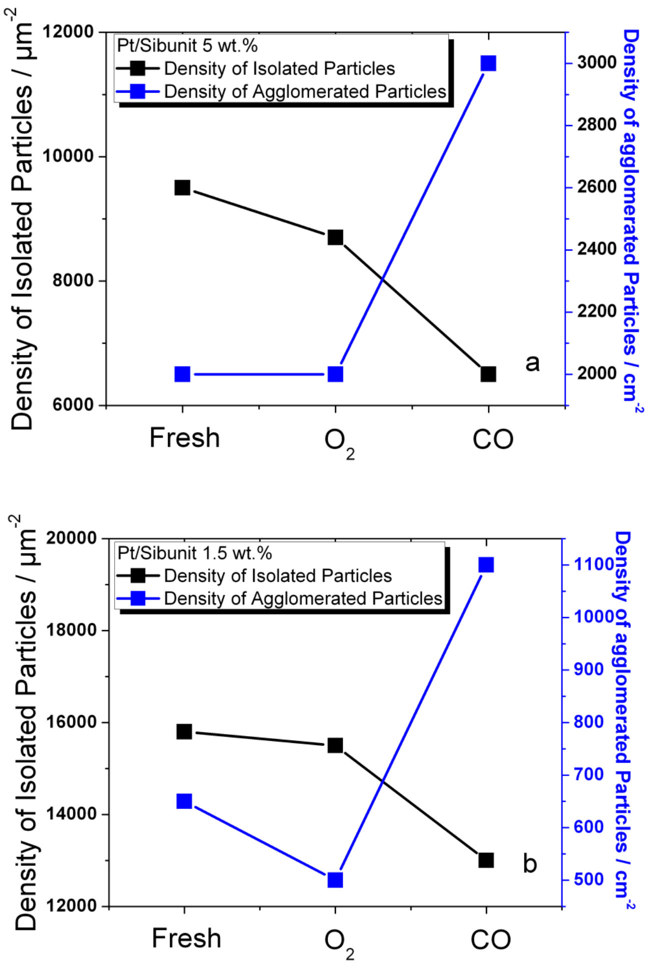

Figure V-14. Density of isolated particles and agglomeration on Pt/Sibunit 5 wt. % (left) and Pt/Sibunit 1.5 wt. % (right) before/after ageing in reducing or oxidizing environment.

## III. Conclusions

The results presented in this chapter suggest that the aging of the catalytic layers also impacts the ORR kinetics through transport and re-adsorption effects. This was highlighted using model Pt/Sibunit electrocatalysts and variable Pt loadings and catalytic layer thicknesses. The RDE and RRDE experiments performed on these two model electrocatalysts provided evidences that the ORR follows the series 2 + 2 e$^-$ pathway on Pt/Sibunit catalysts. Indeed, the average number of transferred electrons produced during the ORR decreases below 4 with the decrease of the catalyst layer thickness or the Pt loading. This is rationalized by considering the lower probability for $H_2O_2$ molecules to re-adsorbed and further reduced into water in the catalytic layer. We also found that Pt/Sibunit electrocatalysts face similar degradation mechanisms as Pt/Vulcan XC 72 used in Chapter III. Repetitive potential cycles in CO-containing electrolyte facilitate the migration and aggregation of Pt nanoparticles. Similarly, we observed that repetitive potential cycles in $O_2$-containing electrolyte cause a decrease of the density of isolated Pt nanoparticles. The latter however is believed to result from the detachment of the Pt nanoparticles following the increased production of $H_2O_2$ molecules at low electrode potential below $E$ = 0.80 V *vs.* RHE.

# CHAPTER VI

# PT NWS AS MORE ROBUST ELECTROCATALYSTS FOR PEMFC APPLICATIONS

This chapter is based on the following article:

"Pt NWs as more robust electrocatalysts for PEMFCs" by Z. Zhao, L. Dubau, F. Maillard, in preparation.

The contribution of the author of the present chapter includes the entirety of the experimental part (preparation and measurements of the properties of the catalytic systems), treatment and analysis of the experimental data and participation in preparation of the manuscript for the publication.

# I. Introduction

As it was mentioned in the previous chapters, the loss of ECSA is a major source of PEMFC performance degradation over time [1-10]. In an early study, Guilminot *et al*. [8] identified at least four possible degradation mechanisms for the nanometre sized Pt/C-based materials: (i) electrochemical dissolution/redeposition of the metal nanoparticles (Ostwald ripening) (ii) chemical redeposition and reduction of the $Pt^{z+}$ ions in the ionomer phase by $H_2$ molecules crossing over from the anode (iii) metal nanoparticle detachment induced by corrosion of the carbon support and (iv) crystallite migration.

Most of these effects arise from the nanometre dimension of the Pt crystallites used to catalyse the HOR at the anode and the ORR at the cathode. Indeed, the small size of the metal nanoparticles is beneficial to reach high specific surface area (and thus high mass activity), but favours their dissolution. The minimization of the overall surface energy of the total mass of electrocatalyst is the driving force of Ostwald ripening, [11] and the Gibbs–Thomson relation shows that the dissolution rate increases with a decrease of the Pt particle size [12]. The dissolution rate is also accelerated by the electrode potential and the load-cycle applied, [4, 13-17], the relative humidity [14] and the temperature [18, 19]. Similarly, we have seen in Chapter III that the adhesion between the metal nanoparticles and the carbon support is modified in the presence of reducing molecules, yielding increased mobility and aggregation of the metal nanocrystallites. Chemical and stable modification of the carbon support appears to be a promising way to circumvent this issue but is challenging with regards to the highly oxidizing PEMFC environment [20, 21]. Ultimately, non-supported catalysts may suppress the durability issues related to the carbon support. [d]

Another option to avoid durability issues related to the carbon support while maintaining high catalytic activity consists of using Pt-coated supports, [22-25] high surface area Pt nanowires (Pt NWs), Pt nanotubes or mesoporous Pt structures. Recently, Zhou,

---

[d] However, in the absence of a porous carbon support, the PEMFC catalytic layers might suffer issues related to insufficient $O_2$ mass-transport and poor water management.

Koenigsmann and Adzic [26-29] used Pt nanostructures with ultrathin one dimensional (1D) NW morphology to catalyse the electrooxidation of ethanol. The Pt nanostructures were shown to be composed of elongated single crystalline segments with smooth crystal planes that are connected by grain boundaries forming a NW structural motif. These structures possess proportionally less low surface coordinated surface atoms and hence are less prone to be corroded than the conventional Pt nanoparticles with zero-dimensional (0D)[e] morphology. In addition, the 1D nanostructures provide several beneficial features in terms of electrocatalysis [26-35] including (i) facile re-adsorption of reaction intermediates and hence maximization of the number of effectively transferred electrons per $O_2$/fuel molecule at the cathode/anode, respectively (see Chapter V), (ii) weaker bonding with oxygen-containing species [36]. Unlike the hard template methods, nanowires can be fabricated without additional templates, while they were obtained through the self-assembly of nanoparticles in a reverse micelle solution.

Recently, Sung *et al*. [34] synthesized Pt NWs (3 nm in diameter) in a mesoporous silicate mobile composition of matter (MCM-41) hard template with channel-like pores of uniform size. The authors reported improved specific and mass activity for the methanol oxidation reaction (MOR). Chien and Jeng [30] reported the synthesis of Pt and PtRu nanonetworks using a self-assembled, layered template of polystyrene nanospheres by chemical reduction deposition, and the performance of the DMFC cell based on the Pt and PtRu nanonetwork electrocatalysts was 3–4 times higher than that of the cell with conventional Pt and PtRu nanoparticle electrocatalysts. Kim *et al*. [31] reported the synthesis of Pt NWs via the polymer template method with improved mass activity for the MOR. However, the hard template method generally produces low metallic interconnectivity due to the poor continuity of precursors in the hard template. Also the removal of the hard template normally requires the use of hydrofluoric acid, which causes serious concerns for the environment and safety. Besides, the size and shape of the nanostructured materials are usually limited by the porous structure of the hard templates available. Thus, the soft template synthesis methods appear to be more suitable and flexible for the synthesis and control of the effective multi-dimensional Pt nanostructured electrocatalysts for fuel cell applications. Song *et al*. [33] developed a phase-transfer

---

[e] 0D, 1D, and 2D nanotructures –. Clusters, Nanowires, Sheet

method to prepare platinum NW networks with controllable cross-section diameter. Wang *et al*. [37] synthesized Pd NWs via a controllable self-assembly method mediated by the polysodium-p-styrenesulfonate polyelectrolyte, and the as-prepared Pd NW shows an enhanced electrocatalytic activity for the formic acid oxidation as compared to Pd NP/C electrocatalysts.

This short literature review shows that, despite their high initial metal loading, Pt NWs have great potential to replace nanoparticles in a PEMFC. In this chapter, we successfully synthesized Pt NWs catalysts with an average cross section diameter of about 2.1 ± 0.2 nm by a soft template method. The physical properties of the Pt NWs were characterized by TEM, SEM and XRD techniques. A 20 wt. % Pt/C catalyst (E-TeK) with similar particle size (2.5 ± 0.1 nm) and a 40 wt. % Pt/C catalyst (E-TeK) with larger particle size (3.5 ± 0.2 nm) were used as benchmark materials. The activity of the Pt NWs/C catalysts was tested for reactions of interest in PEMFC and DMFC including CO and MOR. We also focused on the stability of the Pt NWs/C catalysts in conditions mimicking fuel cell operation.

## II. Results and discussion

### A. Physical properties of Pt NWs/C catalyst

The Pt NWs were prepared by a soft template method using cetyltrimethylammonium bromide ($(C_{16}H_{33})N(CH_3)_3Br$, CTAB) as a surfactant. In typical synthesis conditions, a 10 mL of 20 mM $K_2PtCl_4$ aqueous solution was increasingly added to 10 mL of chloroform containing 40 mM CTAB under vigorous stirring conditions and $T$ = 20 °C. Previous experiments in similar conditions [33, 38-40] have suggested that wormlike micelles form under these conditions. The $K_2PtCl_4$ precursor was then reduced with the addition of a solution of 10 mL 30 mM $NaBH_4$ under stirring at a speed of 1000 rpm. The colour of the solution changes from light yellow to dark brown indicating the reduction of the Pt precursor to metallic Pt. Excess CTAB and chloroform were removed by flitting with 200 mL boiling ethanol(80 °C) and 1000 mL water (100 °C) until the solution was transparent after washing.

Figure VI-1 shows the TEM micrographs of the synthesized Pt NWs. The Pt NWs are interconnected, and form two-dimensional NWs with multi-grained boundaries. The average cross-sectional diameter of the Pt NWs is 2.1 ± 0.2 nm and the distribution in size and structure is very uniform. Some of the Pt NWs were then deposited on Vulcan XC-72 for electrochemical experiments. The aging test includes (i) 10 sequential CO stripping voltammograms, (ii) 50 and 800 potential cycling on Pt NWs/C in solutions containing Ar, CO and methanol or (iii) 1000 CVs and 5000 CVs on the pure Pt NWs, Pt NWs/C, Pt NP/C 20 wt.% and Pt NP/C 40 wt.% at *T* = 20 °C. CO stripping experiments were performed before/after the aging treatment.

## 1. Transmission Electron Microscopy characterization

Figure VI-1B displays a high resolution TEM image of the nanostructure of Pt NWs. This image shows that the Pt NWs are polycrystalline, with randomly oriented grains and varied orientations of the atomic lattice fringes. The HRTEM images also show that the Pt NWs are highly-defective materials with a high concentration of grain boundaries. The average cross section diameters of the Pt NWs was calculated by counting more than 50 different zones in the TEM images, and equals 2.1 ± 0.2 nm.

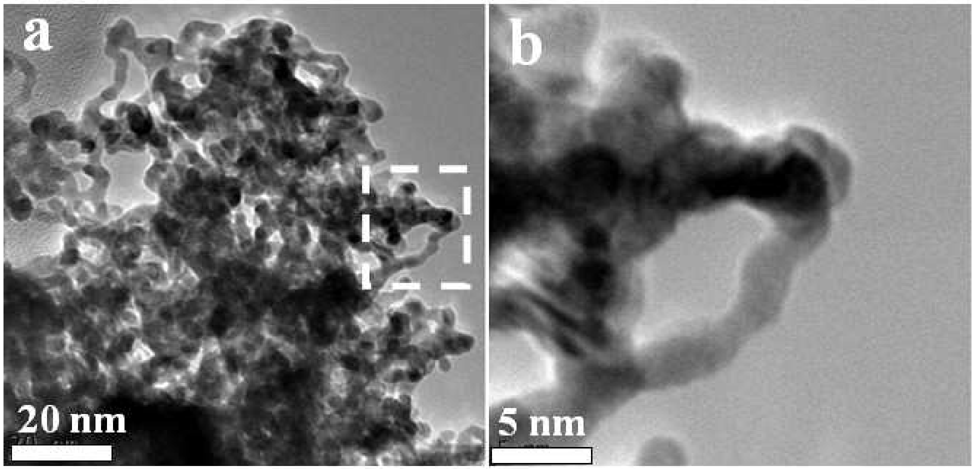

Figure VI-1. Representative TEM images of Pt NWs at low magnification (A) and Pt NWs at high magnification (B).

## 2. Scanning Electron Microscope (SEM) characterization

SEM images indicate that the Pt NWs are not single separated nanowires but form a complex 3D honeycomb structure (Figure VI-2). Similar morphology was recently reported by Wang and Zhou [26, 28, 36].

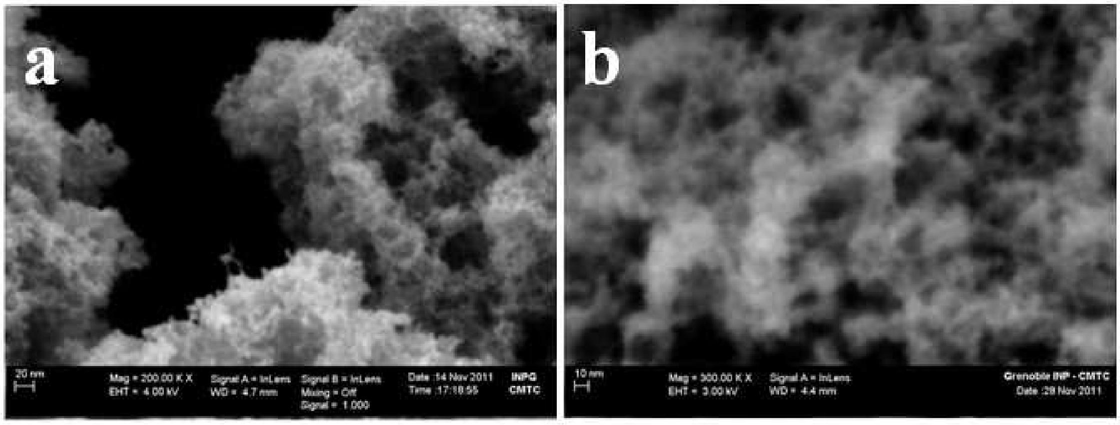

Figure VI-2. Representative SEM images of Pt NWs at low magnification (A) and Pt NWs at high magnification (B).

## 3. XRD characterization

Figure VI-3 shows the XRD patterns and the mean crystallite size of Pt NWs and Pt NPs (20 wt. % E-TeK). The average crystallite size $\bar{d}_{XRD}$ was estimated from the peak broadening in the X-ray diffractograms using the Scherrer equation [41].

$$\bar{d}_{XRD} = \frac{K\lambda}{B(2\theta)\times\cos\theta} \qquad \text{Equation VI-1}$$

Here $\bar{d}_{XRD}$ is the crystal dimension normal to the diffracting planes, $K$ is the Scherrer constant ($K$ = 0.89), $\lambda$ is the X-ray wavelength, $B_{2\theta}$ is the integral breath of the diffraction peak in terms of the 2θ angle in radians (the full width at half maximum is frequently used), and θ is the Bragg angle.

From Figure VI-3, the mean crystallite size of Pt NWs estimated by XRD is 2.0 nm, a value that is very similar to that of the diameter of the cross sections calculated from TEM images, and to the average mean particle size of the benchmark 20 wt. % Pt/C .

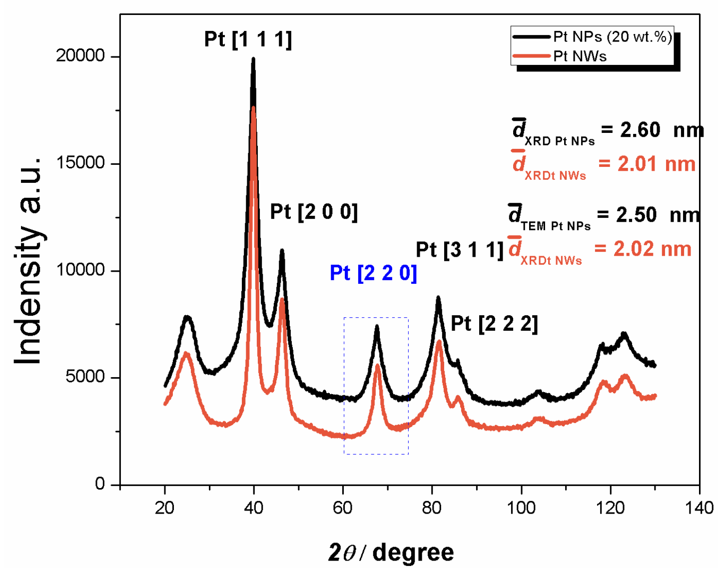

Figure VI-3. XRD patterns and mean particle size of Pt NWs and Pt/C 20 wt. %

We were also interested in knowing whether the Pt NWs possess, to some extent, preferential crystallographic orientation. The phenomenon of preferred crystallographic orientation (texture) means that certain crystallographic planes are oriented in a preferred manner [42]. The reasons for that include but are not limited to plastic deformation, and heterogeneous growth of particles. The texture coefficients (TCs) of the synthesized material were obtained by comparing the intensity of the diffraction peaks of Pt NWs with those of the benchmark Pt/C 20 wt. % material:

$$\mathrm{TC(hkl)} = \frac{\dfrac{I(\mathrm{hkl})_\mathrm{i}}{I_0(\mathrm{hkl})_\mathrm{i}}}{\dfrac{1}{N}\sum n \dfrac{I(\mathrm{hkl})_\mathrm{i}}{I_0(\mathrm{hkl})_\mathrm{i}}} \qquad \text{Equation VI-2}$$

Here $I(hkl)_i$ is the observed intensity of the $(hkl)_i$ plane; $I_0(hkl)_i$ the intensity of $(hkl)_i$ plane of the corresponding un-textured sample; $N$ is the total number of reflections taken into account. A value of TC > 1 indicates a preferred crystallographic orientation. If TC = 1, there is no preferential crystallographic orientation in the sample. Conversely, if for a certain plane, the ratio between the intensity of the diffraction peaks measured on the Pt NWs and on the Pt/C NPs is larger than one, the Pt NWs possess a preferred orientation for this plane. Obviously, the existence of preferred orientation for a certain plane implies that other planes have TC values < 1: indeed, the sum of the TC coefficients should equal *N*.

The XRD results show that the proportion of high-index Pt crystallographic planes, such as (220), (311) and (222), is larger in Pt NWs /C with respect to Pt NPs /C (E-TeK 20 wt %). Concomitantly, the TC values of the (111) and (200) orientations strongly decrease, more severely for the (111) planes. Such behaviour indicates that the growth of the Pt NWs is anisotropic, and confirms the presence of grain boundaries such as those imaged in the zoom of Figure VI-1.

Table VI-1. Texture coefficients values of Pt NWs

| Material | Crystallographic planes used for the calculation | | | | |
|---|---|---|---|---|---|
| Pt NWs /C | (1 1 1) | (2 0 0) | (2 2 0) | (3 1 1) | (2 2 2) |
| Texture coefficients | 0.78 | 0.93 | 1.04 | 1.20 | 1.07 |

## B. Enhanced durability of Pt NWs/C with respect to Pt NPs/C

### 1. Effect of subsequent CO stripping experiments

Based on the information obtained in the chapter III, we now use “CO stripping” voltammograms (i) as a rapid and facile method to probe the robustness of the Pt NWs/C and the Pt NPs/C in a reducing atmosphere. As shown in Figure VI-4, Pt NWs /C feature a single CO electrooxidation peak with a plateau at low electrode potential. Such experiment supports earlier conclusion of Maillard *et al*. [43, 44] that nanograined structures possess high activity for the electrochemical CO oxidation. This was attributed to the high defect density on this type of electrocatalysts (steps, intergrain boundaries), and fairly well agrees with what was observed in HRTEM in this chapter (see section II. A.1). Recent observations of Wang *et al.* [36] evidenced similar phenomena on Pt NWs/C, which the authors attributed to the faster $CO_{ads}$ surface mobility as well as to the larger fraction of grain boundaries on the Pt NWs surface.

Figure VI-4 shows the effect of 10 subsequent CO stripping voltammograms on Pt NWs/C and Pt NPs/C catalysts. Interestingly, the changes are minor on the Pt NWs/C relative to Pt NPs/C, which unambiguously shows that the Pt NWs/C catalyst is more stable in these "mild ageing conditions" than Pt NPs/C. Here, we postulate that the improved durability of Pt NWs/C catalysts may result from: (i) the improved contact surface area between the Pt NWs and the carbon support and (ii) the increase of the weight of Pt NWs/C with respect to Pt NPs/C, which possibly reduces the mobility of the metal phase.

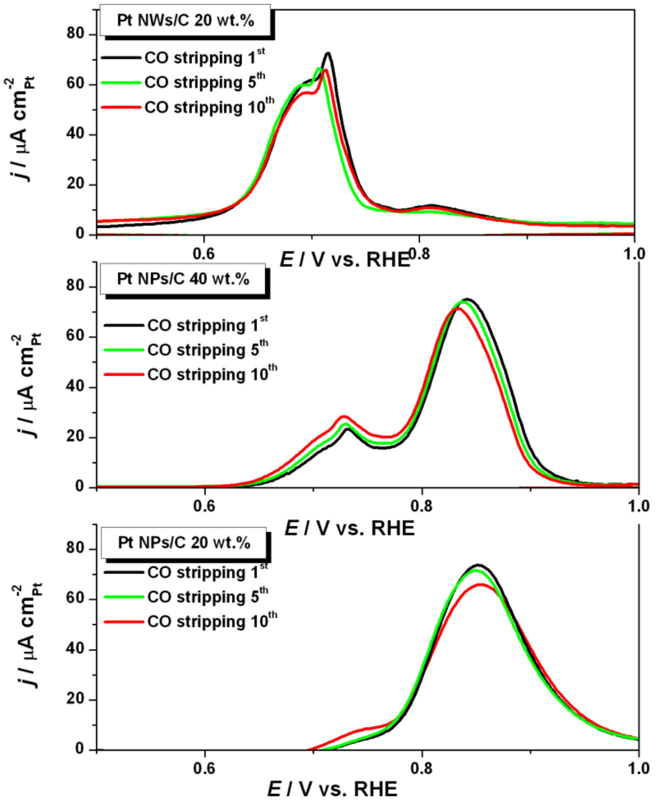

Figure VI-4. Repetitive background-subtracted CO stripping voltammograms on Pt NWs/C and Pt NPs/C electrocatalysts. The currents are normalized to the real surface area estimated from CO stripping coulometry. Electrolyte: 0.1 M $HClO_4$; $v = 0.020$ V $s^{-1}$; $T = 20$ °C.

## 2. Effect of reducing molecules such as CO and $CH_3OH$

We now estimate the robustness of the Pt NWs/C in the presence of reducing molecules in the electrolyte as we did for the Pt NPs/ in the Chapter III. Figure VI-5 shows the CO stripping voltammograms recorded on the fresh Pt NWs/C 20 wt. % before (plain line) and after (dashed line) 50 or 800 CVs in Ar or CO-saturated 0.1 M $HClO_4$ or in an electrolyte containing 0.5 M methanol.

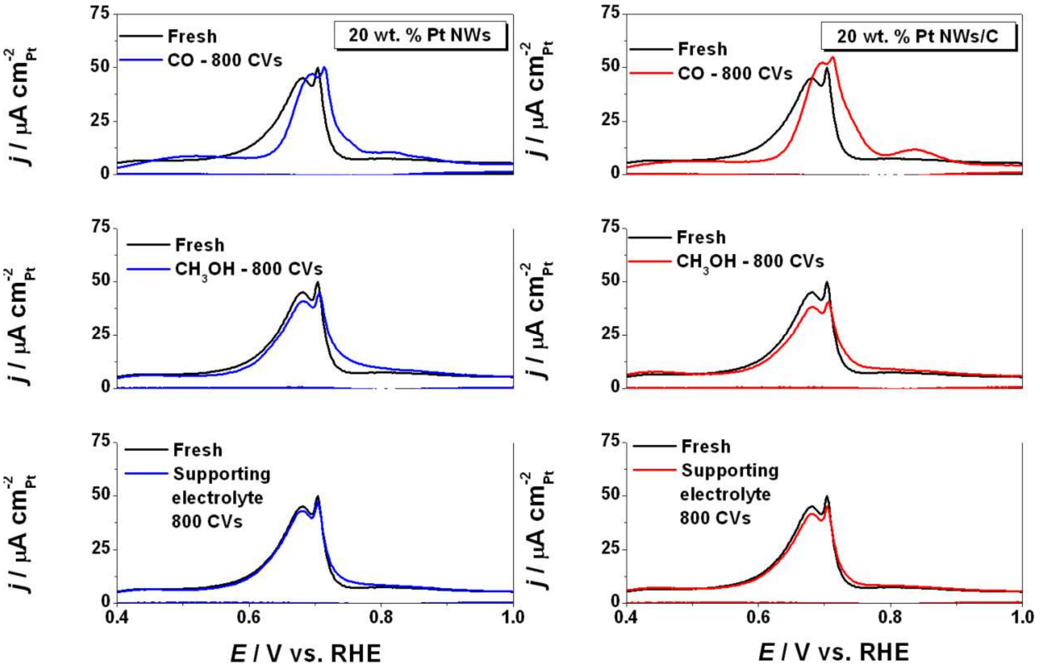

Figure VI-5. CO stripping on fresh/aged Pt NWs/C catalysts after 50 potential cycles (left) or 800 potential cycles (right) between 0.05 and 1.23 V *vs.* RHE in 0.1 M $HClO_4$ saturated with Ar, CO or containing 0.5 M methanol. *v* = 0.020 V $s^{-1}$; *T* = 20 °C.

Under Ar-saturated or in methanol-containing electrolyte, minor changes of the CO stripping voltammograms are detected. Given the strong sensitivity of the CO electrooxidation kinetics to the electrode structure, such observations indicate that the nature and the size of the crystallites in the Pt NWs as well as the fraction of structural defects did not change during the sequence. Here, it is worth recalling that for Pt NPs/C and under similar experimental conditions, the charge under the CO electrooxidation pre-peak continuously increased at the expense of the main peak and TEM images featured the formation of localized areas with high concentration of aggregated Pt particles (Figure III-4,. Interestingly, a slight tailing appears after the main peak in the CO stripping experiments, which to the present moment remains unexplained. Finally, in CO containing solutions, we found a positive shift of the main CO electrooxidation peak after 50 and 800 CVs. As discussed in Chapter III, this result point towards the “healing” of surface defects by potential cycling in CO-containing solution. The defects are the source of oxygen-containing species, and are necessary to oxidize the adsorbed CO molecules. Similar effect was observed on Pt NPs/C materials in Chapter III.

## 3. Effect of the carbon support

Figure VI-6 shows the CO stripping voltammograms recorded on 20 wt. % Pt NWs/C and 20 wt.% Pt/C catalysts before/after ageing treatment in a solution containing methanol. Similar to what was shown in chapter III, the electrochemical experiments suggest that the nanometre-sized Pt crystallites are mobile and agglomerate upon potential cycling in methanol-containing electrolyte. At variance, slightly changes are monitored both for the 20 wt. % Pt NWs/C. Interestingly, a small electrooxidation peak, located at potential more positive from that of the main peak, appears after extensive potential cycling on the unsupported Pt NWs. The latter indicates that some sites of the surface become less active for the electrooxidation of methanol and of its main reaction intermediate (CO). The reasons for that however remain largely unclear and are not the focus of the present Ph.D.

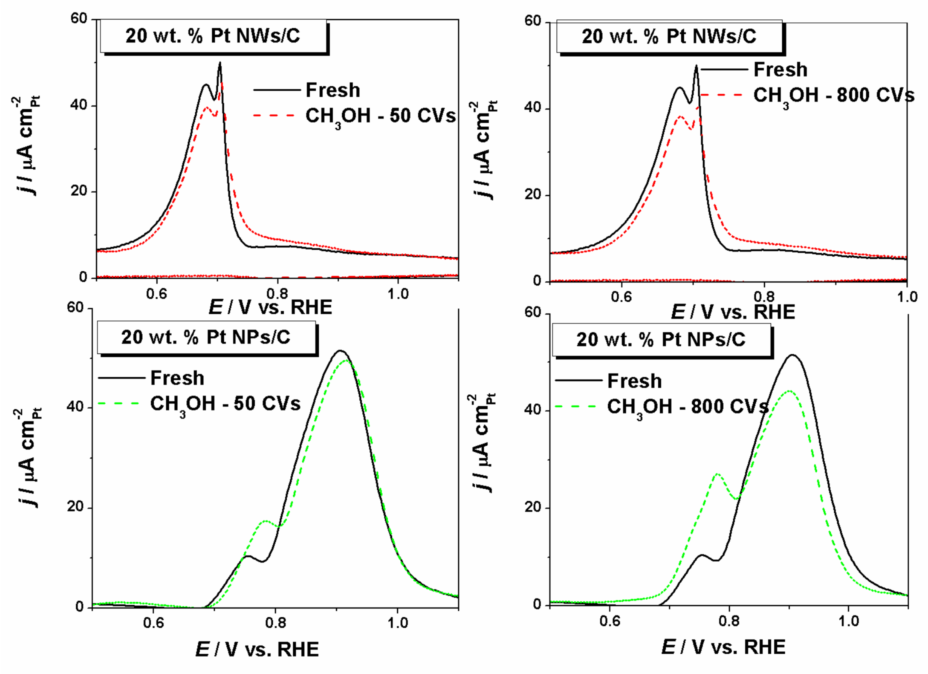

Figure VI-6. Background subtracted CO stripping voltammograms on fresh/aged Pt NWs/C and 20 wt.% Pt NPs/C catalysts after 50 (left) or 800 potential cycles (right) between 0.05 and 1.23 V *vs.* RHE in 0.1 M $HClO_4$ + 0.5 M methanol. $v$ = 0.020 V s$^{-1}$; $T$ = 20 °C.

## 4. Long term ageing treatment

Long-term ageing experiments were also performed to determine the stability of the unsupported Pt NWs, the Pt NWs/C and the benchmark Pt NP/C catalysts (20 wt. % and 40 wt. %). The aging procedure comprised 1000 or 5000 potential cycles between 0.05 V *vs.* RHE to 1.23 V *vs.* RHE in 0.1 M $HClO_4$ at a sweep rate $v = 0.2$ V $s^{-1}$ and $T = 60$ °C. Figure VI-7 shows the CO stripping voltammograms measured on the fresh/aged catalysts. On both Pt/C 20 and 40 wt. %, the charge under the pre-peak increased at the expense of main peak, a feature that is typical of the formation of Pt aggregates. On the contrary, on both carbon-supported and unsupported Pt NWs, the position of the main CO stripping peak remained largely unchanged, and demonstrates the high stability of the synthesized Pt NWs under reducing conditions.

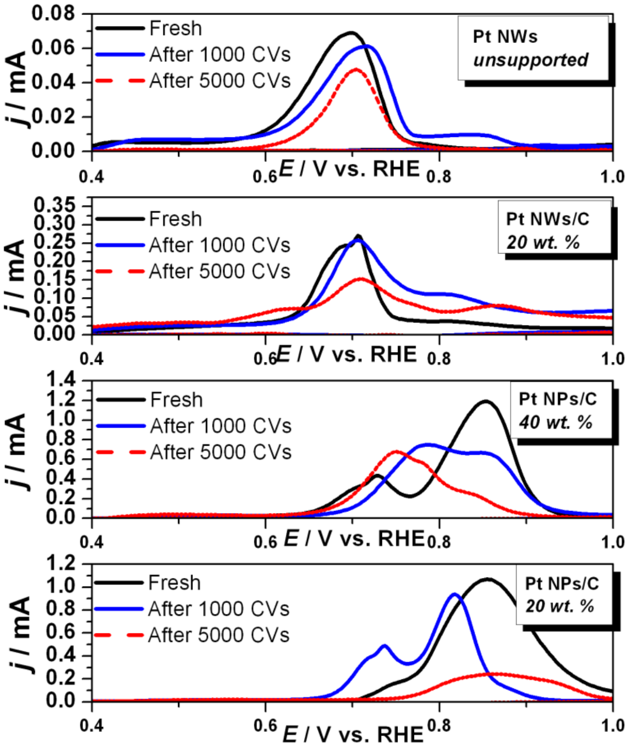

Figure VI-7. Background subtracted CO stripping voltammograms measured on Pt NWs, Pt NWs /C, Pt NPs/C 40 wt. % and Pt NPs/C 20 wt %. The ageing treatments were performed in the 0.1 M $HClO_4$, sweep rate 0.2 V $s^{-1}$. $T = 60$ °C. Electrolyte: 0.1 M $HClO_4$; $v = 0.020$ V $s^{-1}$; $T = 20$ °C.

## C. Electrocatalytic activity of Pt NWs/C for the MOR

Figure VI-8 shows the electrocatalytic activity of Pt NWs/C and Pt NPs/C catalysts for the MOR in 0.1 M $HClO_4$ + 0.5 M MeOH. The currents are normalized to the surface area estimated from the CO stripping coulometry. The current peak ratio of $I_f$ (the forward peak current density) to $I_b$ (the backward peak current density) is used to indicate the CO tolerance of Pt catalysts [36]. The $I_f/I_b$ ratio strongly depends on the potential sweep rate, and is much higher on the Pt NWs/C than on Pt NPs/C. Similar results were recently obtained by Wang *et al.* [33, 36] on PtRu NWs/C. The authors ascribed the enhanced electrocatalytic activity of PtRu NWs/C *vs*. PtRu NPs/C to the high fraction of grain boundaries in these materials and to the unique Pt NWs structure.

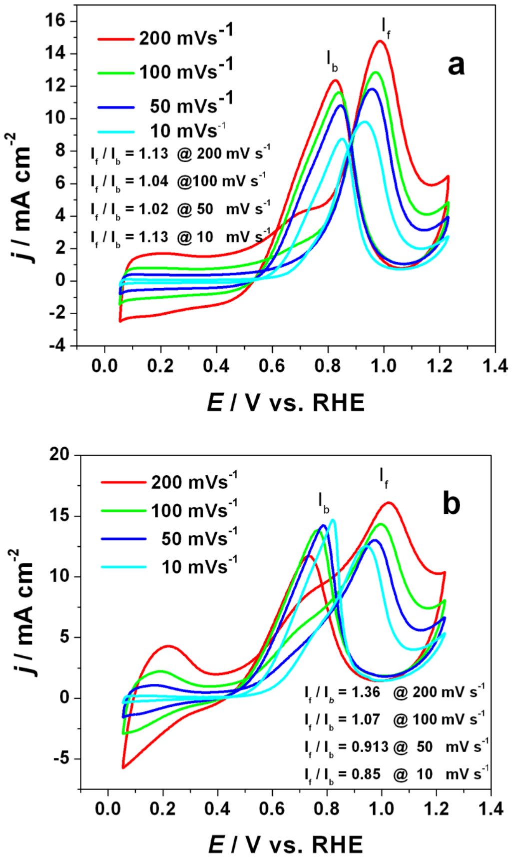

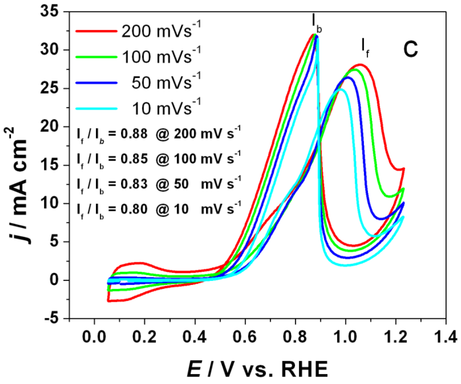

Figure VI-8. Cyclic voltammograms of Pt NWs/C (a), Pt NPs/C 40 wt % (b) and Pt NPs/C 20 wt. % (c) in a 0.1 M $HClO_4$ + 0.5 M MeOH solution at different scan rates of 0.2, 0.1, 0.05 and 0.01V $s^{-1}$. $T$ = 20 °C.

It is generally admitted that the MOR proceeds via a Langmuir-Hinshelwood mechanism in which methanol is adsorbed and dissociated onto the Pt surface, yielding the formation of $CO_{ads}$ in the potential region $E < 0.5$ V *vs*. RHE [45-50]. This step is fast is the main reason for the rapid poisoning of the Pt surface under low electrode potential conditions.

$CH_3OH + Pt \rightarrow Pt(CH_3OH)_{ads}$ Equation VI-3

$Pt(CH_3OH)_{ads} \rightarrow Pt(CO)_{ads} + 4\,H^+ + 4e^-$ Equation VI-3a

$H_2O + Pt \rightarrow Pt(OH)_{ads} + H^+ + e^-$ Equation VI-3b

$Pt(OH)_{ads} + Pt(CO)_{ads} \rightarrow 2\,Pt + CO_2 + H^+ + e^-$ Equation VI-3c

At more positive electrode potentials, $CO_{ads}$ is then oxidized to $CO_2$ (Equation VI-3) via adsorbed oxygenated species ($OH_{ads}$) formed by water splitting. As $CO_{ads}$ is the main intermediate formed during the MOR in DMFCs, the CO tolerance of Pt NWs/C and Pt NPs/C catalysts is important. Figure VI-9 shows the background subtracted CO stripping curves normalized by ECSA. CO oxidation on the Pt NPs/C samples consists of two peaks at $E \sim 0.87$ V *vs*. RHE with variable electrical charges below them as a result of variable degree of aggregation. On Pt NWs/C, the position of the main peak is shifted by ca. 170 mV, indicating much larger tolerance to CO of Pt surface atoms. The latter is believed to consistently account for the observed enhanced MOR kinetics on the 1D material.

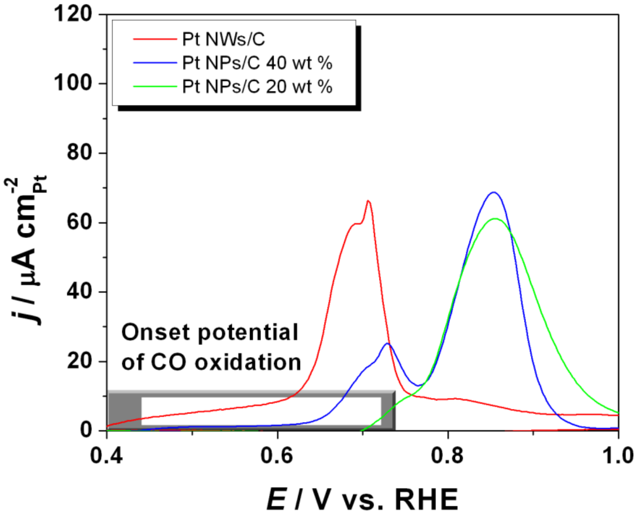

Figure VI-9. Background-subtracted CO stripping voltammograms on Pt NWs /C, Pt NPs/C 20 wt.% Pt NPs/C 40 wt.%. in 0.1 M $HClO_4$, sweep rate 0.02 V $s^{-1}$. Electrolyte: 0.1 M $HClO_4$; *v* = 0.020 V $s^{-1}$; *T* = 20 °C.

## III. Conclusions

In this chapter, Pt NWs with *ca*. 2.0 nm crystallite size were synthesized by a soft template method and benchmarked with Pt NPs/C 20 wt. % E-TeK. The electrocatalytic for the electrooxidation of CO and methanol molecules and the stability in conditions mimicking fuel cell operation of these two materials were investigated. Evidences were provided that the morphology of the Pt material plays a pivotal role: the 1D Pt NWs/C demonstrate a reduction by *ca*. 170 mV of the CO oxidation overpotential and feature high and stable MOR activity. The latter was bridged with HRTEM images showing that the Pt nanowires possess smooth crystal planes that are connected by grain boundaries. XRD experiments also evidence preferential texture of the Pt NWs with a high fraction of high-index crystal planes. The enhanced durability of Pt NWs/C was rationalized by considering (i) the increase of the weight of the Pt nanomaterials resulting from the increase of the morphology size (nanoparticles to nanowires) and (ii) the enhanced contact surface area between the Pt NWs and the carbon support. The development of 1D Pt nanostructures, such as Pt NWs, hold promises to solve the durability issues faced with the 0D materials actually used in a PEMFCs.

# CHAPTER VII – GENERAL CONCLUSION AND OUTLOOK

State-of-the-art catalytic layers of PEMFCs utilize ionomer-bonded Pt-based nanocrystallites supported on a porous carbon support to accelerate the rate of the hydrogen oxidation reaction at the anode, and the oxygen reduction reaction at the cathode. Post-mortem analysis of PEMFC catalytic layers revealed that four degradation mechanisms yield Pt surface area losses (and hence decreased PEMFC performance): (i) aggregation and/or detachment of the metal nanoparticles, (ii) corrosion of the high surface area carbon support, (iii) Ostwald ripening (dissolution/redeposition of the Pt-based crystallites) yielding the formation of $Pt^{z+}$ species and (iv) chemical reduction of the $Pt^{z+}$ species in ion conductors, yielding the formation of electrically disconnected Pt crystallites. Evidences were provided in this manuscript that the first three degradation mechanisms take place simultaneously, and interact with each other in a model PEMFC environment. The second key result of this Ph.D. is that the contribution of each degradation mechanism to the loss of electrochemically active Pt surface area depends on the nature of the gaseous atmosphere and on the potential range used in the accelerated aging test.

A major concern of the PhD was to be able to isolate a well-known yet poorly explored degradation mechanism: the migration of the Pt nanocrystallites. For that purpose, commercial Pt/Vulcan XC 72 electrocatalysts were aged in “mild” conditions, for which the corrosion of both the Pt nanoparticles and the carbon support could not be considered dominant. The materials were characterized by electron microscopy and electrochemical techniques in the fresh state and after various aging conditions. Evidences were provided that the Pt/C nanoparticles are not immobile but prone to aggregate in the presence of $H_2$, $CH_3OH$, and CO, three molecules of interest for PEMFC applications. The migration rate of the Pt crystallites was the largest in CO-containing solution and decreased in the order CO > $CH_3OH$ > $H_2$. Based on thermodynamic considerations, we suggested that chemisorption modifies the surface tension of Pt, and lowered the work of adhesion between the Pt nanoparticles and the high surface area carbon support. The possible interactions between the oxygen-containing groups of the carbon support and the Pt nanoparticles were also underlined, and will be further explored in the Ph.D. of Luis Castanheira.

In Chapter IV of the Ph.D., we provided some insights into the mechanism of the electrochemical oxidation of Vulcan XC72, a carbon black support classically used in PEMFC catalytic layers. Raman spectroscopy measurements evidenced that the disordered domains of the Vulcan XC72 support (non-graphitic, $sp^3$-hybridized) are preferentially oxidized in experimental conditions mimicking the operation of a PEMFC. The ordered domains (graphitic carbon, $sp^2$-hybridized) of the Vulcan XC72 support are also oxidized but at a much smaller rate than that observed on the non-graphitic domains. The preferential oxidation of the disordered domains of Vulcan XC72 translates in XPS by a concomitant decrease of the content of oxygen-containing carbon surface groups. A major consequence of the oxidation of the high-surface area carbon support is the aggregation and the detachment of the supported Pt nanoparticles. Here again, the role of the oxygen-containing carbon surface groups, which are reaction intermediates in the carbon oxidation reaction, requires clarification. It is of prime importance to determine (i) whether the kinetics of corrosion of the carbon support depends on the nature and the content of oxygenated groups that are initially present on the surface but also (ii) if these oxygenated groups are the same as those formed during the corrosion reaction. Future work in this direction requires the coupling of electrochemical, chemical and physical techniques such as Fourier-Transform infrared spectroscopy, mass spectroscopy and identical location transmission electron microscopy.

In Chapter V, we used model Pt/Sibunit electrocatalysts to show that aged catalytic layers featuring (i) low Pt to C weight fraction, (ii) large Pt crystallite size and (iii) large inter-particle distance, perform worst for the ORR. Evidences were provided that the ORR follows the series 2 + 2 $e^-$ pathway with $H_2O_2$ as the major reaction intermediate. The fraction of $H_2O_2$ molecules escaping from the catalytic layer, and being detected at the ring in RRDE experiments highly depends on the Pt to C surface coverage and of the thickness of the catalytic layer. Consequently, the average number of transferred electrons produced during the ORR decreases below 4 with the decrease of the catalyst layer thickness or the Pt loading. This is rationalized by considering the lower probability for $H_2O_2$ molecules to be re-adsorbed and further reduced into water in the catalytic layer. We also found that Pt/Sibunit electrocatalysts face similar degradation mechanisms as Pt/Vulcan XC 72 used in

Chapter III. Repetitive potential cycles in CO-containing electrolyte facilitated the migration and aggregation of Pt nanoparticles. Similarly, we observed that repetitive potential cycles in $O_2$-containing electrolyte cause a decrease of the density of isolated Pt nanoparticles. It is believed that the large production of $H_2O_2$ molecules cause enhanced rate of carbon corrosion and detachment of the Pt nanoparticles.

Finally, Pt NWs with 2.1 ± 0.2 nm crystallite size were synthesized by a soft template method and benchmarked with Pt NPs/C 20 wt. % E-TeK. The electrocatalytic for the electrooxidation of CO and methanol molecules and the stability in conditions mimicking fuel cell operation of these two materials were investigated. Evidences were provided that the morphology of the Pt material plays a pivotal role: the 1D Pt NWs/C demonstrate a reduction by *ca*. 170 mV of the CO oxidation overpotential and feature high and stable MOR activity. The latter was bridged with HRTEM images showing that the Pt nanowires possess smooth crystal planes that are connected by grain boundaries. XRD experiments also evidenced preferential texture of the Pt NWs with a high fraction of high-index crystal planes. The enhanced durability of Pt NWs/C was rationalized by considering (i) the increase of the weight of the Pt nanomaterials resulting from the increase of the morphology size (nanoparticles to nanowires) and (ii) the enhanced contact surface area between the Pt NWs and the carbon support. The development of 1D Pt nanostructures, such as Pt NWs, hold promises to solve the durability issues faced with the 0D materials actually used in a PEMFCs.

The next generation of catalytic materials should be capable of fulfilling simultaneously cost, performance, and durability requirements of PEMFC applications. Evidences were provided in this manuscript that the stability of PEMFC electrocatalysts may be largely enhanced by designing adequately their nanostructure. In addition, it is now well-established that bimetallic alloyed Pt-M/C surfaces (M being a transition metal) exhibit an improved catalytic performance for the ORR relative to Pt, both in terms of mass activity (per g of Pt) or specific activity (per real $cm^2$ of Pt). Therefore, Pt-M nanowires, Pt-M capsules and Pt-M nanonetwork appear to be interesting materials, which combine positive effects in ORR electrocatalysis and long-term stability. Using such catalytic materials will impose to pay a high price for PEMFC catalytic layers, but it is the opinion of the author that high mass activity and durable performance cannot be met with the conventional nanometre-sized crystallites. $Pt_xCo_y$ nanowires supported on Vulcan XC72 were recently synthesized in our lab using the methodology exposed in Chapter VI. However, due to time constraints and limited access to characterization techniques, only preliminary results were obtained and couldn't be presented in this manuscript.

# REFERENCES

## Chapter I

[1] Exxonmobil. *The outlook for Energy: A View to 2040* 2012. Available from https://www.exxonmobil.com/Corporate/files/news_pub_eo.pdf.

[2] U.S.D.o. Energy. 2012. *Basic Research Needs for the Hydrogen Economy, Report on the Basic Energy Sciences Workshop on Hydrogen Production, Storage, and Use* 2003 [cited September 11th 2012]. Available from http://science.energy.gov/bes/news-and-resources/reports/basic-research-needs/.

[3] E.A. Heaton, S.P. Long, T.B. Voigt, M.B. Jones, J. Clifton-Brown, Mitig. Adapt. Strat. Glob. Change, 9 (2004) 433-451.

[4] P. Pinel, C.A. Cruickshank, I. Beausoleil-Morrison, A. Wills, Renewable Sustainable Energy Rev., 15 (2011) 3341-3359.

[5] E. Sesto, C. Casale, J. Wind Eng. Ind. Aerodyn., 74-76 (1998) 375-387.

[6] D.R. Lide, in CRC Handbook of Chemistry and Physics, 84th ed., CRC Press, 2003-2004.

[7] H.A. Gasteiger, W. Vielstich, H. Yokokawa, Handbook of fuel cells, John Wiley & Sons Ltd, Chichester, 2009.

[8] G. Wand. 2012. *Fuel cell history* 2006 [cited September 11th 2012]. Available from http://www.fuelcelltoday.com.

[9] P. Ochal, J.L. Gomez de la Fuente, M. Tsypkin, F. Seland, S. Sunde, N. Muthuswamy, M. Rønning, D. Chen, S. Garcia, S. Alayoglu, B. Eichhorn, J. Electroanal. Chem., 655 (2011) 140-146.

[10] W.R. Grove, London and Edinburgh Philosophical Magazine and Journal of Science, 21 (1842) 417-420.

[11] H.A. Gasteiger, S.S. Kocha, B. Sompalli, F.T. Wagner, Appl. Catal. B, 56 (2005) 9-35.

[12] H.A. Gasteiger, N.M. Markovic, Science, 324 (2009) 48-49.

[13] Y. Wang, K.S. Chen, J. Mishler, S.C. Cho, X.C. Adroher, Appl. Energ., 88 (2011) 981-1007.

[14] L. Zhang, J. Zhang, D.P. Wilkinson, H. Wang, J. Power Sources, 156 (2006) 171-182.

[15] R. Bashyam, P. Zelenay, Nature, 443 (2006) 63-66.

[16] C.W.B. Bezerra, L. Zhang, K. Lee, H. Liu, A.a.L.B. Marques, E.P. Marques, H. Wang, J. Zhang, Electrochim. Acta, 53 (2008) 4937-4951

[17] R.W. Reeve, P.A. Christensen, A.J. Dickinson, A. Hamnett, K. Scott, Electrochim. Acta, 45 (2000) 4237-4250.

[18] H.A. Gasteiger, J.E. Panels, S.G. Yan, J. Power Sources, 127 (2004) 162-171.

[19] A.J.J. Kadjo, P. Brault, A. Caillard, C. Coutanceau, J.P. Garnier, S. Martemianov, J. Power Sources, 172 (2007) 613-622.

[20] M. Cavarroc, A. Ennadjaoui, M. Mougenot, P. Brault, R. Escalier, Y. Tessier, J. Durand, S. RouauldÃ¨s, T. Sauvage, C. Coutanceau, Electrochem. Com., 11 (2009) 859-861.

[21] A. Caillard, C. Charles, R. Boswell, P. Brault, C. Coutanceau, Appl. Phys. Lett., 90 (2007) 3.

[22] E. Billy, F. Maillard, A. Morin, L. Guétaz, F. Emmieux, C. Thurier, P. Doppelt, S. Donet, S. Mailley, J. Power Sources, 195 (2010) 2737–2746.

[23] F. Maillard, S. Pronkin, E.R. Savinova, Influence of size on the electrocatalytic activities of supported metal nanoparticles in fuel cells related reactions, in: Handbook of Fuel Cells, John Wiley & Sons, Ltd, 2009.

[24] S. Mukerjee, S. Srinivasan, J. Electroanal. Chem., 357 (1993) 201-224.

[25] H.A. Gasteiger, N. Markovic, P.N. Ross, E.J. Cairns, J. Phys. Chem., 97 (1993) 12020-12029.

[26] E. Antolini, E.R. Gonzalez, Electrochim. Acta, 56 (2010) 1-14.

[27] H. Zhao, J. Yang, L. Li, H. Li, J. Wang, Y. Zhang, Int. J. Hydrogen Energy, 34 (2009) 3908-3914.

[28] C. Xu, L. Cheng, P. Shen, Y. Liu, Electrochem. Com., 9 (2007) 997-1001.

[29] R. Borup, J. Meyers, B. Pivovar, Y.S. Kim, R. Mukundan, N. Garland, D. Myers, M. Wilson, F. Garzon, D. Wood, P. Zelenay, K. More, K. Stroh, T. Zawodzinski, J. Boncella, J.E. McGrath, M. Inaba, K. Miyatake, M. Hori, K. Ota, Z. Ogumi, S. Miyata, A. Nishikata, Z. Siroma, Y. Uchimoto, K. Yasuda, K.I. Kimijima, N. Iwashita, Chem. Rev., 107 (2007) 3904-3951.

[30] S. Chen, H.A. Gasteiger, K. Hayakawa, T. Tada, Y. Shao-Horn, J. Electrochem. Soc., 157 (2010) A82-A97.

[31] L. Dubau, J. Durst, L. Guetaz, F. Maillard, M. Chatenet, J. Andre, E. Rossinot, ECS Trans., 41 (2011) 827-836.

[32] L. Dubau, J. Durst, L. Guétaz, F. Maillard, M. Chatenet, J. André, E. Rossinot, ECS Electrochem. Lett., 1 (2012) F13-F15.

[33] L. Dubau, J. Durst, F. Maillard, M. Chatenet, L. Guétaz, J. André, E. Rossinot, Electrochim. Acta, 56 (2011) 10658-10667.

[34] L. Dubau, J. Durst, F. Maillard, M. Chatenet, L. Guétaz, J. André, E. Rossinot, Fuel Cells, 12 (2012) 188-198.

[35] L. Dubau, F. Maillard, M. Chatenet, J. André, E. Rossinot, Electrochim. Acta, 56 (2010) 776-783.

[36] L. Dubau, F. Maillard, M. Chatenet, L. Guétaz, J. André, E. Rossinot, J. Electrochem. Soc., 157 (2010) B1887-B1895.

[37] Z. Zhao, X. Fang, Y. Li, Y. Wang, P.K. Shen, F. Xie, X. Zhang, Electrochem. Com., 11 (2009) 290-293.

[38] E. Guilminot, A. Corcella, C. Iojoiu, G. Berthomé, F. Maillard, M. Chatenet, J.-Y. Sanchez, J. Electrochem. Soc., 154 (2007) B1106-B1114.

[39] V. Mehta, J.S. Cooper, J. Power Sources, 114 (2003) 32-53.

[40] F. de Bruijn, Green Chem., 7 (2005) 132-150.

[41] D.J.L. Brett, N.P. Brandon, J. Fuel Cell Sci. Tech., 4 (2007) 29-44.

[42] A. Pozio, R.F. Silva, M. De Francesco, L. Giorgi, Electrochim. Acta, 48 (2003) 1543-1549.

[43] J. Wu, X.Z. Yuan, J.J. Martin, H. Wang, J. Zhang, J. Shen, S. Wu, W. Merida, J. Power Sources, 184 (2008) 104-119.

[44] H.-K. Lee, J.-H. Park, D.-Y. Kim, T.-H. Lee, J. Power Sources, 131 (2004) 200-206.

[45] G.-G. Park, Y.-J. Sohn, T.-H. Yang, Y.-G. Yoon, W.-Y. Lee, C.-S. Kim, J. Power Sources, 131 (2004) 182-187.

[46] M. Prasanna, H.Y. Ha, E.A. Cho, S.A. Hong, I.H. Oh, J. Power Sources, 131 (2004) 147-154.

[47] C. Lee, W. MÃ©rida, J. Power Sources, 164 (2007) 141-153.

[48] D.A. Stevens, M.T. Hicks, G.M. Haugen, J.R. Dahn, J. Electrochem. Soc., 152 (2005) A2309-A2315.

[49] M. Cai, M.S. Ruthkosky, B. Merzougui, S. Swathirajan, M.P. Balogh, S.H. Oh, J. Power Sources, 160 (2006) 977-986.

[50] M. Schulze, N. Wagner, T. Kaz, K.A. Friedrich, Electrochim. Acta, 52 (2007) 2328-2336.

[51] L.R. Jordan, A.K. Shukla, T. Behrsing, N.R. Avery, B.C. Muddle, M. Forsyth, J. Power Sources, 86 (2000) 250-254.

[52] U. Pasaogullari, C.-Y. Wang, Electrochim. Acta, 49 (2004) 4359-4369.

[53] A.Z. Weber, J. Newman, J. Electrochem. Soc., 152 (2005) A677-A688.

[54] F. Maillard, A. Bonnefont, F. Micoud, Electrochem. Com., 13 (2011) 1109-1111.

[55] W. Schmittinger, A. Vahidi, J. Power Sources, 180 (2008) 1-14.

[56] M. Chatenet, L. Guétaz, F. Maillard, Electron microscopy to study membrane electrode assembly (MEA) materials and structure degradation, in: W. Vielstich, H.A. Gasteiger, H. Yokokawa (Eds.) Handbook of fuel cells - Fundamentals, technology and applications, John Wiley & Sons, Inc., New York, 2009, pp. 844-860.

[57] J. Xie, D.L. Wood, D.M. Wayne, T.A. Zawodzinski, P. Atanassov, R.L. Borup, J. Electrochem. Soc., 152 (2005) A104-A113.

[58] V.A. Sethuraman, J.W. Weidner, A.T. Haug, M. Pemberton, L.V. Protsailo, Electrochim. Acta, 54 (2009) 5571-5582.

[59] J. Xie, D.L. Wood, Iii, K.L. More, P. Atanassov, R.L. Borup, J. Electrochem. Soc., 152 (2005) A1011-A1020.

[60] S. Zhang, X.-Z. Yuan, J.N.C. Hin, H. Wang, K.A. Friedrich, M. Schulze, J. Power Sources, 194 (2009) 588-600.

[61] E. Antolini, Mater. Chem. Phys., 78 (2003) 563-573.

[62] X. Yu, S. Ye, J. Power Sources, 172 (2007) 133-144.

[63] E. Antolini, J.R.C. Salgado, E.R. Gonzalez, J. Power Sources, 160 (2006) 957-968.

[64] Y. Shao, G. Yin, Y. Gao, J. Power Sources, 171 (2007) 558-566.

[65] S. Zhang, X. Yuan, H. Wang, W. MÃ©rida, H. Zhu, J. Shen, S. Wu, J. Zhang, Int. J. Hydrogen Energy, 34 (2009) 388-404.

[66] P. Rama, R. Chen, J. Andrews, Proc. Inst. Mech. Eng., Part A: J. Power Energy Syst, 222 (2008) 421-441.

[67] E. Guilminot, A. Corcella, F. Charlot, F. Maillard, M. Chatenet, J. Electrochem. Soc., 154 (2007) B96-B105.

[68] K.J.J. Mayrhofer, J.C. Meier, S.J. Ashton, G.K.H. Wiberg, F. Kraus, M. Hanzlik, M. Arenz, Electrochem. Com., 10 (2008) 1144-1147.

[69] J.C. Meier, C. Galeano, I. Katsounaros, A.A. Topalov, A. Kostka, F. Schüth, K.J.J. Mayrhofer, ACS Catal., 2 (2012) 832-843.

[70] T. Yoda, H. Uchida, M. Watanabe, Electrochim. Acta, 52 (2007) 5997-6005.

[71] Z. Zhao, L. Dubau, F. Maillard, J. Power Sources, 217 (2012) 449-458.

[72] S. Maass, F. Finsterwalder, G. Frank, R. Hartmann, C. Merten, J. Power Sources, 176 (2008) 444-451.

[73] Z.Y. Liu, J.L. Zhang, P.T. Yu, J.X. Zhang, R. Makharia, K.L. More, E.A. Stach, J. Electrochem. Soc., 157 (2010) B906-B913.

[74] N. Linse, L. Gubler, G.G. Scherer, A. Wokaun, Electrochim. Acta, 56 (2011) 7541-7549.

[75] Y. Shao-Horn, W. Sheng, S. Chen, P. Ferreira, E. Holby, D. Morgan, Topics Catal., 46 (2007) 285-305.

[76] P.J. Ferreira, G.J. la O', Y. Shao-Horn, D. Morgan, R. Makharia, S. Kocha, H.A. Gasteiger, J. Electrochem. Soc., 152 (2005) A2256-A2271.

[77] X. Wang, R. Kumar, D.J. Myers, Electrochem. Solid-State Lett., 9 (2006).

[78] S. Mitsushima, S. Kawahara, K.I. Ota, N. Kamiya, J. Electrochem. Soc., 154 (2007) B153-B158.

[79] Z. Nagy, H. You, Electrochim. Acta, 47 (2002) 3037-3055.

[80] B.J. Eastwood, P.A. Christensen, R.D. Armstrong, N.R. Bates, J. Solid State Electrochem., 3 (1999) 179-186.

[81] J. Willsau, J. Heitbaum, Journal of Electroanalytical Chemistry and Interfacial Electrochemistry, 161 (1984) 93-101.

[82] Y. Shao, G. Yin, Y. Gao, P. Shi, J. Electrochem. Soc., 153 (2006) A1093-A1097.

[83] K.H. Kangasniemi, D.A. Condit, T.D. Jarvi, J. Electrochem. Soc., 151 (2004) E125-E132.

[84] J. Willsau, J. Heitbaum, J. Electroanal. Chem., 161 (1984) 93-101.

[85] L.M. Roen, C.H. Paik, T.D. Jarvi, Electrochem. Solid-State Lett., 7 (2004) A19-A22.

[86] F. Coloma, A. Sepulvedaescribano, F. Rodriguezreinoso, J. Catal., 154 (1995) 299-305.

[87] K. Kinoshita, Carbon, electrochemical and physicochemical properties, John Wiley & Sons, New York, 1988.

[88] J. Chen, K.-Y. Chan, Mol. Simul., 31 (2005) 527 - 533.

[89] X. Wang, W. Li, Z. Chen, M. Waje, Y. Yan, Journal of Power Sources, 158 (2006) 154-159.

[90] E.S. Steigerwalt, G.A. Deluga, C.M. Lukehart, J. Phys. Chem. B, 106 (2002) 760-766.

[91] C. Wang, M. Waje, X. Wang, J.M. Tang, R.C. Haddon, Yan, Nano Lett., 4 (2003) 345-348.

[92] J.M. Tang, K. Jensen, M. Waje, W. Li, P. Larsen, K. Pauley, Z. Chen, P. Ramesh, M.E. Itkis, Y. Yan, R.C. Haddon, J. Phys. Chem. C, 111 (2007) 17901-17904.

[93] X. Wang, M. Waje, Y. Yan, Electrochem. Solid-State Lett., 8 (2005) A42-A44.

[94] P. Ehrburger, O.P. Mahajan, P.L. Walker Jr, J. Catal., 43 (1976) 61-67.

[95] D.R. Lowde, J.O. Williams, P.A. Attwood, R.J. Bird, B.D. McNicol, R.T. Short, Journal of the Chemical Society-Faraday Transactions I, 75 (1979) 2312-&.

[96] C. Prado-Burguete, A. Linares-Solano, F. Rodriguez-Reinoso, C.S.-M. de Lecea, J. Catal., 115 (1989) 98-106.

[97] P.L. Antonucci, V. Alderucci, N. Giordano, D.L. Cocke, H. Kim, J. Appl. Electrochem., 24 (1994) 58-65.

[98] S. Adora, Y. Soldo-Olivier, R. Faure, R. Durand, E. Dartyge, F. Baudelet, J. Phys. Chem. B, 105 (2001) 10489-10495.

[99] F. Coloma, A. Sepulveda-Escribano, J.L.G. Fierro, F. Rodriguez-Reinoso, Langmuir, 10 (1994) 750-755.

[100] S.R. de Miguel, O.A. Scelza, M.C. Roman-Martinez, C. Salinas-Martinez de Lecea, D. Cazorla-Amoros, A. Linares-Solano, Appl. Catal. A, 170 (1998) 93-103.

[101] A. Guerrero-Ruiz, P. Badenes, I. Rodŕiguez-Ramos, Appl. Catal. A, 173 (1998) 313-321.

[102] M.C. Roman-Martinez, D. Cazorla-Amoros, A. Linares-Solano, C.S.-M. De Lecea, H. Yamashita, M. Anpo, Carbon, 33 (1995) 3-13.

[103] G.C. Torres, E.L. Jablonski, G.T. Baronetti, A.A. Castro, S.R. de Miguel, O.A. Scelza, M.D. Blanco, M.A. Penã Jiménez, J.L.G. Fierro, Appl. Catal. A, 161 (1997) 213-226.

[104] L.J. Hillenbrand, J.W. Lacksonen, J. Electrochem. Soc., 112 (1965) 249-252.

[105] A.K. Shukla, A. Hamnett, A. Roy, S.R. Barman, D.D. Sarma, V. Alderucci, L. Pino, N. Giordano, J. Electroanal. Chem., 352 (1993) 337-343.

[106] A.K. Shukla, M.K. Ravikumar, A. Roy, S.R. Barman, D.D. Sarma, A.S. Arico, V. Antonucci, L. Pino, N. Giordano, J. Electrochem. Soc., 141 (1994) 1517-1522.

[107] V. Alderucci, L. Pino, P.L. Antonucci, W. Roh, J. Cho, H. Kim, D.L. Cocke, V. Antonucci, Mater. Chem. Phys., 41 (1995) 9-14.

[108] F. Coloma, A. Sepulveda-Escribano, J.L.G. Fierro, F. Rodriguez-Reinoso, Appl. Catal. A, 148 (1996) 63-80.

[109] R.V. Hull, L. Li, Y.C. Xing, C.C. Chusuei, Chem. Mater., 18 (2006) 1780-1788.

[110] J. Petroski, M.A. El-Sayed, The Journal of Physical Chemistry A, 107 (2003) 8371-8375.

[111] J. Escard, C. Leclère, J.P. Contour, J. Catal., 29 (1973) 31-39.

[112] Y.R. Tzeng, W.W. Pai, C.S. Tsao, M.S. Yu, J. Phys. Chem. C, 115 (2011) 12023-12032.

[113] W.M. Chen, B.D. Qu, Int. J. Hydrogen Energy, 35 (2010) 10102-10108.

[114] K. Kinoshita, J.A.S. Bett, Carbon, 12 (1974) 525-533.

[115] C.C. Hung, P.Y. Lim, J.R. Chen, H.C. Shih, J. Power Sources, 196 (2011) 140-146.

[116] N. Giordano, P.L. Antonucci, E. Passalacqua, L. Pino, A.S. Arico, K. Kinoshita, Electrochim. Acta, 36 (1991) 1931-1935.

[117] K. Kinoshita, J. Bett, Carbon, 11 (1973) 237-247.

[118] M.S. Wilson, F.H. Garzon, K.E. Sickafus, S. Gottesfeld, J. Electrochem. Soc., 140 (1993) 2872-2877.

[119] P. Scardi, P.L. Antonucci, J. Mater. Res., 8 (1993) 1829-1835.

[120] I.N. Leontyev, V.E. Guterman, E.B. Pakhomova, P.E. Timoshenko, A.V.Guterman, I.N. Zakharchenko, G.P. Petin, B. Dkhil, J. Alloys Compd., 500 (2010) 241-246.

[121] K.J.J. Mayrhofer, S.J. Ashton, J.C. Meier, G.K.H. Wiberg, M. Hanzlik, M. Arenz, J. Power Sources, 185 (2008) 734-739.

[122] F.J. Perez-Alonso, C.F. Elkjaer, S.S. Shim, B.L. Abrams, I.E.L. Stephens, I. Chorkendorff, J. Power Sources, 196 (2011) 6085-6091.

[123] T.J. Schmidt, H.A. Gasteiger, G.D. Stab, P.M. Urban, D.M. Kolb, R.J. Behm, J. Electrochem. Soc., 145 (1998) 2354-2358.

[124] R. Van Hardeveld, F. Hartog, Surf Sci, 15 (1969) 189-230.

[125] S. Trasatti, O.A. Petrii, J. Electroanal. Chem., 327 (1992) 353-376.

[126] F. Maillard, M. Eikerling, O.V. Cherstiouk, S. Schreier, E. Savinova, U. Stimming, Faraday Discuss., 125 (2004) 357-377.

[127] O.V. Cherstiouk, P.A. Simonov, E.R. Savinova, Electrochim. Acta, 48 (2003) 3851-3860.

[128] F. Maillard, S. Schreier, M. Hanzlik, E.R. Savinova, S. Weinkauf, U. Stimming, Phys. Chem. Chem. Phys., 7 (2005) 385-393.

[129] F. Maillard, E. Savinova, P.A. Simonov, V.I. Zaikovskii, U. Stimming, J. Phys. Chem. B, 108 (2004) 17893-17904.

[130] M. Arenz, K.J.J. Mayrhofer, V. Stamenkovic, B.B. Blizanac, T. Tomoyuki, P.N. Ross, N.M. Markovic, J. Am. Chem. Soc., 127 (2005) 6819-6829.

[131] K.J.J. Mayrhofer, M. Arenz, B.B. Blizanac, V.R. Stamenkovic, P.N. Ross, N.M. Markovic, Electrochim. Acta, 50 (2005) 5144-5154.

[132] X. Li, X. Qiu, H. Yuan, L. Chen, W. Zhu, J. Power Sources, 184 (2008) 353-360.

[133] E.G. Ciapina, S.F. Santos, E.R. Gonzalez, J. Electroanal. Chem., 644 (2010) 132-143.

[134] A. Lopez-Cudero, J. Solla-Gullon, E. Herrero, A. Aldaz, J.M. Feliu, J. Electroanal. Chem., 644 (2010) 117-126.

[135] B. Andreaus, M. Eikerling, J. Electroanal. Chem., 607 (2007) 121-132.

[136] B. Andreaus, F. Maillard, J. Kocylo, E.R. Savinova, M. Eikerling, J. Phys. Chem. B, 110 (2006) 21028-21040.

## Chapter II

[1] Y. Yermakov, V. Surovikin, G. Plaksin, V. Semikolenov, V. Likholobov, L. Chuvilin, S. Bogdanov, React. Kinet. Catal. Lett., 33 (1987) 435-440.

[2] F. Maillard, E. Savinova, P.A. Simonov, V.I. Zaikovskii, U. Stimming, J. Phys. Chem. B, 108 (2004) 17893-17904.

[3] J.-B. Donnet, A. Voet, Carbon black: physics, chemistry and elastomer reinforcement, Marcel Dekker, New York, 1976.

[4] Y. Song, R.M. Garcia, R.M. Dorin, H. Wang, Y. Qiu, E.N. Coker, W.A. Steen, J.E. Miller, J.A. Shelnutt, Nano Lett., 7 (2007) 3650-3655.

[5] K.J.J. Mayrhofer, J.C. Meier, S.J. Ashton, G.K.H. Wiberg, F. Kraus, M. Hanzlik, M. Arenz, Electrochem. Com., 10 (2008) 1144-1147.

[6] K.J.J. Mayrhofer, S.J. Ashton, J.C. Meier, G.K.H. Wiberg, M. Hanzlik, M. Arenz, J. Power Sources, 185 (2008) 734-739.

[7] B. Vion-Dury, M. Chatenet, L. Guétaz, F. Maillard, ECS Trans., 41 (2011) 697-708.

[8] H.P. Klug, L.E. Alexander, in, Wiley New York, 1974, pp. 175.

[9] M. Chatenet, L. Guétaz, F. Maillard, Electron microscopy to study membrane electrode assembly (MEA) materials and structure degradation, in: W. Vielstich, H.A. Gasteiger, H. Yokokawa (Eds.) Handbook of fuel cells - Fundamentals, technology and applications, John Wiley & Sons, Inc., New York, 2009, pp. 844-860.

[10] F. Maillard, A. Bonnefont, F. Micoud, Electrochem. Com., 13 (2011) 1109-1111.

[11] A.J. Bard, L.R. Faulkner, Electrochemical methods, John Wiley & Sons, Inc., Weinheim, 2001.

[12] E. Billy, F. Maillard, A. Morin, L. Guétaz, F. Emmieux, C. Thurier, P. Doppelt, S. Donet, S. Mailley, J. Power Sources, 195 (2010) 2737–2746.

[13] O. Antoine, R. Durand, J. Appl. Electrochem., 30 (2000) 839-844.

## Chapter III

[1] K. Kinoshita, Carbon, electrochemical and physicochemical properties, John Wiley & Sons, New York, 1988.

[2] F. Maillard, P. Simonov, E.R. Savinova, Carbon materials as support for fuel cells electrocatalysts, in: P. Serp, J.L. Figueiredo (Eds.) Carbon Materials for Catalysis, John Wiley & Sons, Inc., New York, 2009, pp. 429-480.

[3] L. Dubau, F. Maillard, M. Chatenet, L. Guétaz, J. André, E. Rossinot, J. Electrochem. Soc., 157 (2010) B1887-B1895.

[4] L. Dubau, J. Durst, F. Maillard, M. Chatenet, L. Guétaz, J. André, E. Rossinot, Electrochim. Acta, 56 (2011) 10658-10667.

[5] E. Guilminot, A. Corcella, F. Charlot, F. Maillard, M. Chatenet, J. Electrochem. Soc., 154 (2007) B96-B105.

[6] L.M. Roen, C.H. Paik, T.D. Jarvi, Electrochem. Solid-State Lett., 7 (2004) A19-A22.

[7] Y. Shao-Horn, W. Sheng, S. Chen, P. Ferreira, E. Holby, D. Morgan, Topics Catal., 46 (2007) 285-305.

[8] J.A. Bett, K. Kinoshita, P. Stonehart, J. Catal., 35 (1974) 307-316.

[9] J.A.S. Bett, K. Kinoshita, P. Stonehart, J. Catal., 41 (1976) 124-133.

[10] E. Ruckenstein, B. Pulvermacher, J. Catal., 29 (1973) 224-245.

[11] P.J. Ferreira, G.J. la O', Y. Shao-Horn, D. Morgan, R. Makharia, S. Kocha, H.A. Gasteiger, J. Electrochem. Soc., 152 (2005) A2256-A2271.

[12] E. Guilminot, A. Corcella, C. Iojoiu, G. Berthomé, F. Maillard, M. Chatenet, J.-Y. Sanchez, J. Electrochem. Soc., 154 (2007) B1106-B1114.

[13] M.S. Wilson, F.H. Garzon, K.E. Sickafus, S. Gottesfeld, J. Electrochem. Soc., 140 (1993) 2872-2877.

[14] P. Ehrburger, O.P. Mahajan, P.L. Walker Jr, J. Catal., 43 (1976) 61-67.

[15] D.R. Lowde, J.O. Williams, P.A. Attwood, R.J. Bird, B.D. McNicol, R.T. Short, J. Chem. Soc. Faraday Trans., 75 (1979) 2312-&.

[16] C. Prado-Burguete, A. Linares-Solano, F. Rodriguez-Reinoso, C.S.-M. de Lecea, J. Catal., 115 (1989) 98-106.

[17] P.L. Antonucci, V. Alderucci, N. Giordano, D.L. Cocke, H. Kim, J. Appl. Electrochem., 24 (1994) 58-65.

[18] S. Adora, Y. Soldo-Olivier, R. Faure, R. Durand, E. Dartyge, F. Baudelet, J. Phys. Chem. B, 105 (2001) 10489-10495.

[19] F. Coloma, A. Sepulveda-Escribano, J.L.G. Fierro, F. Rodriguez-Reinoso, Langmuir, 10 (1994) 750-755.

[20] S.R. de Miguel, O.A. Scelza, M.C. Roman-Martinez, C. Salinas-Martinez de Lecea, D. Cazorla-Amoros, A. Linares-Solano, Appl. Catal. A, 170 (1998) 93-103.

[21] A. Guerrero-Ruiz, P. Badenes, I. Rodŕiguez-Ramos, Appl. Catal. A, 173 (1998) 313-321.

[22] M.C. Roman-Martinez, D. Cazorla-Amoros, A. Linares-Solano, C.S.-M. De Lecea, H. Yamashita, M. Anpo, Carbon, 33 (1995) 3-13.

[23] G.C. Torres, E.L. Jablonski, G.T. Baronetti, A.A. Castro, S.R. de Miguel, O.A. Scelza, M.D. Blanco, M.A. Pen˜a Jiménez, J.L.G. Fierro, Appl. Catal. A, 161 (1997) 213-226.

[24] L.J. Hillenbrand, J.W. Lacksonen, J. Electrochem. Soc., 112 (1965) 249-252.

[25] J. Escard, C. Leclère, J.P. Contour, J. Catal., 29 (1973) 31-39.

[26] A.K. Shukla, A. Hamnett, A. Roy, S.R. Barman, D.D. Sarma, V. Alderucci, L. Pino, N. Giordano, J. Electroanal. Chem., 352 (1993) 337-343.

[27] A.K. Shukla, M.K. Ravikumar, A. Roy, S.R. Barman, D.D. Sarma, A.S. Arico, V. Antonucci, L. Pino, N. Giordano, J. Electrochem. Soc., 141 (1994) 1517-1522.

[28] V. Alderucci, L. Pino, P.L. Antonucci, W. Roh, J. Cho, H. Kim, D.L. Cocke, V. Antonucci, Mater. Chem. Phys., 41 (1995) 9-14.

[29] F. Coloma, A. Sepulveda-Escribano, J.L.G. Fierro, F. Rodriguez-Reinoso, Appl. Catal. A, 148 (1996) 63-80.

[30] R.V. Hull, L. Li, Y.C. Xing, C.C. Chusuei, Chem. Mater., 18 (2006) 1780-1788.

[31] J. Petroski, M.A. El-Sayed, J. Phys. Chem. A, 107 (2003) 8371-8375.

[32] F. Coloma, A. Sepulveda-Escribano, F. Rodriguez-Reinoso, J. Catal., 154 (1995) 299-305.

[33] W.M. Chen, B.D. Qu, Int. J. Hydrogen Energy, 35 (2010) 10102-10108.

[34] K. Kinoshita, J.A.S. Bett, Carbon, 12 (1974) 525-533.

[35] F. Maillard, A. Bonnefont, F. Micoud, Electrochem. Com., 13 (2011) 1109-1111.

[36] C.C. Hung, P.Y. Lim, J.R. Chen, H.C. Shih, J. Power Sources, 196 (2011) 140-146.

[37] N. Giordano, P.L. Antonucci, E. Passalacqua, L. Pino, A.S. Arico, K. Kinoshita, Electrochim. Acta, 36 (1991) 1931-1935.

[38] J. Willsau, J. Heitbaum, J. Electroanal. Chem., 161 (1984) 93-101.

[39] K.H. Kangasniemi, D.A. Condit, T.D. Jarvi, J. Electrochem. Soc., 151 (2004) E125-E132.

[40] K. Kinoshita, J. Bett, Carbon, 11 (1973) 237-247.

[41] F. Maillard, S. Schreier, M. Hanzlik, E.R. Savinova, S. Weinkauf, U. Stimming, Phys. Chem. Chem. Phys., 7 (2005) 385-393.

[42] F. Maillard, E.R. Savinova, U. Stimming, J. Electroanal. Chem., 599 (2007) 221-232.

[43] O.V. Cherstiouk, A.N. Gavrilov, L.M. Plyasova, I.Y. Molina, G.A. Tsirlina, E.R. Savinova, J. Solid State Electrochem., 12 (2008) 497-509.

[44] E.G. Ciapina, S.F. Santos, E.R. Gonzalez, J. Electroanal. Chem., 644 (2010) 132-143.

[45] A. Lopez-Cudero, J. Solla-Gullon, E. Herrero, A. Aldaz, J.M. Feliu, J. Electroanal. Chem., 644 (2010) 117-126.

[46] F. Maillard, M. Eikerling, O.V. Cherstiouk, S. Schreier, E. Savinova, U. Stimming, Faraday Discuss., 125 (2004) 357-377.

[47] O.V. Cherstiouk, P.A. Simonov, E.R. Savinova, Electrochim. Acta, 48 (2003) 3851-3860.

[48] K.J.J. Mayrhofer, J.C. Meier, S.J. Ashton, G.K.H. Wiberg, F. Kraus, M. Hanzlik, M. Arenz, Electrochem. Com., 10 (2008) 1144-1147.

[49] K.J.J. Mayrhofer, S.J. Ashton, J.C. Meier, G.K.H. Wiberg, M. Hanzlik, M. Arenz, J. Power Sources, 185 (2008) 734-739.

[50] Z.Y. Liu, J.L. Zhang, P.T. Yu, J.X. Zhang, R. Makharia, K.L. More, E.A. Stach, J. Electrochem. Soc., 157 (2010) B906-B913.

[51] F.J. Perez-Alonso, C.F. Elkjaer, S.S. Shim, B.L. Abrams, I.E.L. Stephens, I. Chorkendorff, J. Power Sources, 196 (2011) 6085-6091.

[52] J.C. Meier, I. Katsounaros, C. Galeano, H.J. Bongard, A.A. Topalov, A. Kostka, A. Karschin, F. Schuth, K.J.J. Mayrhofer, Energy & Environmental Science, (2012).

[53] L. Dubau, L. Castanheira, Z. Zhao, F. Maillard, Electrochim. Acta, (2013) in preparation for the special Issue of Electrochimica Acta dedicated to the 63rd meeting of the ISE.

[54] O. Antoine, R. Durand, J. Appl. Electrochem., 30 (2000) 839-844.

[55] O. Legrini, E. Oliveros, A.M. Braun, Chem. Rev., 93 (1993) 671-698.

[56] L. Castanheira, in, Université de Grenoble, Grenoble, 2014.

[57] P.A. Simonov, V.A. Likholobov, Physicochemical Aspects of Preparation of Carbon-Supported Noble Metal Catalysts, in: A. Wieckowski, E.R. Savinova, C.G. Vayenas (Eds.) Catalysis & Electrocatalysis at Nanoparticle Surfaces, Marcel Dekker, New York, 2003, pp. 409.

[58] W.T. Lee, L. Ford, P. Blowers, H.L. Nigg, R.I. Masel, Surf. Sci., 416 (1998) 141-151.

[59] B.A. Sexton, Surf. Sci., 102 (1981) 271-281.

[60] K. Christmann, G. Ertl, T. Pignet, Surf. Sci., 54 (1976) 365-392.

[61] R.W. McCabe, L.D. Schmidt, Surf. Sci., 65 (1977) 189-209.

[62] M. Cabie, S. Giorgio, C.R. Henry, M.R. Axet, K. Philippot, B. Chaudret, J. Phys. Chem. C, 114 (2010) 2160-2163.

[63] C. Henry, Adsorption and reaction at supported model catalysts, in: A. Wieckowski, E.R. Savinova, C.G. Vayenas (Eds.) Catalysis and Electrocatalysis at Nanoparticle Surfaces, Eds. Marcel Dekker, New York, 2003, pp. 239-280.

[64] S. Mukerjee, J. McBreen, J. Electroanal. Chem., 448 (1998) 163-171.

[65] H. Kikuchi, W. Ouchida, M. Nakamura, C. Goto, M. Yamada, N. Hoshi, Electrochem. Com., 12 (2010) 544-547.

[66] CRC Handbook of Chemistry and Physics, Internet Version 2005, CRC Press, 2005.

[67] M.C. Román-Martínez, D. Cazorla-Amorós, A. Linares-Solano, C.S.-M. de Lecea, Carbon, 31 (1993) 895-902.

[68] R. Sellin, C. Grolleau, S. Arrii-Clacens, S. Pronier, J.M. Clacens, C. Coutanceau, J.M. Léger, J. Phys. Chem. C, 113 (2009) 21735-21744.

## Chapter IV

[1] W. Vielstich, A. Lamm, H.A. Gasteiger, in, John Wiley & Sons, Chichester, 2003.

[2] E. Guilminot, A. Corcella, F. Charlot, F. Maillard, M. Chatenet, J. Electrochem. Soc., 154 (2007) B96-B105.

[3] Z. Zhao, L. Dubau, F. Maillard, J. Power Sources, 217 (2012) 449-458.

[4] K.J.J. Mayrhofer, J.C. Meier, S.J. Ashton, G.K.H. Wiberg, F. Kraus, M. Hanzlik, M. Arenz, Electrochem. Com., 10 (2008) 1144-1147.

[5] J.C. Meier, C. Galeano, I. Katsounaros, A.A. Topalov, A. Kostka, F. Schüth, K.J.J. Mayrhofer, ACS Catalysis, 2 (2012) 832-843.

[6] T. Yoda, H. Uchida, M. Watanabe, Electrochim. Acta, 52 (2007) 5997-6005.

[7] S. Maass, F. Finsterwalder, G. Frank, R. Hartmann, C. Merten, J. Power Sources, 176 (2008) 444-451.

[8] Z.Y. Liu, J.L. Zhang, P.T. Yu, J.X. Zhang, R. Makharia, K.L. More, E.A. Stach, J. Electrochem. Soc., 157 (2010) B906-B913.

[9] F. Maillard, A. Bonnefont, F. Micoud, Electrochem. Com., 13 (2011) 1109-1111.

[10] N. Linse, L. Gubler, G.G. Scherer, A. Wokaun, Electrochim. Acta, 56 (2011) 7541-7549.

[11] E. Guilminot, A. Corcella, C. Iojoiu, G. Berthomé, F. Maillard, M. Chatenet, J.-Y. Sanchez, J. Electrochem. Soc., 154 (2007) B1106-B1114.

[12] R. Borup, J. Meyers, B. Pivovar, Y.S. Kim, R. Mukundan, N. Garland, D. Myers, M. Wilson, F. Garzon, D. Wood, P. Zelenay, K. More, K. Stroh, T. Zawodzinski, J. Boncella, J.E. McGrath, M. Inaba, K. Miyatake, M. Hori, K. Ota, Z. Ogumi, S. Miyata, A. Nishikata, Z. Siroma, Y. Uchimoto, K. Yasuda, K.I. Kimijima, N. Iwashita, Chem. Rev., 107 (2007) 3904-3951.

[13] Y. Shao-Horn, W. Sheng, S. Chen, P. Ferreira, E. Holby, D. Morgan, Topics Catal., 46 (2007) 285-305.

[14] L. Dubau, L. Castanheira, Z. Zhao, F. Maillard, Electrochim. Acta, (2013) in preparation for the special Issue of Electrochimica Acta dedicated to the 63rd meeting of the ISE.

[15] L.M. Roen, C.H. Paik, T.D. Jarvi, Electrochem. Solid-State Lett., 7 (2004) A19-A22.

[16] K.H. Kangasniemi, D.A. Condit, T.D. Jarvi, J. Electrochem. Soc., 151 (2004) E125-E132.

[17] S. Zhang, X.-Z. Yuan, R. Hiesgen, K.A. Friedrich, H. Wang, M. Schulze, A. Haug, H. Li, J. Power Sources, 205 (2012) 290-300.

[18] C.A. Reiser, L. Bregoli, T.W. Patterson, J.S. Yi, J.D.L. Yang, M.L. Perry, T.D. Jarvi, Electrochem. Solid-State Lett., 8 (2005) A273-A276.

[19] J. Willsau, J. Heitbaum, J. Electroanal. Chem., 161 (1984) 93-101.

[20] M.F. Mathias, R. Makharia, H. Gasteiger, J.J. Conley, T.J. Fuller, G.J. Gittleman, S.S. Kocha, D.P. Miller, C.K. Mittelsteadt, T. Xie, S.G. Yan, P.T. Yu, Interface, 14 (2005) 24-35.

[21] F. Micoud, F. Maillard, A. Bonnefont, N. Job, M. Chatenet, Phys. Chem. Chem. Phys., 12 (2010) 1182-1193.

[22] F. Maillard, S. Pronkin, E.R. Savinova, Influence of size on the electrocatalytic activities of supported metal nanoparticles in fuel cells related reactions, in: W. Vielstich, H.A. Gasteiger, H. Yokokawa (Eds.) Handbook of fuel cells - Fundamentals, technology and applications, John Wiley & Sons, Inc., New York, 2009, pp. 91-111.

[23] K. Kinoshita, Carbon, electrochemical and physicochemical properties, John Wiley & Sons, New York, 1988.

[24] V. Parry, G. Berthomé, J.C. Joud, O. Lemaire, A.A. Franco, J. Power Sources, 196 (2011) 2530-2538.

[25] P.E. Fanning, M.A. Vannice, Carbon, 31 (1993) 721-730.

[26] R.M. Silverstein, F.X. Webster, D.J. Kiemle, Spectrometric identification of organic compounds 7th ed., John Wiley & Sons, Chichester, 2005.

[27] Y. Hiramitsu, H. Sato, H. Hosomi, Y. Aoki, T. Harada, Y. Sakiyama, Y. Nakagawa, K. Kobayashi, M. Hori, J. Power Sources, 195 (2010) 435-444.

[28] M. Hara, M. Lee, C.-H. Liu, B.-H. Chen, Y. Yamashita, M. Uchida, H. Uchida, M. Watanabe, Electrochim. Acta, 70 (2012) 171-181.

[29] F. Tuinstra, J.L. Koenig, J. Chem. Phys., 53 (1970) 1126-1130.

[30] Y. Wang, D.C. Alsmeyer, R.L. McCreery, Chem. Mater., 2 (1990) 557-563.

[31] A. Sadezky, H. Muckenhuber, H. Grothe, R. Niessner, U. Pöschl, Carbon, 43 (2005) 1731-1742.

[32] M. Marcinek, L.J. Hardwick, G.Z. Żukowska, R. Kostecki, Carbon, 48 (2010) 1552-1557.

[33] O.V. Cherstiouk, A.N. Simonov, N.S. Moseva, S.V. Cherepanova, P.A. Simonov, V.I. Zaikovskii, E.R. Savinova, Electrochim. Acta, 55 (2010) 8453-8460.

[34] F. Maillard, M. Eikerling, O.V. Cherstiouk, S. Schreier, E. Savinova, U. Stimming, Faraday Discuss., 125 (2004) 357-377.

[35] F. Maillard, E. Savinova, P.A. Simonov, V.I. Zaikovskii, U. Stimming, J. Phys. Chem. B, 108 (2004) 17893-17904.

[36] F. Maillard, S. Schreier, M. Hanzlik, E.R. Savinova, S. Weinkauf, U. Stimming, Phys. Chem. Chem. Phys., 7 (2005) 385-393.

[37] F. Maillard, E.R. Savinova, U. Stimming, J. Electroanal. Chem., 599 (2007) 221-232.

[38] O.V. Cherstiouk, A.N. Gavrilov, L.M. Plyasova, I.Y. Molina, G.A. Tsirlina, E.R. Savinova, J. Solid State Electrochem., 12 (2008) 497-509.

[39] E.G. Ciapina, S.F. Santos, E.R. Gonzalez, J. Electroanal. Chem., 644 (2010) 132-143.

[40] A. Lopez-Cudero, J. Solla-Gullon, E. Herrero, A. Aldaz, J.M. Feliu, J. Electroanal. Chem., 644 (2010) 117-126.

[41] P.L. Antonucci, L. Pino, N. Giordano, L. Pinna, Mater. Chem. Phys., 21 (1989) 495-506.

[42] N. Giordano, P.L. Antonucci, E. Passalacqua, L. Pino, A.S. Arico, K. Kinoshita, Electrochim. Acta, 36 (1991) 1931-1935.

[43] H.S. Oh, K. Kim, Y.J. Ko, H. Kim, Int. J. Hydrogen Energy, 35 (2010) 701-708.

## Chapter V

[1] E. Guilminot, A. Corcella, F. Charlot, F. Maillard, M. Chatenet, J. Electrochem. Soc., 154 (2007) B96-B105.

[2] Z. Zhao, L. Dubau, F. Maillard, J. Power Sources, 217 (2012) 449-458.

[3] K.J.J. Mayrhofer, D. Strmcnik, B.B. Blizanac, V. Stamenkovic, M. Arenz, N.M. Markovic, Electrochim. Acta, 53 (2008) 3181-3188.

[4] J.C. Meier, C. Galeano, I. Katsounaros, A.A. Topalov, A. Kostka, F. Schüth, K.J.J. Mayrhofer, ACS Catalysis, 2 (2012) 832-843.

[5] T. Yoda, H. Uchida, M. Watanabe, Electrochim. Acta, 52 (2007) 5997-6005.

[6] S. Maass, F. Finsterwalder, G. Frank, R. Hartmann, C. Merten, J. Power Sources, 176 (2008) 444-451.

[7] Z.Y. Liu, J.L. Zhang, P.T. Yu, J.X. Zhang, R. Makharia, K.L. More, E.A. Stach, J. Electrochem. Soc., 157 (2010) B906-B913.

[8] F. Maillard, A. Bonnefont, F. Micoud, Electrochem. Com., 13 (2011) 1109-1111.

[9] N. Linse, L. Gubler, G.G. Scherer, A. Wokaun, Electrochim. Acta, 56 (2011) 7541-7549.

[10] R. Borup, J. Meyers, B. Pivovar, Y.S. Kim, R. Mukundan, N. Garland, D. Myers, M. Wilson, F. Garzon, D. Wood, P. Zelenay, K. More, K. Stroh, T. Zawodzinski, J. Boncella, J.E. McGrath,

M. Inaba, K. Miyatake, M. Hori, K. Ota, Z. Ogumi, S. Miyata, A. Nishikata, Z. Siroma, Y. Uchimoto, K. Yasuda, K.I. Kimijima, N. Iwashita, Chem. Rev., 107 (2007) 3904-3951.

[11] Y. Shao-Horn, W. Sheng, S. Chen, P. Ferreira, E. Holby, D. Morgan, Topics Catal., 46 (2007) 285-305.

[12] S.L. Chen, A. Kucernak, J. Phys. Chem. B, 108 (2004) 13984-13994.

[13] A. Schneider, L. Colmenares, Y.E. Seidel, Z. Jusys, B. Wickman, B. Kasemo, R.J. Behm, Phys. Chem. Chem. Phys., 10 (2008) 1931-1943.

[14] F. Maillard, S. Pronkin, E.R. Savinova, Influence of size on the electrocatalytic activities of supported metal nanoparticles in fuel cells related reactions, in: Handbook of Fuel Cells, John Wiley & Sons, Ltd, 2010.

[15] P.S. Ruvinskiy, A. Bonnefont, C. Pham-Huu, E.R. Savinova, Langmuir, 27 (2011) 9018-9027.

[16] P.S. Ruvinskiy, A. Bonnefont, E.R. Savinova, Electrocatalysis, 2 (2011) 123-133.

[17] N.M. Marković, P.N. Ross Jr, Surf. Sci. Rep., 45 (2002) 117-229.

[18] V.S. Bagotskii, M.R. Tarasevich, V.Y. Filinovskii, Elektrokhimiya, 5 (1969) 1218.

[19] H.S. Wroblowa, Y.C. Pan, G. Razumney, J. Electroanal. Chem., 69 (1976) 195-201.

[20] O. Antoine, R. Durand, J. Appl. Electrochem., 30 (2000) 839-844.

[21] M. Watanabe, H. Sei, P. Stonehart, Journal of Electroanalytical Chemistry and Interfacial Electrochemistry, 261 (1989) 375-387.

[22] F. Maillard, S. Pronkin, E.R. Savinova, Size effects in electrocatalysis of fuel cells reactions on supported metal nanoparticles, in: M.T.M. Koper (Ed.) Fuel Cell Catalysis: a Surface Science Approach, John Wiley & Sons, Inc., New York, 2010.

[23] B. Andreaus, F. Maillard, J. Kocylo, E.R. Savinova, M. Eikerling, J. Phys. Chem. B, 110 (2006) 21028-21040.

[24] M. Inaba, H. Yamada, J. Tokunaga, A. Tasaka, Electrochem. Solid-State Lett., 7 (2004) A474-A476.

[25] P.S. Ruvinskiy, A. Bonnefont, M. Houlle, C. Pham-Huu, E.R. Savinova, Electrochim. Acta, 55 (2010) 3245-3256.

[26] Q. Dong, S. Santhanagopalan, R.E. White, J. Electrochem. Soc., 154 (2007) A888-A899.

[27] J.-B. Donnet, A. Voet, Carbon black: physics, chemistry and elastomer reinforcement, Marcel Dekker, New York, 1976.

[28] F. Maillard, M. Eikerling, O.V. Cherstiouk, S. Schreier, E. Savinova, U. Stimming, Faraday Discuss., 125 (2004) 357-377.

[29] F. Maillard, S. Schreier, M. Hanzlik, E.R. Savinova, S. Weinkauf, U. Stimming, Phys. Chem. Chem. Phys., 7 (2005) 385-393.

[30] F. Maillard, E.R. Savinova, U. Stimming, J. Electroanal. Chem., 599 (2007) 221-232.

## Chapter VI

[1] R. Borup, J. Meyers, B. Pivovar, Y.S. Kim, R. Mukundan, N. Garland, D. Myers, M. Wilson, F. Garzon, D. Wood, P. Zelenay, K. More, K. Stroh, T. Zawodzinski, J. Boncella, J.E. McGrath, M. Inaba, K. Miyatake, M. Hori, K. Ota, Z. Ogumi, S. Miyata, A. Nishikata, Z. Siroma, Y. Uchimoto, K. Yasuda, K.I. Kimijima, N. Iwashita, Chem. Rev., 107 (2007) 3904-3951.

[2] M.K. Debe, A.K. Schmoeckel, G.D. Vernstrom, R. Atanasoski, J. Power Sources, 161 (2006) 1002-1011.

[3] M. Inaba, H. Yamada, J. Tokunaga, A. Tasaka, Electrochem. Solid-State Lett., 7 (2004) A474-A476.

[4] T. Yoda, H. Uchida, M. Watanabe, Electrochim. Acta, 52 (2007) 5997-6005.

[5] P.J. Ferreira, G.J. la O, Y. Shao-Horn, D. Morgan, R. Makharia, S. Kocha, H.A. Gasteiger, J. Electrochem. Soc., 152 (2005) A2256-A2271.

[6] E. Guilminot, A. Corcella, M. Chatenet, F. Maillard, F. Charlot, G. Berthome, C. Iojoiu, J.Y. Sanchez, E. Rossinot, E. Claude, J. Electrochem. Soc., 154 (2007) B1106-B1114.

[7] T. Kinumoto, K. Takai, Y. Iriyama, T. Abe, M. Inaba, Z. Ogumi, J. Electrochem. Soc., 153 (2006) A58-A63.

[8] E. Guilminot, A. Corcella, F. Charlot, F. Maillard, M. Chatenet, J. Electrochem. Soc., 154 (2007) B96-B105.

[9] J. Xie, D.L. Wood, D.M. Wayne, T.A. Zawodzinski, P. Atanassov, R.L. Borup, J. Electrochem. Soc., 152 (2005) A104-A113.

[10] J. Xie, D.L. Wood, K.L. More, P. Atanassov, R.L. Borup, J. Electrochem. Soc., 152 (2005) A1011-A1020.

[11] G.X. Wang, L. Yang, J.Z. Wang, H.K. Liu, S.X. Dou, J. Nanosci. Nanotech., 5 (2005) 1135-1140.

[12] Y. Shao-Horn, W. Sheng, S. Chen, P. Ferreira, E. Holby, D. Morgan, Topics Catal., 46 (2007) 285-305.

[13] X. Yu, S. Ye, J. Power Sources, 172 (2007) 145-154.

[14] Y. Shao, G. Yin, Y. Gao, J. Power Sources, 171 (2007) 558-566.

[15] X.P. Wang, R. Kumar, D.J. Myers, Electrochem. Solid-State Lett., 9 (2006) A225-A227.

[16] Z. Nagy, H. You, Electrochim. Acta, 47 (2002) 3037-3055.

[17] S. Mitsushima, S. Kawahara, K.I. Ota, N. Kamiya, J. Electrochem. Soc., 154 (2007) B153-B158.

[18] R.L. Borup, J.R. Davey, F.H. Garzon, D.L. Wood, M.A. Inbody, J. Power Sources, 163 (2006) 76-81.

[19] M. Cai, M.S. Ruthkosky, B. Merzougui, S. Swathirajan, M.P. Balogh, S.H. Oh, J. Power Sources, 160 (2006) 977-986.

[20] M. Weissmann, S. Baranton, J.M. Clacens, C. Coutanceau, Carbon, 48 (2010) 2755-2764.

[21] M. Weissmann, S. Baranton, C. Coutanceau, Langmuir, 26 (2010) 15002-15009.

[22] M.K. Debe, in: W. Vielstich, A. Lamm, H. Gasteiger (Eds.) Handbook of fuel cells: fundamentals, technology, and applications, John Wiley & Sons, 2003, pp. 576-589.

[23] M.K. Debe, A.K. Schmoeckel, G.D. Vernstrorn, R. Atanasoski, J. Power Sources, 161 (2006) 1002-1011.

[24] L. Gancs, T. Kobayashi, M.K. Debe, R. Atanasoski, A. Wieckowski, Chem. Mater., 20 (2008) 2444-2454.

[25] D. van der Vliet, C. Wang, M. Debe, R. Atanasoski, N.M. Markovic, V.R. Stamenkovic, Electrochim. Acta, 56 (2011) 8695-8699.

[26] H. Zhou, W.-p. Zhou, R.R. Adzic, S.S. Wong, J. Phys. Chem. C, 113 (2009) 5460-5466.

[27] C. Koenigsmann, W.P. Zhou, R.R. Adzic, E. Sutter, S.S. Wong, Nano Lett., 10 (2010) 2806-2811.

[28] W.-P. Zhou, M. Li, C. Koenigsmann, C. Ma, S.S. Wong, R.R. Adzic, Electrochim. Acta, 56 (2011) 9824-9830.

[29] C. Koenigsmann, E. Sutter, T.A. Chiesa, R.R. Adzic, S.S. Wong, Nano Lett., 12 (2012) 2013-2020.

[30] C.-C. Chien, K.-T. Jeng, Mater. Chem. Phys., 103 (2007) 400-406.

[31] S.M. Choi, J.H. Kim, J.Y. Jung, E.Y. Yoon, W.B. Kim, Electrochim. Acta, 53 (2008) 5804-5811.

[32] S. Mahima, R. Kannan, I. Komath, M. Aslam, V.K. Pillai, Chem. Mater., 20 (2007) 601-603.

[33] Y. Song, R.M. Garcia, R.M. Dorin, H. Wang, Y. Qiu, E.N. Coker, W.A. Steen, J.E. Miller, J.A. Shelnutt, Nano Lett., 7 (2007) 3650-3655.

[34] I.-S. Park, J.-H. Choi, Y.-E. Sung, Electrochem. Solid-State Lett., 11 (2008) B71-B75.

[35] L. Xiao, L. Zhuang, Y. Liu, J. Lu, H.c.D. AbrunÌƒa, J. Am. Chem. Soc., 131 (2008) 602-608.

[36] S. Wang, S.P. Jiang, X. Wang, J. Guo, Electrochim. Acta, 56 (2011) 1563-1569.

[37] S.F. Wang, Journal of Physics a-Mathematical and Theoretical, 41 (2008) 15.

[38] D.F. Evans, D.J. Mitchell, B.W. Ninham, J. Phys. Chem., 90 (1986) 2817-2825.

[39] J.M. Tingey, J.L. Fulton, D.W. Matson, R.D. Smith, J. Phys. Chem., 95 (1991) 1445-1448.

[40] K. Mukherjee, D.C. Mukherjee, S.P. Moulik, J. Colloid Interface Sci., 187 (1997) 327-333.

[41] H.P. Klug, L.E. Alexander, in, Wiley New York, 1974, pp. 175.

[42] E.G. Ciapina, S.F. Santos, E.R. Gonzalez, J. Electroanal. Chem., 644 (2010) 132-143.

[43] F. Maillard, S. Schreier, M. Hanzlik, E.R. Savinova, S. Weinkauf, U. Stimming, Phys. Chem. Chem. Phys., 7 (2005) 385-393.

[44] F. Maillard, E.R. Savinova, U. Stimming, J. Electroanal. Chem., 599 (2007) 221-232.

[45] B. Beden, C. Lamy, A. Bewick, K. Kunimatsu, J. Electroanal. Chem., 121 (1981) 343-347.

[46] B. Beden, F. Hahn, S. Juanto, C. Lamy, J.M. Léger, J. Electroanal. Chem., 225 (1987) 215-225.

[47] P. Waszczuk, A. Wieckowski, P. Zelenay, S. Gottesfeld, C. Coutanceau, J.M. Léger, C. Lamy, J. Electroanal. Chem., 511 (2001) 55-64.

[48] F. Vigier, S. Rousseau, C. Coutanceau, J.M. Léger, C. Lamy, Topics Catal., 40 (2006) 111-121.

[49] C. Lamy, A. Lima, V. LeRhun, F. Delime, C. Coutanceau, J.M. Léger, J. Power Sources, 105 (2002) 283-296.

[50] J.M. Léger, S. Rousseau, C. Coutanceau, F. Hahn, C. Lamy, Electrochim. Acta, 50 (2005) 5118-5125.

UNIVERSITÉ DE GRENOBLE

## Résumé

Ce travail de thèse s'est intéressé aux mécanismes de dégradation de nanoparticules de Pt supportées sur carbone utilisées pour catayser les réactions électrochimiques dans une pile à combustible à membrane échangeuse de protons (PEMFC). Une attention particulière a été portée au mécanisme de l'oxydation électrochimique du Vulcan XC72, un noir de carbone couramment utilisé dans les couches catalytiques de PEMFC. Des mesures par spectroscopie Raman ont montré que les domaines désordonnés du Vulcan XC72 (non-graphitiques, hybridisation $sp^3$) sont corrodés de façon préférentielle dans des conditions expérimentales proches de celles d'une cathode de PEMFC. En conséquences, les nanoparticules de Pt se détachent ou agglomèrent comme le révèlent des expériences par microscopie électronique en transmission. Les distances entre nanoparticules de Pt influencent les cinétiques de la réaction cathodique par des effets liés au transport et à la ré-adsorption des intermédiaires réactionnels. Nous montrons également que les nanocristallites de Pt ne sont pas immobiles mais qu'elles agglomèrent en présence de molécules réductrices. La vitesse de migration augmente dans l'ordre : CO > $CH_3OH$ > $H_2$. Finalement, les nano-fils de Pt révèlent un potentiel intéressant pour surmonter les problèmes de durabilité des matériaux conventionnels évoqués dans cette thèse.

Mots clés : pile à combustible à membrane échangeuse de protons, durabilité des matériaux de PEMFC, oxydation électrochimique du carbone, migration des cristallites, nano-fils de Pt.

## Abstract

This Ph.D. focused on the degradation mechanisms of carbon-supported Pt nanoparticles used to catalyse the hydrogen oxidation reaction, and the oxygen reduction reaction (ORR) in proton-exchange membrane fuel cells (PEMFC). We paid special attention to the mechanism of the electrochemical oxidation of Vulcan XC72, a conventional carbon black support classically used in PEMFC catalytic layers. Raman spectroscopy measurements evidence that the disordered domains of the Vulcan XC72 support (non-graphitic, $sp^3$-hybridized) are preferentially oxidized in experimental conditions mimicking the operation of a PEMFC cathode. A major consequence of the oxidation of the high surface area carbon support is the aggregation and the detachment of the supported Pt nanoparticles, as revealed by identical location transmission electron microscopy experiments. The increasing distances between the Pt nanoparticles impacts the ORR kinetics through transport-readsorption effects. Evidences were also provided that the carbon-supported Pt nanoparticles are not immobile but prone to agglomerate in the presence of reducing molecules, and that the migration rate increases in the order CO > $CH_3OH$ > $H_2$. Finally, Pt nanowires have been synthesized to overcome the durability issues faced with the conventional materials used in a PEMFC.

Keywords: proton exchange membrane fuel cell, durability of PEMFC materials, electrochemical carbon oxidation, crystallite migration, Pt nanowires.